



Norwegian University of  
Science and Technology

# Aerodynamic Stability of Long-span Suspension Bridges

**Magnus Aa Dalen**

Civil and Environmental Engineering

Submission date: June 2016

Supervisor: Ole Andre Øiseth, KT

Norwegian University of Science and Technology  
Department of Structural Engineering



## **MASTEROPPGAVE 2016**

for

*Magnus Aa Dalen*

### **Aerodynamisk stabilitet av hengebruere**

#### *Aerodynamic stability of suspension bridges*

I forbindelse med prosjektet ferjefri E39 planlegges det en rekke grensesprengende brokonstruksjoner. En av de viktigste kriteriene for et vellykket design er å unngå uønskede vibrasjoner på grunn av vind. Aerodynamisk stabilitet gis ofte spesiell oppmerksomhet siden dette kan føre til at konstruksjonen kollapse. Den aerodynamiske utformingen av brotversnittet har en nøkkelrolle for å oppnå en høy stabilitetsgrense, men konstruksjonens egenskaper er også viktige. Konstruksjonens egenfrekvenser og frekvensforhold, svingeformenes formlighet og modale masser er eksempler på parametere som vil ha en stor innflytelse på stabilitetsgrensen. Denne oppgaven dreier seg om å finne en konstruktiv utforming som gir så høy stabilitetsgrense som mulig.

Oppgaven bør inneholde følgende temaer.

- En grundig gjennomgang av de ulike typene instabilitetsfenomenene
- Beskrivelse av flutter likningene
- Beskrivelse av instabilitetsfenomener der flere «stille luft» moder inngår
- Optimalisering av en bro med hovedspenn på 2000m

Studentene velger selv hva de ønsker å legge vekt på

Besvarelsen organiseres i henhold til gjeldende retningslinjer.

*Veileder(e)*: Ole Andre Øiseth, Michael Styrk Andersen.

NTNU, 25.01.2015

Ole Andre Øiseth  
faglærer





# Abstract

A MATLAB script for making customized finite element models of suspension bridges is created. The main purpose of the script is to perform eigenvalue analysis of different bridge setups to investigate the controlling parameters for the torsional-to-vertical frequency ratios. The modal output from the model is used to perform aerodynamic stability analysis. The in-wind complex eigenvalue problem (CEV) is solved in an iterative procedure in order to locate the stability limits of the various bridge setups. The bridge geometries investigated originates from a conceptual study on triple-girder flutter-free bridges conducted by Michael Styrk Andersen at The University of Southern Denmark.

The FE-model is verified by analysing the Hardanger Bridge. Both the model output and the instability limit, found as 77.5 m/s, is in good agreement with previous research. The results for other setups gave reasonable natural frequencies and mode shapes, and are verified by simplified calculations made by Michael Styrk Andersen. The widest triple-girder configuration, Setup 3, shows below unity frequency ratios, as expected. The importance of pylon stiffness is investigated, and it is concluded that the natural frequencies are not very sensitive to changes in pylon stiffness. An analysis is made to determine what effect the crossbeam stiffness has on the natural frequencies. For very stiff crossbeams the frequency ratio of Setup 3 was inverted. This allows classical flutter, reducing the stability limit considerably.

The available literature has been searched for applicable aerodynamic derivatives for the configurations that are studied. The Messina ADs are implemented for the triple-girder setups. The results are not satisfactory as they are highly unstable regarding the choice of curve fitting. Therefore all setups are analysed using Hardanger and Theodorsen ADs. Michael has planned and performed wind tunnel tests on Setup 1-3 parallel with the work on this project. The data is not yet processed as this report is in its finishing stages. It is therefore left for further work to analyse the stability of these setups with the correct ADs.

Besides the verification by Hardanger Bridge, there are mainly three different bridge setups analysed. They are all fictitious designs of a suspension bridge crossing Halsafjorden on the Norwegian coastal highway E39. The bridges has main spans of 2050 meters. Setup 1 is a single hollow-box girder similar to the Hardanger bridge girder. The stability limit is 26.5 m/s, and denotes the wind velocity at which the bridge deck enters coupled flutter in the first pair of symmetric modes. Setup 2 has a medium wide triple-girder bridge deck. With Hardanger ADs it undergoes classical flutter at 28.2 m/s, in good correspondence with observed behaviour in wind tunnel testing. The stability limit of Setup 3 is not identified by the complex eigenvalue procedure applied because of the low frequency ratios. The results indicate a critical wind speed of circa 71 m/s for torsional divergence. Unlike the Hardanger analysis, all setups with span-length 2050 meters has considerable lateral deflections in the anti-symmetric torsional modes. This increases the effect of the lateral ADs on the critical wind speed and frequencies. It is however observed that neglecting these ADs is conservative for all analyses in this report.

The in-wind characteristics of suspension bridges with low torsional-to-vertical frequency

ratios are investigated. The present results indicates that such bridges has good aerodynamic performance and that flutter instability is avoided. Achieving such low frequency ratios is though compromising for the torsional stiffness of the bridge deck girder, causing fairly low stability limits for static divergence. A CEV analysis of Setup 3 with improved torsional stiffness is conducted, indicating an improvement of the wind velocity at which static divergence occurs. The results indicate a critical wind velocity for static divergence of 91 m/s when increasing the cable distance from 30 to 40 meters. This result verifies indications made in existing research on similar bridges.

# Sammendrag

I denne oppgaven er det laget et MATLAB skript som genererer tilpassede elementmetode-modeller (FE-modeller) av hengebruer. Skriptets formål er å utføre modalanalyse av ulike konfigurasjoner for hengebruer, for å undersøke hvilke parametere som påvirker frekvensforholdene mellom torsjons- og vertikalmøder. Resultatene fra modalanalysen brukes så til å utføre beregninger på aerodynamisk stabilitet ved å vurdere det dempede, komplekse egenverdiproblemet (CEV). Løsningen av det dempede egenverdiproblemet blir regnet ut som en del av en iterativ prosess som skal identifisere stabilitetsgrensene for de ulike konfigurasjonene. Geometrien til konfigurasjonene som er brukt kommer fra et konseptstudie på trippelbjelke-hengebruer med lave frekvensforhold, som utføres av PhD kandidat Michael Styrk Andersen ved Syddask Universitet.

FE-modellen er verifisert ved å vurdere Hardangerbrua. Både de modale resultatene, og den beregnede stabilitetsgrensen på 77.5 m/s er i god overenstemmelse med tidligere forskning. De andre konfigurasjonene ga rimelige egenfrekvenser og egenmoder, og er verifisert ved forenklete beregninger utført av Michael Styrk Andersen. Den bredeste av trippelbjelke-konfigurasjonene, Setup 3, har som forventet frekvensforhold under 1. Det er undersøkt hvor mye stivheten av tårnene påvirker egenfrekvenser og egenmoder, og det er konkludert med at disse parameterne er lite sensitive ovenfor endringer i tårnstivhet. Det er også vurdert hvordan stivheten av kryssbjelkene påvirker egenfrekvensene. Med svært stive kryssbjelker fikk Setup 3 frekvensforhold over 1. Dette gjør at flutter kan oppstå, og reduserer stabilitetsgrensen betraktelig.

Det er gjort et søk i litteraturen etter tilgjengelige aerodynamisk deriverte (ADer) for hengebruer med tre brubjelker. De deriverte for brua som ble planlagt over Messinastredet er implementert for trippelbjelke-konfigurasjonene. Resultatene er dog ikke tilfredsstillende da de viser seg å være svært sensitive i forhold til linjetilpasning av måledata. Derfor er alle konfigurasjoner analysert med aerodynamisk deriverte fra Hardangerbrua, samt Theodorsens teoretiske ADer. Parallelt med arbeidet med denne oppgaven har Michael planlagt og utført vindtunneltesting av Setup 1-3. Måledataene var ikke ferdig bearbeidet da denne oppgaven var i avsluttende fase. Det er derfor etterlatt til videre arbeid å undersøke stabiliteten av disse konfigurasjonene med de korrekte aerodynamisk deriverte.

Foruten beregningsmodellen av Hardangerbrua er det hovedsakelig tre ulike konfigurasjoner som er analysert, Setup 1-3. De er alle fiktive design av en hengebru som krysser Halsafjorden på E39. Bruene har et hovedspenn på 2050 meter. Setup 1 har én brubjelke med et lukket kassetverrsnitt, svært likt som for Hardangerbrua. Stabilitetsgrensen er beregnet til å være 26.5 m/s, og er den vindhastigheten der brudekket opplever koblet flutter. Setup 2 har en middels bred trippelbjelke. Med Hardanger deriverte er stabilitetsgrensen 28.2 m/s, i god overensstemmelse med observasjoner gjort under vindtunneltestingen. Stabilitetsgrensen til Setup 3 er ikke identifisert ved beregningsprosedyren som er brukt, på grunn av de lave frekvensforholdene. Resultatene indikerer en kritisk vindhastighet for statisk divergens på ca. 71 m/s.

I motsetning til Hardangerbrua får alle konfigurasjonene med hovedspenn på 2050 meter vesentlige horisontale forskyvninger i de antisymmetriske torsjonsmodene. Dette øker

innflytelsen til de horisontale aerodynamiske deriverte i stabilitetsberegningene. Det er observert at det er konservativt å neglisjere de horisontale deriverte for alle konfigurasjonene som er analysert i denne oppgaven.

Egenskapene til vindutsatte hengebruer med lave torsjon-til-vertikal frekvensforhold er undersøkt. Resultatene som er lagt frem indikerer at slike bruer har gode aerodynamiske egenskaper, og at flutter ikke vil oppstå. Å oppnå lave frekvensforhold kan dog gå på bekostning av torsjonsstivheten til brua. Dette kan medføre lav kritisk vindhastighet for statisk divergens. Denne effekten er vist ved en stabilitetsberegning av Setup 3 med økt torsjonsstivhet og rotasjonstregghet, men med frekvensforhold fremdeles under 1. Resultatene indikerer en økt stabilitetsgrense på ca. 91 m/s for statisk divergens når kabelavstanden blir økt fra 30 til 40 meter. Dette er som forventet, og det bekrefter indikasjoner gjort i tidligere forskning.

## Preface

This report is the result of 20 weeks work during the spring of 2016. The report constitutes my master thesis at the Department of Structural Engineering at the Norwegian University of Science and Technology (NTNU). Doing this masters project has been an educational journey, and it would not have been possible without the help and the resources from the Department.

I would like to thank my supervisor Associate Professor Ole Øiseth for the follow-up and his sharing of experiences and opinions. This project would not have been possible without his guidance and knowledge.

Special thanks also goes to supervisor PhD Candidate Michael Styrk Andersen at the University of Southern Denmark. The educational conversations and feedback you have provided has improved my work considerably throughout these 20 weeks. I hope you will find the results useful in your further research.



# Contents

<b>List of Figures</b>	<b>xiii</b>
<b>List of Tables</b>	<b>xv</b>
<b>1 Introduction</b>	<b>1</b>
1.1 Problem description . . . . .	1
1.2 Structure of the report . . . . .	1
<b>2 Basic theory</b>	<b>3</b>
2.1 Structural dynamics and modal analysis . . . . .	3
2.2 Wind and motion induced loads . . . . .	3
2.3 Aerodynamic derivatives . . . . .	5
2.4 Theodorsen’s aerodynamic derivatives . . . . .	7
2.5 Motion induced instabilities . . . . .	8
2.5.1 Static divergence . . . . .	9
2.5.2 Galloping . . . . .	10
2.5.3 Instability in pure torsion . . . . .	11
2.5.4 Bimodal flutter . . . . .	12
2.5.5 Multi-modal flutter . . . . .	14
<b>3 Numerical models</b>	<b>18</b>
3.1 FE-model . . . . .	18
3.2 MATLAB script for flutter analysis . . . . .	23
<b>4 Case study – Aerodynamic stability of a triple- girder suspension bridge</b>	<b>25</b>
4.1 Introduction . . . . .	25
4.2 The triple- girder concept . . . . .	25
4.3 Configurations for this thesis . . . . .	26
<b>5 Modal results</b>	<b>28</b>
5.1 Verification of FE-model: The Hardanger Bridge replica . . . . .	28
5.2 Estimated modal results . . . . .	29
5.3 Vibration modes and natural frequencies for Setup 1-3 . . . . .	31
5.4 Pylon analysis . . . . .	32
5.5 Stiffness of crossbeams . . . . .	33
<b>6 Aerodynamic derivatives</b>	<b>35</b>
6.1 Assumptions . . . . .	35
6.2 The role of each aerodynamic derivative . . . . .	36
6.3 Accuracy of aerodynamic derivatives . . . . .	37
6.4 ADs of the setups in this thesis . . . . .	38
<b>7 The critical wind velocity</b>	<b>42</b>
7.1 Flutter analysis of the Hardanger Bridge replica . . . . .	42
7.2 Setup 1 . . . . .	46
7.3 Adopting the Messina ADs for Setup 2 and 3. . . . .	49
7.4 Setup 2 . . . . .	50
7.5 Setup 3 . . . . .	52

7.6	Setup 2 with Theodorsen and Hardanger ADs . . . . .	54
7.7	Setup 3 with Theodorsen and Hardanger ADs . . . . .	56
7.8	Stability limit for Setup 1-3 with stiff crossbeams . . . . .	57
7.9	Modified Setup 3 with improved torsional stiffness . . . . .	60
<b>8</b>	<b>Final considerations and main research findings</b>	<b>63</b>
8.1	Further work . . . . .	65
	<b>References</b>	<b>66</b>
	<b>Appendices</b>	<b>68</b>
<b>A</b>	<b>Geometric and mechanical properties Setup 1-3</b>	<b>68</b>
<b>B</b>	<b>Geometric and mechanical properties Hardanger Bridge</b>	<b>69</b>
<b>C</b>	<b>Mode shapes for Setup 1-3</b>	<b>70</b>



# Abbreviations

## Acronyms

DOF	Degree of freedom
FE	Finite element
ADs	Aerodynamic derivatives
NPRA	Norwegian Public Roads Administration
CEV	Complex eigenvalue

## Nomenclature

$\hat{\mathbf{E}}$	Impedance matrix
$\mathbf{M}, \mathbf{C}, \mathbf{K}$	Mass, damping, and stiffness matrices
$A_{1-6}^*$	Aerodynamic derivatives in torsion
$P_{1-6}^*$	Aerodynamic derivatives lateral (in-wind) direction
$H_{1-6}^*$	Aerodynamic derivatives for vertical (cross-wind) direction
$C_L$	Force coefficient of bridge deck associated with lift
$C_D$	Force coefficient of bridge deck associated with drag
$C_M$	Force coefficient of bridge deck associated with rotation
$C'_L$	Change of $C_L$ as the rotation increases
$C'_D$	Change of $C_D$ as the rotation increases
$C'_M$	Change of $C_M$ as the rotation increases
$V$	Wind velocity
$V_{red}$	Reduced wind velocity
$B$	Width of bridge deck
$f$	Natural frequency in hertz
$\rho$	Density of air
$\omega$	Natural frequency in radians
$\phi(x)$	Mode shape
$\zeta$	Damping ratio
$\gamma$	Frequency ratio
$\psi$	Shapewise similarity factor
$\eta$	Modal coordinate

## Notations

$z, Z$	Scalar
$\mathbf{Z}$	Matrix
$Z_{ij}$	Element in row $i$ and column $j$ of matrix $\mathbf{Z}$
$\dot{z}$	Time derivative of variable $z$
$\tilde{\mathbf{Z}}$	Matrix in modal frequency domain
$\mathbf{Z}_0$	Zero-wind coefficient matrix of the undamped system
$\mathbf{Z}_{ae}$	In-wind coefficient matrix of the damped system



# List of Figures

1	Visualization of system stability depending on the eigenvalues . . . . .	16
2	Real part of complex eigenvalue solution corresponding to in- wind frequencies. . . . .	17
3	Main parameters of the suspension bridge. Undeformed geometry. . . . .	19
4	Main elements of the triple- girder suspension bridge. . . . .	19
5	Element axis definition in Abaqus. Facsimile from Abaqus Keywords Reference Guide [1]. . . . .	20
6	Bridge cross section for one, two and three girders . . . . .	21
7	Geometry before and after the *STATIC tensioning step. Example setup: Girder height mid span before tensioning = 45m. Girder height after tenioning = 8.5 m. . . . .	22
8	Setup 3 with pylons highlighted . . . . .	23
9	From right: Setup 1, Setup 2 and Setup 3. . . . .	26
10	Positioning of crossbeams and cables . . . . .	26
11	Hardanger configuration of FE-Model . . . . .	28
12	Different curve fittings for $H_4^*$ of the Messina Bridge. . . . .	36
13	3-DOF convention corresponding to the aerodynamic derivatives. $r_D = r_1$ , $r_L = r_2$ , $r_\theta = r_3$ . . . . .	37
14	Geometry of the Hardanger bridge. Geometry taken from [19]. . . . .	38
15	Geometry of Messina tripple- girder. Facsimile from [15]. . . . .	39
16	Geometry of Setup 3. The external girders are very narrow, only 3.5 m wide. . . . .	40
17	ADs corresponding to aerodynamic stiffness. Normalized with frequencies in radians. . . . .	40
18	ADs corresponding to aerodynamic damping. Normalized with frequencies in radians. . . . .	41
19	Shapewise similarity of 1TS and 1TS* in torsion. $\psi_{16,17} = 0.9999$ . . . . .	43
20	Solution of the complex eigenvalue problem for Hardanger replica using Theodorsen ADs. It is clearly seen that 1TS is the mode that drives the system to flutter. . . . .	45
21	Solution of the complex eigenvalue problem for Hardanger replica using Hardanger ADs . . . . .	45
22	Critical mode shapes for the Hardanger Bridge . . . . .	46
23	Similarity of critical modes for Setup 1 . . . . .	47
24	Solution of the complex eigenvalue problem for Setup 1 with Theodorsen ADs. . . . .	48
25	Solution of the complex eigenvalue problem for Setup 1 with Hardanger ADs. . . . .	48
26	Solution of the complex eigenvalue problem for Setup 2 with Messina ADs. . . . .	51
27	Imaginary part of solution for Setup 2, corresponding to frequencies. Messina ADs. Be aware of that each branch changes colour when crossing another branch. The legend refers to the initial colours. . . . .	52
28	Solution of the complex eigenvalue problem for Setup 3 with Messina ADs. . . . .	53
29	Imaginary part of solution for Setup 3, corresponding to frequencies. Be aware of that each branch changes colour when crossing another branch. The legend refers to the initial colours. . . . .	54
30	Frequency development for Setup 2, Theodorsen ADs. 10 first modes. . . . .	55

31	Frequency development for Setup 3, Hardanger ADs. 10 first modes. Be aware that the iterative flutter script sorts the frequencies by magnitude in each iteration. This disturbs the plot function, making each frequency branch to change colour when it crosses another branch. . . . .	56
32	Mode shape of 1TA for regular Setup 2 and Setup 2 with stiff crossbeams.	59
33	Frequency development of modified Setup 3 with Hardanger ADs. . . . .	62
34	The triple-girder system will cause challenges related to detailed design. .	65

# List of Tables

1	Input parameters suspension bridge code . . . . .	18
2	Mechanical properties that must be defined by the analyst for each main structural part of the bridge. See Figure 5 for axis definition. . . . .	19
3	The different setups . . . . .	27
4	Abbreviations that describes the mode shapes . . . . .	28
5	Modal output for the Hardanger Bridge replica compared to NRPA model.	29
6	Eigen-frequencies supplied by advisor Michael Styrk Andersen . . . . .	30
7	Frequency ratio $\gamma_\omega$ for the first pair of symmetric (S) and anti- symmetric (A) vertical and torsional modes, obtained from Table 6 . . . . .	30
8	Natural frequencies of the three setups. Error refers to the supplied results by Michael Styrk Andersen in table 6. The mode shapes are illustrated in appendix C . . . . .	31
9	Frequency ratio $\gamma_\omega$ for the first pair of symmetric (S) and anti- symmetric (A) vertical and torsional modes, obtained from Table 9 . . . . .	31
10	Eigen-frequencies of different tower setups. Error refers to Analysis 1. . . . .	32
11	Eigenfrequencies Setup 1-3 with stiff crossbeams. The error refers to the normal configuration of Setup 1-3, as seen in Table 8 . . . . .	34
12	Critical wind velocity for Hardanger replica. Theodorsen ADs, Hardanger ADs with $P_{1-6}^* = 0$ , $H_{5,6}^* = 0$ , and $A_{5,6}^* = 0$ , and the full set of Hardanger ADs is reported. . . . .	43
13	Results from Øiseth, Rønnquist, and Sigbjørnsson, 2010 [10] . . . . .	44
14	Width and lengths of some well- known bridges. The Table is a modified reproduction from [10] . . . . .	46
15	Critical wind velocity for Setup 1 using different types of ADs . . . . .	47
16	Ratio between total width and total gap-width . . . . .	50
17	Reduced width used in flutter calculations for Setup 2 and 3 . . . . .	50
18	Critical wind velocity for Setup 2 . . . . .	51
19	Critical wind velocity for Setup 3 with different extrapolation polynomials.	53
20	Estimated critical wind velocity for Setup 2 with different types of ADs. B=23m . . . . .	55
21	Estimated critical wind velocity for Setup 3. B=23m. No stability limit found. . . . .	56
22	Frequency ratios with stiff crossbeams . . . . .	57
23	Stability limit and critical frequencies for Setup 1-3 with stiff crossbeams. The difference refers to the original stability limits of Setup 1-3 in Table 15, 20 and 21. . . . .	58
24	Natural frequencies of modified Setup 3. Increased cable distance. Mass is moved from central to external girder. Error refers to the regular Setup 3.	60
25	Frequency ratio for first pair of torsional and veritcal mode pairs . . . . .	60
26	Stability limit and critical frequencies for modified Setup 3. Increased cable distance. Mass is moved from central to external girder . . . . .	61
27	Geometrical- and material- properties for Setup 1-3 . . . . .	68
28	Geometrical- and material- properties og the Hardanger Bridge . . . . .	69
29	Modeshapes for Setup 1-3. Sideview/Topview. . . . .	70



---

# 1 Introduction

As a part of the project on making the Norwegian coastal highway E39 ferry-free, the Norwegian Public Roads Administration (NPRA) facilitates research on possible ways of crossing the wide and deep fjords of the Norwegian west coast. One of the alternatives is to develop technology that allows suspension bridges so span further than ever before. The effects of such slender and flexible structures being subjected to the harsh climate of the Norwegian west coast, is a challenge that the experts within structural engineering and aerodynamics will have to face in the years to come. This thesis investigates the behaviour of long-span suspension bridges both in terms of modal quantities and aerodynamic stability. The aerodynamic design of the bridge deck is of high importance when constructing long-span suspension bridges, but the structural characteristics are also key parameters.

## 1.1 Problem description

The work leading to this report is done in cooperation with Michael Styrk Andersen at the University of Southern Denmark. Michael is doing a study on flutter free bridges. The goal of this thesis is to provide an adaptable FE-code that can be used in the further research, and to investigate the frequency ratios and stability limits of a variety of bridge configurations. Bridges with low frequency ratios is given a special focus since they are expected to avoid classical flutter.

This thesis concerns the development of a FE-code that easily can be adapted to describe a broad variety of suspension bridge setups. The model will be used to determine the modal output of different suspension bridge setups. The main configurations are Setup 1-3, that is provided by Michael. A parameter study on which structural elements that affects the frequency ratios of a suspension bridge is conducted.

The modal output from the various FE-models is used to determine the aerodynamic stability limit of the bridge-sections. The stability is assessed by a complex MATLAB routine provided by supervisor Ole Øiseth. The goal of these stability analyses is to determine which characteristics has the most influence on the flutter instability of cable-supported bridges. The purpose of the results is to expand the understanding of flutter-free bridges, and to create a structural design with high stability limit.

## 1.2 Structure of the report

This paper starts with a presentation of the basic theory of structural dynamics as well as aeroelastic theory related to wind-induced instabilities. This theory is developed in order to provide a mathematical understanding of the flutter instability. Next up, the FE-code is presented. Chapter 3.1 together with Appendix B and C should be sufficient documentation of the MATLAB code for the FE-model, assuming the user has some experience using Abaqus keywords.

The main results are reported in Chapter 5 and 7. First, the results from the modal frequency analysis in Abaqus is reported in Chapter 5. The definitions and assumptions of the aerodynamic derivatives is presented in Chapter 6, before the stability limits and in-wind behaviour of the setups are presented in Chapter 7. The discussion and processing of the results are done in the same chapter as they are presented. The loose strings are gathered in the final considerations in Chapter 8.



---

## 2 Basic theory

### 2.1 Structural dynamics and modal analysis

All dynamic calculations starts with equation of motion

$$\mathbf{M}\ddot{r} + \mathbf{C}\dot{r} + \mathbf{K}r = \mathbf{Q}(t) \quad (1)$$

where  $\mathbf{M}$ ,  $\mathbf{C}$ , og  $\mathbf{K}$  is the system mass-, damping-, and stiffness matrix.  $\mathbf{Q}$  is the vector containing the external loads that acts on the system. By considering the undamped system without external loads, and assuming that the displacement  $r$  can be described by a harmonic oscillating function

$$\mathbf{M}\ddot{r} + \mathbf{K}r = 0 \quad r = a_i e^{i\omega t} \quad (2)$$

we obtain the undamped eigenproblem [18]

$$(\mathbf{K} - \omega_n^2 \mathbf{M})\phi = 0 \quad (3)$$

where  $\omega$  is the eigenvalue and  $\phi$  is the associated eigenvector of the system. In structural dynamics these parameters corresponds to the eigenfrequency and the eigenmode of the system. These undamped quantities will herein be referred to as the still-air quantities.

In the study of structural dynamics it is expedient to apply a modal frequency approach. The structural displacements are represented by generalized degrees of freedom (DOF), as products of space dependant mode shapes  $\phi_n(x)$  and time dependant modal coordinates  $\eta_n(t)$ .

$$r_n = \phi_n(x)\eta_n(t) \quad (4)$$

This approach allows us to describe the response of a structure with high accuracy with only a few modal degrees of freedom.

### 2.2 Wind and motion induced loads

When a wind field meets a fixed obstacle, the velocity pressure from the wind field that acts on the structure is given by Bernoulli's equation.

$$q_U = \frac{1}{2}\rho[U(t)]^2 \quad (5)$$

$\rho$  is the density of air, and  $U(t)$  is the air velocity that can be separated into a mean wind velocity  $\bar{V}$  and a time dependent fluctuating part  $u(t)$ , also known as turbulence.

When an air flow passes a line-like structure, for instance a suspension bridge, the interaction between the wind field and the structure will induce forces on the structure. These forces may be divided into four parts.

1. Static wind forces from the mean wind
2. Fluctuating forces from vortex shedding in the wake of the structure
3. Fluctuating forces from buffeting due to turbulent wind
4. Motion induced forces due to interaction between the wind field and the motion of the structure

This thesis will consider the motion induced forces. These forces are highly relevant for suspension bridges as they are flexible structures where the vibration frequencies and the aerodynamic damping terms are strongly dependent on the wind velocity [5].

Continuing the modal frequency approach from Chapter 2.1, the structural displacement is represented by generalized degrees of freedom as the sum of products between the time invariant mode shapes  $\phi(x)$  and modal coordinates  $\eta(t)$ .

$$r(t) = \sum_{i=1}^{N_{mod}} \phi_i(x)\eta_i(t) = \mathbf{\Phi}(x)\boldsymbol{\eta}(t) \quad (6)$$

$\mathbf{\Phi}(x)$  is the matrix that contains the eigenmodes, and  $\boldsymbol{\eta}(t)$  is the vector of generalized coordinates. The dynamic equilibrium equation in the modal frequency domain is given as [18]

$$\widetilde{\mathbf{M}}_n \ddot{\eta} + \widetilde{\mathbf{C}}_n \dot{\eta} + \widetilde{\mathbf{K}}_n \eta = \widetilde{\mathbf{Q}} + \widetilde{\mathbf{Q}}_n^{se}(t) \quad (7)$$

where  $\widetilde{\mathbf{M}}_n$  is the modal mass,  $\widetilde{\mathbf{C}}_n$  is the modal damping,  $\widetilde{\mathbf{K}}_n$  is the modal stiffness,  $\widetilde{\mathbf{Q}}_n(t)$  is the modal loading from the self-excited forces, and  $\widetilde{\mathbf{Q}}$  is the wind-load contributions except the self excited forces. See the definitions below.

$$\widetilde{\mathbf{M}}_n = \int_L \phi_n(x)^T m(x) \phi_n(x) dx \quad (8)$$

$$\widetilde{\mathbf{C}}_n = 2\zeta_n \omega_n \widetilde{\mathbf{M}}_n \quad (9)$$

$$\widetilde{\mathbf{K}}_n = \widetilde{\mathbf{M}}_n \omega_n^2 \quad (10)$$

$$\widetilde{\mathbf{Q}}_n^{se} = \int_L \phi_n(x)^T q_n^{se} dx \quad (11)$$

where  $n = y, z, \theta$  and refers to the lateral, vertical and rotational generalized degrees of freedom. See Equations 12, 13, and 14.  $\omega_n$  is the natural frequency, and  $\zeta_n$  is the structural damping of the still-air mode n, and  $m(x)$  is the mass per unit length. The equations defining the self-excited forces in the three generalized degrees of freedom (DOF) are given below [12]

$$q_y^{se} = \frac{1}{2}\rho V^2 \left( KP_1^* \frac{\dot{r}_y}{V} + KP_2^* \frac{B\dot{r}_\theta}{V} + K^2 P_3^* r_\theta + KP_4^* \frac{r_y}{B} + KP_5^* \frac{\dot{r}_z}{V} + K^2 P_6^* \frac{r_z}{B} \right) \quad (12)$$

$$q_z^{se} = \frac{1}{2}\rho V^2 \left( KH_1^* \frac{\dot{r}_z}{V} + KH_2^* \frac{B\dot{r}_\theta}{V} + K^2 H_3^* r_\theta + KH_4^* \frac{r_z}{B} + KH_5^* \frac{\dot{r}_y}{V} + K^2 H_6^* \frac{r_y}{B} \right) \quad (13)$$

$$q_\theta^{se} = \frac{1}{2}\rho V^2 \left( KA_1^* \frac{\dot{r}_z}{V} + KA_2^* \frac{B\dot{r}_\theta}{V} + K^2 A_3^* r_\theta + KA_4^* \frac{r_z}{B} + KA_5^* \frac{\dot{r}_y}{V} + K^2 A_6^* \frac{r_y}{B} \right) \quad (14)$$

where  $V$  is the mean-wind velocity,  $B$  is the width of the girder, and the reduced frequency  $K = \frac{\omega B}{V}$ .  $P_n^*$ ,  $H_n^*$ , and  $A_n^*$  are the aerodynamic derivatives, explained in Chapter 2.3.

By Fourier- transforming the equation of motion in Equation 7, we obtain the dynamic equilibrium condition in the frequency domain [3,18]

$$(\tilde{\mathbf{M}}_i \omega^2 + \tilde{\mathbf{C}}_i i\omega + \tilde{\mathbf{K}}_i) a_{\eta_i} = a_{\tilde{Q}} + a_{\tilde{Q}_i^{se}} \quad (15)$$

where  $a_{\eta_i}(\omega)$  and  $a_{\tilde{Q}_i^{se}}$  are the Fourier amplitudes of  $\eta_i(t)$  and  $Q_{ae}(t)$ , and  $i$  is the imaginary unit.

As Equations 12, 13, and 14 illustrates, the force contains terms that are proportional to, and in phase with, the structural displacement and velocity. Hence, the Fourier-amplitude of the self- excited forces also contains these proportional terms, respectively  $k_{ae}$ ,  $c_{ae}$  and  $m_{ae}$ .  $a_{\tilde{Q}_i^{se}}$  can now be expressed as

$$a_{\tilde{Q}_i^{se}} = (\tilde{\mathbf{C}}_{ae_i} \omega + \tilde{\mathbf{K}}_{ae_i}) a_{\eta_i} \quad (16)$$

Combining Equations 15 and 16, and re-arranging all terms to the left side, we obtain the equation of motion in frequency domain, including the self-excited forces

$$[\tilde{\mathbf{M}}_0 \omega^2 + i\omega(\tilde{\mathbf{C}}_0 - \tilde{\mathbf{C}}_{ae}) + (\tilde{\mathbf{K}}_0 - \tilde{\mathbf{K}}_{ae})] a_{\eta_i} = a_{\tilde{Q}} \quad (17)$$

As Equation 17 demonstrates, the self excited loads from the wind will affect the structural properties of the system through the matrices  $\mathbf{K}_{ae}$  and  $\mathbf{C}_{ae}$ . The change in damping and stiffness of the structure will also change the eigenfrequencies as the wind velocity increases.

## 2.3 Aerodynamic derivatives

The aerodynamic derivatives depend on the external shape of the bridge deck, and are usually determined through wind-tunnel tests. The ADs are coefficients that describes

the motion induced dynamic forces that occurs from interaction between the oscillations of the bridge deck and the wind flow.

The theoretical expressions for the aerodynamic instabilities and the mechanism of flutter, was first developed by Theodorsen [20] for thin air foils in the 1920's and 1930's. The problem of aerodynamic instabilities first occurred within the field of aeronautics, where instability caused by interaction of the air flow and the wings of air-planes was observed. In 1971 R. Scanlan and J. Tomko re-launched Theodorsen's theory but now with the experimental AD coefficients for a flat plate, applied within bridge aerodynamics. [13, 21].

The aerodynamic derivatives provides a description of the interacting forces between the wind flow and the oscillating structure. The ADs are described as non-dimensional functions of the mean wind velocity and the oscillating frequency of the bridge deck.

There are in total 18 AD terms, when including modes in the vertical, lateral and the torsional degree of freedom of the bridge deck. The different terms are proportional to deflection and velocity- terms of the bridge deck. Hence, it is convenient to implement them as aerodynamic coefficient matrices in the equation of motion.

In many aerodynamic stability analyses the in-wind lateral degrees of freedom has been omitted, and therefore the non-zero terms of the ADs are reduced to 8;  $H_i^*$  and  $A_i^*$ ,  $i = 1 - 4$ . This is the case for Theodorsen's ADs, and will be further deliberated in Chapter 2.5.4 and 2.5.5.

In Equation 17,  $\tilde{\mathbf{K}}_{ae}$  and  $\tilde{\mathbf{C}}_{ae}$  is the coefficient matrices that describes the self excited forces in Equation 12, 13, and 14. The matrices are given as the  $N_{mod} * N_{mod}$  matrices

$$\begin{bmatrix} \ddots & & & \\ & \tilde{K}_{aeij} & & \\ & & \ddots & \\ & & & \ddots \end{bmatrix} \text{ and } \begin{bmatrix} \ddots & & & \\ & \tilde{C}_{aeij} & & \\ & & \ddots & \\ & & & \ddots \end{bmatrix} \quad (18)$$

and the elements on row i and column j is given as

$$\begin{bmatrix} \tilde{K}_{aeij} \\ \tilde{C}_{aeij} \end{bmatrix} = \int_L \begin{bmatrix} \phi_i^T \mathbf{K}_{ae} \phi_j \\ \phi_i^T \mathbf{C}_{ae} \phi_j \end{bmatrix} dx \quad (19)$$

Adopting the notations for  $\mathbf{K}_{ae}$  and  $\mathbf{C}_{ae}$  from Scanlan and Tomko [21]

$$\mathbf{K}_{ae} = \frac{\rho B^2}{2} \omega^2 \begin{bmatrix} P_4^* & P_6^* & BP_3^* \\ H_6^* & H_4^* & BH_3^* \\ BA_6^* & BA_4^* & B^2 A_3^* \end{bmatrix} \text{ and } \mathbf{C}_{ae} = \frac{\rho B^2}{2} \omega \begin{bmatrix} P_1^* & P_5^* & BP_2^* \\ H_5^* & H_1^* & BH_2^* \\ BA_5^* & BA_1^* & B^2 A_2^* \end{bmatrix} \quad (20)$$

The non- dimensional coefficients in the  $\mathbf{K}_{ae}$  and  $\mathbf{C}_{ae}$  are functions of both the frequency of motion and the mean wind velocity. The  $A_k^*$ ,  $H_k^*$ , and  $P_k^*$ ,  $k = 1 - 6$  denotes the

aerodynamic derivatives associated with motion in torsional, cross- wind, and along-wind directions, respectively. As the ADs are coefficient describing the forces from the wind flow that acts on the bridge deck, they may be measured in wind tunnel tests. This will be further deliberated in chapter 6. A different approach to obtain the ADs is to derive them from the buffeting theory [17]. The quasi-static aerodynamic derivatives are given as

$$\begin{bmatrix} P_1^* & H_1^* & A_1^* \\ P_2^* & H_2^* & A_2^* \\ P_3^* & H_3^* & A_3^* \\ P_4^* & H_4^* & A_4^* \\ P_5^* & H_5^* & A_5^* \\ P_6^* & H_6^* & A_6^* \end{bmatrix} = \begin{bmatrix} -2\bar{C}_D \frac{D}{B} \frac{V}{B\omega(V)} & -(C'_L + \bar{C}_D \frac{D}{B}) \frac{V}{B\omega} & -C'_M \frac{V}{B\omega} \\ 0 & 0 & 0 \\ C'_D \frac{D}{B} (\frac{V}{B\omega})^2 & C'_L (\frac{V}{B\omega})^2 & C'_M (\frac{V}{B\omega})^2 \\ 0 & 0 & 0 \\ (\bar{C}_L - C'_D \frac{D}{B}) \frac{V}{B\omega} & -2\bar{C}_L \frac{V}{B\omega} & -2\bar{C}_M \frac{V}{B\omega} \\ 0 & 0 & 0 \end{bmatrix} \quad (21)$$

As illustrated above the ADs are expressed as functions of the dimensionless reduced velocity  $\tilde{V}_i = \frac{V}{B\omega}$ .  $\omega$  denotes the oscillating frequency of the system. The terms  $\bar{C}_D, \bar{C}_L, \bar{C}_M$  is the quasi-static drag, lift and moment coefficients, and  $C'_D, C'_L, C'_M$  are the rates of change of the respective load coefficients as the angle of rotation of the bridge deck increases.

## 2.4 Theodorsen's aerodynamic derivatives

The Norwegian- American Theodore Theodorsen was the first to develop analytical aerodynamic derivatives for a flat plate section. There has been made a series of assumptions in the derivation of Theodorsen's ADs. It has been assumed that at least two degrees of freedom are required to create a condition of instability. The wind forces acting on the section is derived from non-stationary potential flow theory. Large oscillatory motions are neglected, considering only the small oscillations around a state of equilibrium. These assumptions still allow the description of unstable conditions in the interaction between the wind and the section. In Theodorsen's theory there has not been made any efforts to adapt the derivatives to different section shapes, as they purely seek to describe the mechanism of flutter, not secondary effects like section shape [20].

In this thesis, Theodorsen's flutter derivatives has been adopted to the triple girder section. This is because of the lack of aerodynamic derivatives extracted from experimental tests for similar sections, and for a sufficiently high reduced velocity range.

Theodorsen's derivatives are stated below

$$\begin{bmatrix} H_1^* & A_1^* \\ H_2^* & A_2^* \\ H_3^* & A_3^* \\ H_4^* & A_4^* \end{bmatrix} = \begin{bmatrix} -2\pi F \tilde{V}_i & -\frac{\pi}{2} F \tilde{V}_i \\ \frac{\pi}{2} (1 + F + 4G \tilde{V}_i) \tilde{V}_i & -\frac{\pi}{8} (1 - F - 4G \tilde{V}_i) \tilde{V}_i \\ 2\pi (F \tilde{V}_i - \frac{G}{4}) \tilde{V}_i & \frac{\pi}{2} (F \tilde{V}_i - \frac{G}{4}) \tilde{V}_i \\ \frac{\pi}{2} (1 + 4G \tilde{V}_i) & \frac{\pi}{2} G \tilde{V}_i \end{bmatrix} \quad (22)$$

where  $\tilde{V}_i = \frac{V}{B\omega}$  is the reduced velocity, and

$$F\left(\frac{\hat{\omega}}{2}\right) = \frac{J_1(J_1 + Y_0) + Y_1(Y_1 - J_0)}{(J_1 + Y_0)^2 + (Y_1 - J_0)^2} \quad (23)$$

$$G\left(\frac{\hat{\omega}}{2}\right) = -\frac{J_1 J_0 + Y_1 Y_0}{(J_1 + Y_0)^2 + (Y_1 - J_0)^2} \quad (24)$$

$F$  and  $G$  are the real and imaginary parts of the so-called Theodorsen's circulatory function.  $J_n(\omega)$  and  $Y_n(\omega)$  are the Bessel functions of first and second kind, with order  $n$  [5, 17].

## 2.5 Motion induced instabilities

Both static and dynamic forces will cause instability of a structure as the load magnitude increases beyond the capacity of the system. As the wind loads increase the response will be dominated by load contributions from the motion induced loads in Chapter 2.2. If the load magnitude continues to increase throughout the domain of motion induced loads, instabilities will occur. An instability is defined as the stage where an incremental increase of the load will cause a large increase in the response. For long-span bridges we separate between four instability phenomena

- Static divergence
- Galloping
- Instability in pure torsion
- Flutter

As it emerged in the end of Chapter 2.2, Equation 17 is the equation of motion that describes the force equilibrium of an oscillating structure subject to self excited forces. Continuing to derive the equations in the modal frequency domain, and introducing modal stiffness and Rayleigh damping [18]

$$\mathbf{K}_0 = \omega_n^2 \mathbf{M} \quad (25)$$

$$\mathbf{C}_0 = 2\zeta_i \omega_n \mathbf{M} \quad (26)$$

Combining Equations 17, 25, and 26 we obtain

$$\left[ \left(\frac{\omega}{\omega_n}\right)^2 + (2i\omega \cdot \text{diag}\left(\frac{1}{\omega_n}\right)(\zeta_i - \zeta_{ae}) + \left(\mathbf{I} - \frac{\mathbf{K}_{ae}}{\omega_n^2 \mathbf{M}}\right)) \right] a_\eta = a_{\bar{Q}} \quad (27)$$

$\omega$  is the oscillating frequency of the structure, and  $\omega_n$  is the zero-wind frequency of mode  $n$ . This gives us the load- relation

$$a_\eta = \hat{H}_\eta a_{\bar{Q}} \quad (28)$$

$$\hat{H}_\eta = \frac{1}{\left(\frac{\omega}{\omega_n}\right)^2 + (2i\omega \cdot \text{diag}\left(\frac{1}{\omega_n}\right)(\zeta_i - \zeta_{ae}) + (\mathbf{I} - \kappa_{aeij}))} = \frac{1}{\hat{\mathbf{E}}_\eta} \quad (29)$$

where  $\kappa_{aeij} = \frac{\mathbf{K}_{ae}}{\omega_i^2 \tilde{\mathbf{M}}}$ ,  $\mathbf{I}$  is the  $N_{mod} \times N_{mod}$  identity matrix and

$$\hat{\mathbf{E}}_\eta = \left(\frac{\omega}{\omega_n}\right)^2 + (2i\omega \cdot \text{diag}\left(\frac{1}{\omega_n}\right))(\zeta_i - \zeta_{ae}) + (\mathbf{I} - \kappa_{aeij}) \quad (30)$$

$\hat{\mathbf{E}}_\eta$  is the impedance matrix. As it appears in Equations 28 and 30 the response of the structure will diverge if

$$\left| \det(\hat{\mathbf{E}}_\eta) \right| = 0 \quad (31)$$

Combining Equations 8, 19 and 30, we obtain

$$\kappa_{aeij} = \frac{\tilde{\mathbf{K}}_{aeij}}{\omega^2 \tilde{\mathbf{M}}_i} = \frac{\rho B^2}{2\tilde{m}_i} \left(\frac{\omega}{\omega_i}\right)^2 \frac{\int_{L_{exp}} (\phi_i^T \tilde{\mathbf{K}}_{ae} \phi_j) dx}{\int_L (\phi_i^T \phi_i) dx} \quad (32)$$

$$\zeta_{aeij} = \frac{\omega_i}{2} \frac{\tilde{\mathbf{C}}_{aeij}}{\omega^2 \tilde{\mathbf{M}}_i} = \frac{\rho B^2 \omega}{4\tilde{m}_i \omega_i} \frac{\int_{L_{exp}} (\phi_i^T \tilde{\mathbf{C}}_{ae} \phi_j) dx}{\int_L (\phi_i^T \phi_i) dx} \quad (33)$$

$\omega$  is the in-wind eigenfrequency of the system. The eigenfrequencies changes as the wind- load increases because the wind-load changes the structural damping- and stiffness properties through  $\mathbf{K}_{ae}$  and  $\mathbf{C}_{ae}$ .  $\omega_i$  is the zero-wind eigenfrequency of mode  $i$ .

All types of dynamic instability may be analysed through the impedance matrix. The solution of Equation 31 will give  $N_{mod}$  stability limits, associated with the modes included in the impedance matrix. Since the impedance- matrix contains both real and complex terms, Equation 31 will provide two conditions that has to be satisfied simultaneously.

$$\text{Re}(\det(\tilde{\mathbf{E}}_\eta)) = 0 \quad (34)$$

$$\text{Im}(\det(\tilde{\mathbf{E}}_\eta)) = 0 \quad (35)$$

Finding these instability limits are iterative procedures, as the solutions relies on both the mean wind velocity  $V$  and the in-wind critical frequency  $\omega$ .

### 2.5.1 Static divergence

Static divergence is a instability phenomenon where the in-wind natural frequency of a mode decreases to zero as the wind velocity increases. This is a static instability in torsion that occurs because of loss of torsional stiffness. As the negative aerodynamic stiffness in torsion achieves the same magnitude as the structural zero-wind stiffness, the net stiffness term in Equation 17 will become zero in torsion, and the structure will become unstable.

Setting  $\omega = 0$  reduces the impedance matrix to

$$\tilde{\mathbf{E}}_\eta(\omega = 0, V_{cr}) = 1 - \kappa_{ae\theta\theta} \quad (36)$$

$V_{cr}$  is the critical mean wind velocity at which static divergence occurs.

As the critical frequency drop to zero for static divergence, the derivation of the stability limit uses quasi-steady theory. If we consider the quasi-static flat-plate derivations of the aerodynamic derivatives are given in [17], and the only non-zero terms in the quasi-static case are [18]

$$\begin{bmatrix} H_1^* & A_1^* \\ H_3^* & A_3^* \end{bmatrix} = \begin{bmatrix} -2\pi\hat{V}_i & -\frac{\pi}{2}\hat{V}_i \\ 2\pi\hat{V}_i^2 & \frac{\pi}{2}\hat{V}_i^2 \end{bmatrix} \quad (37)$$

Since the only modal degree of freedom relevant for static divergence is the torsional twist of the bridge deck, the modal vector is assumed as  $\phi_i = [0, 0, \phi_{\theta_i}]^T$ . The impedance matrix is therefore

$$\tilde{\mathbf{E}}_{\eta}(\omega = 0, V_{cr}) = 1 - \kappa_{ae\theta\theta} = 1 - \frac{\rho B^2 \omega \int_{L_{exp}} (\phi_{\theta}^T \tilde{K}_{ae} \phi_{\theta}) dx}{2\tilde{m}_{\theta\theta} \omega_{\theta}^2 \int_L (\phi_{\theta}^T \phi_{\theta}) dx} \quad (38)$$

The numerator  $\int_{L_{exp}} \phi_{\theta}^T \tilde{K}_{ae} \phi_{\theta} dx$  reduces to  $A_3^* \int_{L_{exp}} \phi_{\theta}^2 dx$  because of the zero-terms in the eigenvector and the quasi-static derivatives listed above.

$$\frac{\rho B^2 \omega}{2\tilde{m}_{\theta\theta} \omega_{\theta}^2} A_3^* \frac{\int_{L_{exp}} \phi_{\theta}^2 dx}{\int_L \phi_{\theta}^2 dx} = 1 \quad (39)$$

Extracting the quasi-static  $A_3^*$  term from Equation 21, we can solve Equation 38 with respect to  $V_{cr}$ , obtaining the critical velocity for static divergence.

$$V_{cr} = B\omega_{\theta} \sqrt{\frac{2\tilde{m}_{\theta}}{\rho B^4 C'_M} \frac{\int_L \phi_{\theta}^2 dx}{\int_{L_{exp}} \phi_{\theta}^2 dx}} \quad (40)$$

### 2.5.2 Galloping

Galloping is an unstable behaviour that only contains oscillating motion perpendicular to the wind direction. Galloping occurs due to negative aerodynamic damping.

The modal vector describing the galloping behaviour is  $\phi_i = [0, \phi_{z_i}, 0]^T$ . The resonant frequency  $\omega_r$  will equal the frequency of the first natural frequency in the vertical z-direction.

$$\omega_r = \omega_z \quad (41)$$

Since the galloping phenomena contains a dynamic behaviour, the natural frequencies are no longer equal to the zero-air natural frequencies. The frequencies change as the wind velocity  $V_{cr}$  and the frequency of oscillation  $\omega_i$  increases. In the case of galloping, the impedance matrix is reduced to

$$\hat{E}_{\eta} = \left(\frac{\omega}{\omega_z}\right)^2 + (2i\omega \cdot \text{diag}\left(\frac{1}{\omega_z}\right)(\zeta_z - \zeta_{aezz})) + (1 - \kappa_{aezz}) \quad (42)$$



Deriving  $\kappa_{ae}$  and  $\zeta_{ae}$  for the pure vertical motion

$$\kappa_{ae_{zz}} = \frac{\rho B^2}{2\tilde{m}_{zz}} \left( \frac{\omega_r}{\omega_z} \right)^2 H_4^* \frac{\int_{L_{exp}} \phi_z^2 dx}{\int_L \phi_z^2 dx} \quad (43)$$

$$\zeta_{ae_{zz}} = \frac{\rho B^2}{4\tilde{m}_{zz}} \frac{\omega_r}{\omega_z} H_1^* \frac{\int_{L_{exp}} \phi_z^2 dx}{\int_L \phi_z^2 dx} \quad (44)$$

Setting both the real and the imaginary parts of Equation 42 equal to zero, we obtain the in-wind resonance frequency and the corresponding damping ratio

$$\omega_r = \frac{\omega_z}{\sqrt{1 + \frac{\rho B^2}{2\tilde{m}_z} H_4^* \frac{\int_{L_{exp}} \phi_z^2 dx}{\int_L \phi_z^2 dx}}} \quad (45)$$

$$\zeta_{ae_{zz}} = \frac{\rho B^2}{4\tilde{m}_z} \frac{\omega_r}{\omega_z} H_1^* \frac{\int_{L_{exp}} \phi_z^2 dx}{\int_L \phi_z^2 dx} \quad (46)$$

The galloping instability is caused by negative net damping in the structure, meaning that the term  $(\zeta_{0_{zz}} - \zeta_{ae_{zz}}) < 0$ . This means that for galloping to occur,  $\zeta_{ae_{zz}} > 0$ . Analysing the expression given in Equation 44, we see that galloping can only occur if  $H_1^*$  attains positive values.

It is seen in Equation 22 that in the Theodorsen's aerodynamic derivatives  $H_1^*$  is consequently negative, and therefore galloping cannot occur for a flat plate section.

Setting Equation 53 equal to the zero- wind structural damping  $\zeta_{0_{zz}}$  and extracting  $H_1^*$  from Equation 21, we obtain the critical wind velocity for galloping

$$V_{cr} = B\omega_z \frac{\zeta_{0_{zz}}}{-(C'_L + \bar{C}_D \frac{D}{B})} \frac{4\tilde{m}_z}{\rho B^2} \frac{\int_L \phi_z^2 dx}{\int_{L_{exp}} \phi_z^2 dx} \quad (47)$$

### 2.5.3 Instability in pure torsion

Pure torsional instability is a single- mode instability caused by negative damping in the lowest torsional degree of freedom. For modern contemporary suspension and cable stayed bridges, this mode is expected to be the first symmetric torsion mode [13]. The mathematical derivations of the stability limit in torsion has several similarities as the galloping equations, since both phenomena is single-mode instabilities.

In the pure torsional case, the only mode shape vector is  $\phi_i = [0, 0, \phi_{\theta_i}]^T$ . The resonant frequency  $\omega_r$  will equal the frequency of the first natural frequency in torsion.

$$\omega_r = \omega_{\theta} \quad (48)$$

The impedance matrix is now given as

$$\hat{E}_\eta = \left(\frac{\omega}{\omega_\theta}\right)^2 + 2i(\omega \cdot \text{diag}\left(\frac{1}{\omega_\theta}\right))(\zeta_\theta - \zeta_{ae\theta\theta}) + (1 - \kappa_{ae\theta\theta}) \quad (49)$$

Deriving  $\kappa_{ae}$  and  $\zeta_{ae}$  for the pure torsional motion

$$\kappa_{ae\theta\theta} = \frac{\rho B^2}{2\tilde{m}_{\theta\theta}} \left(\frac{\omega_r}{\omega_\theta}\right)^2 A_3^* \frac{\int_{Lexp} \phi_\theta^2 dx}{\int_L \phi_\theta^2 dx} \quad (50)$$

$$\zeta_{ae\theta\theta} = \frac{\rho B^2}{4\tilde{m}_{\theta\theta}} \frac{\omega_r}{\omega_\theta} A_2^* \frac{\int_{Lexp} \phi_\theta^2 dx}{\int_L \phi_\theta^2 dx} \quad (51)$$

Setting both the real and the imaginary parts of Equation 49 equal to zero, we obtain the in-wind resonance frequency and the corresponding damping ratio

$$\omega_r = \frac{\omega_\theta}{\sqrt{1 + \frac{\rho B^2}{2\tilde{m}_\theta} A_3^* \frac{\int_{Lexp} \phi_\theta^2 dx}{\int_L \phi_\theta^2 dx}}} \quad (52)$$

$$\zeta_{ae\theta\theta} = \frac{\rho B^2}{4\tilde{m}_\theta} \frac{\omega_r}{\omega_\theta} A_2^* \frac{\int_{Lexp} \phi_\theta^2 dx}{\int_L \phi_\theta^2 dx} \quad (53)$$

Similar to galloping, it is now seen that instability in torsion can only occur for positive values of  $A_2^*$ . As Equation 21 and 22 demonstrates, the  $A_2^*$ - values are consequently equal to zero in the quasi-static case, and always negative for a flat plate section. The ADs for single mode torsional flutter must therefore be found experimentally through wind-tunnel testing. The  $A_2^*$ - values of streamlined bridge decks are in general negative. Bluff sections might achieve positive  $A_2^*$ - values due to its ability to create large edge vortices that will enlarge the torsional oscillations [5, 13].

#### 2.5.4 Bimodal flutter

Flutter is an instability mechanism where the vertical and torsional modes couple in to one dynamic deflection shape. This coupling occurs via the off-diagonal terms  $\kappa_{ae\theta z}$  and  $\kappa_{aez\theta}$ , and are therefore strongly dependent on the mode shape similarity through the integrals in Equation 32 and 33.

Flutter is a phenomenon that involves positive feedback of the forces in the system. The interaction between the oscillating structure and the wind flow will evolve such that the wind is adding more energy to the system than the structural damping can dissipate. This means that  $\zeta_0 - \zeta_{ae} < 0$  i.e the system damping is negative.

Coupled flutter will occur in structures where the first vertical natural frequency is lower than the first torsional,  $f_z^1 < f_\theta^1$ . This is because the self excited load terms, containing the aerodynamic derivatives, tend to reduce the torsional stiffness as the mean wind velocity increases [5]. Hence the in-wind natural frequency of the torsional mode will decrease

towards the natural frequency of the vertical mode. Coupling occurs when the frequencies couple together, and form a coupled flutter oscillation.

Considering only the two simplified modes  $\phi_z = [0, \phi_z, 0]$  and  $\phi_\theta = [0, 0, \phi_\theta]$  we obtain the bimodal impedance matrix

$$\hat{\mathbf{E}}_\eta(\omega_r, V_{cr}) = \begin{bmatrix} 1 & 0 \\ 0 & 1 \end{bmatrix} - \begin{bmatrix} \kappa_{aezz} & \kappa_{aez\theta} \\ \kappa_{ae\theta z} & \kappa_{ae\theta\theta} \end{bmatrix} - \begin{bmatrix} \left(\frac{\omega_r}{\omega_z}\right)^2 & 0 \\ 0 & \left(\frac{\omega_r}{\omega_\theta}\right)^2 \end{bmatrix} + 2i \begin{bmatrix} \frac{\omega_r}{\omega_z} & 0 \\ 0 & \frac{\omega_r}{\omega_\theta} \end{bmatrix} \begin{bmatrix} \zeta_z - \zeta_{aezz} & -\zeta_{aez\theta} \\ -\zeta_{ae\theta z} & \zeta_\theta - \zeta_{ae\theta\theta} \end{bmatrix} \quad (54)$$

The terms in Equation 54 are given as

$$\begin{aligned} \kappa_{aezz} &= \frac{\rho B^2}{2\tilde{m}_z} \left(\frac{\omega_r}{\omega_z}\right)^2 H_4^* \frac{\int_{L_{exp}} \phi_z^2 dx}{\int_L \phi_z^2 dx} & \kappa_{aez\theta} &= \frac{\rho B^3}{2\tilde{m}_z} \left(\frac{\omega_r}{\omega_z}\right)^2 H_3^* \frac{\int_{L_{exp}} \phi_z \phi_\theta dx}{\int_L \phi_z^2 dx} \\ \kappa_{ae\theta z} &= \frac{\rho B^3}{2\tilde{m}_\theta} \left(\frac{\omega_r}{\omega_\theta}\right)^2 A_4^* \frac{\int_{L_{exp}} \phi_\theta \phi_z dx}{\int_L \phi_\theta^2 dx} & \kappa_{ae\theta\theta} &= \frac{\rho B^4}{2\tilde{m}_\theta} \left(\frac{\omega_r}{\omega_\theta}\right)^2 A_4^* \frac{\int_{L_{exp}} \phi_\theta^2 dx}{\int_L \phi_\theta^2 dx} \\ \zeta_{aezz} &= \frac{\rho B^2 \omega_r}{4\tilde{m}_z \omega_z} H_1^* \frac{\int_{L_{exp}} \phi_z^2 dx}{\int_L \phi_z^2 dx} & \zeta_{aez\theta} &= \frac{\rho B^3 \omega_r}{4\tilde{m}_z \omega_z} H_2^* \frac{\int_{L_{exp}} \phi_z \phi_\theta dx}{\int_L \phi_z^2 dx} \\ \zeta_{ae\theta z} &= \frac{\rho B^3 \omega_r}{4\tilde{m}_\theta \omega_\theta} A_2^* \frac{\int_{L_{exp}} \phi_\theta \phi_z dx}{\int_L \phi_\theta^2 dx} & \zeta_{ae\theta\theta} &= \frac{\rho B^4 \omega_r}{4\tilde{m}_\theta \omega_\theta} A_1^* \frac{\int_{L_{exp}} \phi_\theta^2 dx}{\int_L \phi_\theta^2 dx} \end{aligned} \quad (55)$$

To analyse the instability of bimodal flutter, we set the real and the imaginary part of the bimodal impedance matrix equal to zero. To get both the real and the imaginary part equal to zero simultaneously will demand iterations, since we can not read off the aerodynamic derivatives without knowing the mean-wind velocity and the in-wind frequency.

$$Re[\hat{\mathbf{E}}_\eta] = 0 \quad Im[\hat{\mathbf{E}}_\eta] = 0 \quad (56)$$

Solving the two expressions in Equation 56 will give tedious calculations. To simplify the expressions the following dimensionless coefficients are established [12]

$$\psi_{z\theta} = \frac{\int_{L_{exp}} \phi_z \phi_\theta dx}{\int_L \phi_z^2 dx} \frac{\int_{L_{exp}} \phi_z \phi_\theta dx}{\int_L \phi_\theta^2 dx} \quad (57)$$

$$\chi_z = \frac{\rho B^2}{\tilde{m}_z} \quad \chi_\theta = \frac{\rho B^4}{\tilde{m}_\theta} \quad (58)$$

$$\gamma = \frac{\omega_\theta}{\omega_z} \quad \hat{V} = \frac{V}{B\omega_\theta} \quad \omega_{\hat{C}R} = \frac{\omega_{CR}}{\omega_\theta} \quad (59)$$

The coefficient  $\psi_{z\theta}$  is a measure of the shape wise similarity of the vertical and torsional mode shapes. As mentioned earlier, this is an important measure for coupled flutter to occur. If the mode shapes are similar,  $\psi_{z\theta}$  will be close to one, and flutter may happen. This will in general be the case for the first pairs of vertical and torsional modes. If they are dissimilar, all the off-diagonal terms in the impedance matrix will become close to zero, and coupled flutter may not occur. This will typically be the case when combining asymmetric vertical and symmetric torsion.

Performing the calculations indicated in 56 will give us the characteristic equations for the real and the imaginary part

$$R_4 \hat{\omega}_{cr}^4 + R_3 \hat{\omega}_{cr}^3 + R_2 \hat{\omega}_{cr}^2 + 1 = 0 \quad (60)$$

$$I_3 \hat{\omega}_{cr}^3 + I_2 \hat{\omega}_{cr}^2 + I_1 \hat{\omega}_{cr} + \xi_z \gamma + \xi_\theta = 0 \quad (61)$$

where the coefficients is expressed as [12, 21]

$$\begin{aligned} R_4 &= \gamma^2 \left[ 1 + \frac{\beta_z}{2} H_4^* + \frac{\beta_\theta}{2} A_3^* + \frac{\beta_z \beta_\theta}{4} \left( A_1^* H_2^* \psi_{z\theta} - A_2^* H_1^* + A_3^* H_4^* - A_4^* H_3^* \psi_{z\theta} \right) \right] \\ R_3 &= \gamma \left( \zeta_\theta \beta_z \gamma h_1^* + \zeta_z \beta_\theta A_2^* \right) \\ R_2 &= - \left( 1 + \gamma^2 + 4\gamma \zeta_z \zeta_\theta + \frac{\beta_z}{2} \gamma^2 H_4^* + \frac{\beta_\theta}{2} A_3^* \right) \\ I_3 &= \gamma^2 \left[ \frac{\beta_z \beta_\theta}{8} \left( H_1^* A_3^* - H_2^* A_4^* \psi_{z\theta} - h_3^* A_1^* \psi_{z\theta} + H_4^* A_2^* \right) + \frac{1}{4} \left( \beta_z H_1^* + \beta_\theta A_2^* \right) \right] \\ I_2 &= - \left[ \zeta_z \left( \frac{\beta_\theta}{2} A_3^* + \gamma \right) + \zeta_\theta \gamma^2 \left( \frac{\beta_z}{2} H_4^* + 1 \right) \right] \\ I_1 &= - \frac{1}{4} \left( \beta_z \gamma^2 H_1^* + \beta_\theta A_2^* \right) \end{aligned} \quad (62)$$

Equations 60 and 61 are solved for the frequency ratio  $\hat{\omega}_{cr}$  where both the real and imaginary part is zero. The roots corresponding to the real and imaginary parts are plotted as a function of the reduced velocity  $\hat{V}$  and frequency ratio  $\hat{\omega}_{cr}$ . The first intersection point between the real and imaginary root defines the critical reduced flutter wind speed.

The critical wind speed and in-wind frequency may now easily be solved from the two dimensionless numbers on the axis of the plot

$$\omega_{cr} = \hat{\omega}_{cr} \omega_\theta \quad (63)$$

$$V_{cr} = \hat{V} B \omega_\theta \quad (64)$$

### 2.5.5 Multi-modal flutter

The bi-modal approach will in many cases give a good approximation to the flutter limit, because the dominant flutter contributions usually comes from one pair of shape

wise similar vertical and torsional modes. The other vibration modes of the structure will, in many cases, also contribute to the flutter limit. Inclusion of several modes may act stabilizing or destabilizing for the flutter limit, depending on their ability to create coupling-forces.

It is recognized that multi-modal approach more accurately predicts the flutter limit, because the actual oscillation of the structure is better described with more than to modes. In multi-modal flutter analysis we no longer assume that each mode shape  $\phi_i$  only has one component, but it contains all three components.

$$\phi_i = [\phi_y, \phi_z, \phi_\theta]^T \quad (65)$$

Including  $N$  mode shapes in the analysis will give us  $N \times N$  coefficient matrices. Allowing each mode shape to have all three entries, will also expand the number of terms in  $\kappa_{aeij}$  and  $\zeta_{aeij}$ . The derivation of coefficient matrices are the same for the multi-modal approach as for the bi-modal approach. Rendering the expressions 19 and 20 in section 2.3, we may obtain the expression for the multi-modal coefficient matrix  $\kappa_{aeij}$

$$\kappa_{aeij} = \frac{\rho B^2}{2} \omega \int_L \begin{bmatrix} \phi_{y,i} \\ \phi_{z,i} \\ \phi_{\theta,i} \end{bmatrix} \begin{bmatrix} P_4^* & P_6^* & BP_3^* \\ H_6^* & H_4^* & BH_3^* \\ BA_6^* & BA_4^* & B^2 A_3^* \end{bmatrix} \begin{bmatrix} \phi_{y,j} & \phi_{z,j} & \phi_{\theta,j} \end{bmatrix} dx \quad (66)$$

which gives us for all the  $N \times N$  entries in the  $\kappa_{ae}$  matrix

$$\begin{aligned} \kappa_{aeij} = \frac{\rho B^2}{2\tilde{m}_{ij}} \omega \int_L \left( P_4^* \phi_{y,i}^T \phi_{y,j} + H_6^* \phi_{z,i} \phi_{y,j} + BA_6^* \phi_{\theta,i} \phi_{y,j} + P_6^* \phi_{y,i} \phi_{z,j} + H_4^* \phi_{z,i} \phi_{z,j} \right. \\ \left. + BA_4^* \phi_{\theta,i} \phi_{z,j} + BP_3^* \phi_{y,i} \phi_{\theta,j} + BH_3^* \phi_{z,i} \phi_{\theta,j} + B^2 A_3^* \phi_{\theta,i} \phi_{\theta,j} \right) dx \end{aligned} \quad (67)$$

The expression for  $\zeta_i$  in Equation 67 will also include more terms in the multi-modal approach, but its derivation is omitted in this thesis.  $\kappa_{aeij}$  was shown here to visualize the increase in terms due to the expansion of the modal vectors.

The eigenvalue problem for the multi-modal flutter analysis may be developed analogous to the bi-modal analysis. As demonstrated above, both the calculations and the derivations will be far more tedious, and for this reason the eigenvalue problem will be demonstrated in a more general approach.

### Complex eigenvalue problem

Rendering the equation of motion in modal form, only considering the self excited forces, here derived earlier in Equation 7.

$$\tilde{\mathbf{M}}_n \ddot{\eta} + (\tilde{\mathbf{C}}_n - \tilde{\mathbf{C}}_{ae}) \dot{\eta} + (\tilde{\mathbf{K}}_n - \tilde{\mathbf{K}}_{ae}) \eta = 0 \quad (68)$$

Assuming that the solution of the response is on the form  $\eta = \psi e^{\lambda t}$ , substituting into 68, we obtain the second order complex eigenvalue problem [3]. The stability of the aeroelastic system, where  $N$  still-air vibration modes are used as generalized degrees-of-freedom, can be predicted considering the following quadratic eigenvalue problem [12].

$$\left( \lambda^2 \tilde{\mathbf{M}}_n + \lambda(\tilde{\mathbf{C}}_n - \tilde{\mathbf{C}}_{ae}) + (\tilde{\mathbf{K}}_n - \tilde{\mathbf{K}}_{ae}) \right) \psi = \mathbf{0} \quad (69)$$

where  $\lambda$  is the eigenvalues and  $\psi$  is the corresponding eigenvectors. The solution to Equation 69 is the eigenvalues  $\lambda_i$  and the corresponding eigenvectors  $\psi$ . The eigenvalues contains the in-wind damping and frequency of the structure.

$$\lambda_i = -\zeta_i \omega_i \pm i \omega_i \sqrt{1 - \zeta_i^2} \quad (70)$$

We clearly see that the real and imaginary parts of the root is

$$\begin{aligned} Re(\lambda_i) &= -\zeta_i \omega_i \\ Im(\lambda_i) &= \omega_i \sqrt{1 - \zeta_i^2} \end{aligned} \quad (71)$$

where  $\omega_i$  and  $\zeta_i$  is the zero-wind eigen-frequency and damping ratio. The real part of Equation 70 corresponds to the system damping. If the real part is positive, it must be because the damping ratio  $\zeta_i$  is negative. Therefore all solutions where  $Re(\lambda) > 0$  corresponds to negative damping, and is the defining criteria for unstable behaviour of the structure. The imaginary part of the eigenvalue corresponds to the in-wind frequencies. All frequencies must be positive, but since the eigenvalues come as complex- conjugated pairs, see Equation 70, we will get both positive and negative frequencies. Flutter occurs when the eigenvalue problem has a zero real part, and a non- zero imaginary part [2]. Figure 1 visualizes the relations between the positive and negative values of the real and imaginary part of the eigenvalues.

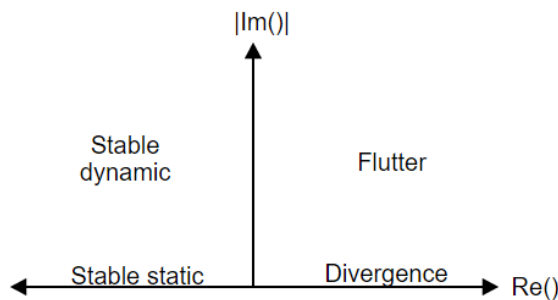


Figure 1: Visualization of system stability depending on the eigenvalues

The solution of the multi-modal flutter analysis requires iterations, and are usually solved graphically because  $\mathbf{C}_{ae}$  and  $\mathbf{K}_{ae}$  are functions of frequency of motion, wind velocity, and the aerodynamic derivatives which are also functions of frequency and velocity. The stability limit for flutter is defined as the lowest wind velocity that attains positive values for the imaginary part and zero for the real part of Equation 71.

Iterations are made for both velocity and frequency. The iterations begins with a selected initial velocity  $V_0$ . For each velocity increment, a frequency iteration will be performed. The iteration starts with the assumption  $\omega_{guess_1} = \omega_0$ , where  $\omega_0$  is the natural frequency of the zero-wind case obtained from the coefficient matrices  $\mathbf{K}_0$ ,  $\mathbf{C}_0$ , and  $\mathbf{M}_0$ . The in-wind coefficient matrices is now developed from the velocity  $V_i$  and the frequency  $\omega_{guess_j}$ , according to Equation 20.  $i$  is the increment number for velocity, and  $j$  the iteration number for frequency, within each velocity increment. Now the eigenfrequencies  $\omega_n$  are solved for the in-wind case, using the polynomial eigenvalue problem described in Equation 69. It is solved using the input parameters  $V_i$  and the frequency  $\omega_{guess_j}$ . Now, the next frequency iteration is performed using the adjusted eigenfrequency,  $\omega_n$  from the previous step as the  $\omega_{guess}$  for the next step.

$$\omega_{guess_{j+1}} = \omega_{omega_j} \quad (72)$$

The frequency iteration for each velocity increment is completed when

$$\omega_j = \omega_{guess_j} \quad (73)$$

The same procedure is then made for the next velocity increment  $V = V + dV$ .

As described above, the solution to the eigenvalue problem has a real and an imaginary part, see Equation 70 and 71. These parts are plotted for the increasing mean wind velocities. See Figure 2 for the development of the imaginary part of the solution of the complex eigenvalue problem, corresponding to oscillation frequencies, as the wind speed picks up.

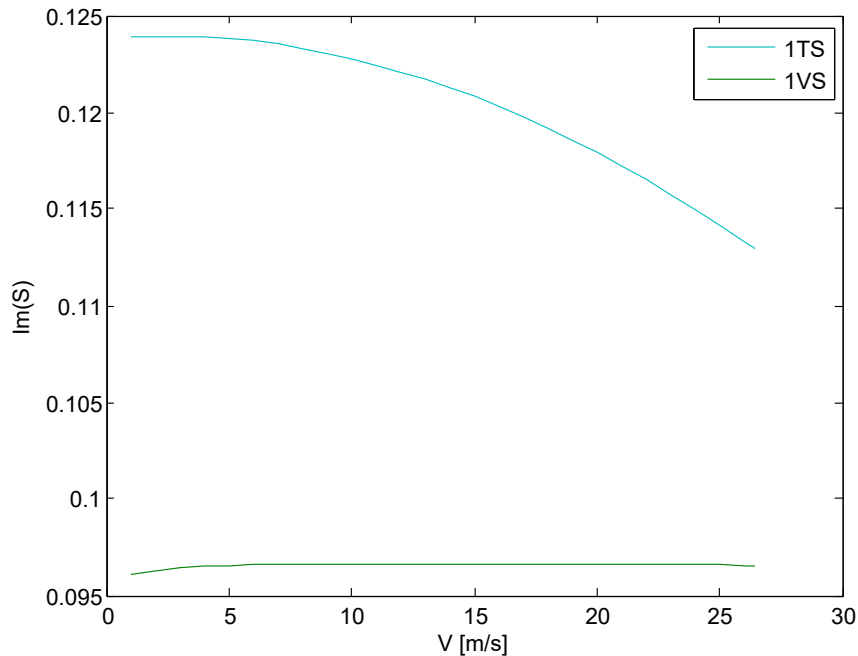


Figure 2: Real part of complex eigenvalue solution corresponding to in- wind frequencies.

As can be seen in the plots, both the real and the imaginary parts of the solution, being the in- wind damping ratio and frequencies, respectively, changes as the mean wind velocity  $V$  increases. The flutter limit is defined as the first point where the system damping turns negative.

### 3 Numerical models

One of the main purposes of this thesis is to develop a general script for creating finite element models (FE-models) of suspension bridge setups. The modal results from the FE-model is used to calculate the aerodynamic stability limits for a variety of suspension bridges by a MATLAB- script that is provided by supervisor Ole Øiseth.

#### 3.1 FE-model

The FE- model is made through a MATLAB- script that accepts certain input parameters to describe a suspension bridge. This makes it easy for the analyst to change parameters in specific analyses. The model may easily be modified to describe a variety of suspension bridges. This is in big contrast to the traditional way of making FE-models of bridges, where it would be time consuming to make large changes of the model geometry. The suspension bridge is very applicable for such a generic modelling technique as the geometry is easily described by a small number of parameters.

The model has been programmed in MATLAB, where a script that accepts certain input parameters automatically creates an Abaqus model of a single-, double-, or triple- girder suspension bridge, according to the input parameters. Abaqus is an advanced tool for performing finite element simulations within several engineering- and mechanical- disciplines. The Abaqus Solver uses an input text file that describes the entire model and type of simulation, to run an analysis. The mentioned MATLAB script writes this input file from the selected input parameters.

##### **master\_script.m**

The master script is the user inter-phase of the MATLAB program that has been made. In this script the analyst must specify the necessary parameters to describe the geometry and the mechanical properties of the bridge.

Table 1: Input parameters suspension bridge code

---

L	Length of mid span
L_side	Length of side span
d	Horizontal c-c distance between main and side girders
e_vert	Vertical distance between main- and side- girder
D	Horizontal distance between cables mid span
D_pylon	Horizontal distance between cables over pylons
subheight	distance from pylon- bottom to girder
hangers	Numbers of hanger- pairs in the main span
number of girders	Number of girders for the bridge. The values 1, 2 and 3 are accepted
girder_sag	Positive sag of girder ("Girder height") before gravity is applied
h	Vertical distance from horizon to cable ("Cable height")before gravity
sag	Cable sag before gravity is applied.

---



Table 2: Mechanical properties that must be defined by the analyst for each main structural part of the bridge. See Figure 5 for axis definition.

A	Area of cross section
$I_y$	Moment of inertia for bending about the n1-axis
$I_{zy}$	Moment of inertia for cross bending
$I_z$	Moment of inertia for bending about the n2-axis
$I_t$	Torsional constant
E	Young's modulus
G	Torsional shear modulus, G
m	Mass per unit length

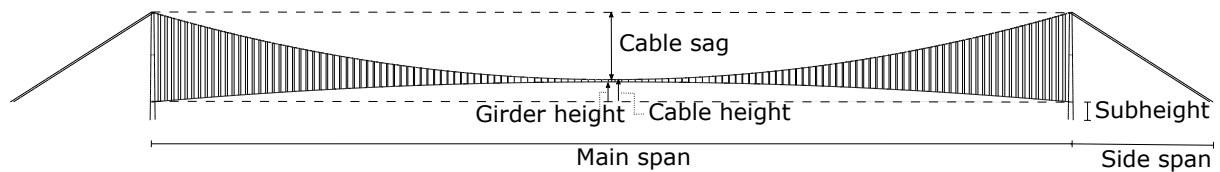


Figure 3: Main parameters of the suspension bridge. Undeformed geometry.

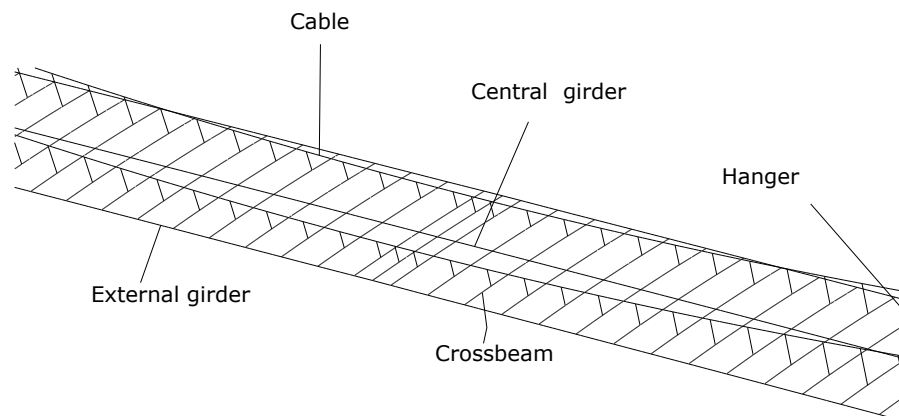


Figure 4: Main elements of the triple-girder suspension bridge.

The parameters in Table 1 creates the undeformed geometry the suspension bridge illustrated in Figure 3. This is the geometry of the bridge before it is subjected to gravity loads. The analyst must also specify the mechanical properties of the bridge elements, listed in Table 2. The program is created to accept all values in SI-units. The master script accepts these inputs from the analyst, and passes them on to a set of functions that creates the necessary vectors and matrices to describe the system.

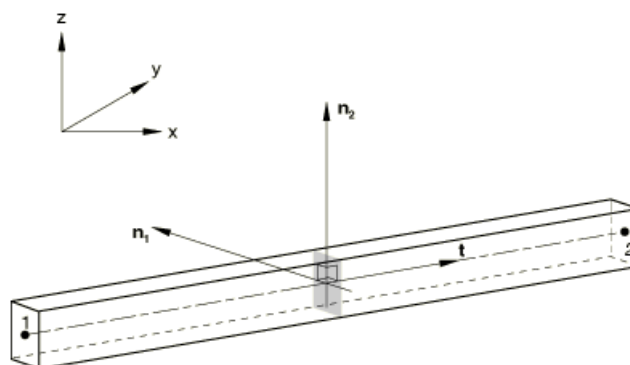


Figure 5: Element axis definition in Abaqus. Facsimile from Abaqus Keywords Reference Guide [1].

### **geometry.m**

The `geometry-` function reads all the geometric input from the master script. It uses this input to create all the nodes of the model and specifying the spacial coordinates of every node, as well as giving each node a unique number. The geometry created by the input parameters is the undeformed geometry of the bridge, before the gravity loads are applied.

### **elements.m**

This script arranges the nodes into elements. Every element is given a unique number. The elements are grouped into element sets for each of the different structural members in the model.

### **writefile.m**

After running `geometry.m` and `elements.m`, all the necessary data to create the Abaqus model is saved in the workspace. This script writes the input text-file by using the built-in function `fprintf` in MATLAB. The Abaqus input file processor requires a certain syntax of the input-file in order to perform a calculation. The matrices in the workspace are now written to the text-file in a specific order.

1. The spacial coordinates of all nodes in the model. Each node must also be given a unique number.
2. The elements and element type. Each element must be given a unique number, and it must be specified which nodes the elements contains. The elements are arranged in element sets that differ between the different structural members
3. The sections. Element sets are given mechanical properties and orientation.
4. Static step. Adding gravity loads on all members.

5. Frequency step. Eigenvalue extraction to calculate the natural frequencies and corresponding mode shapes.

Documentation for the requirements of the Abaqus input file can be found in Abaqus Keywords Reference guide [1].

### Single, double, and triple-girder principle

The model can be implemented with one, two, or three bridge deck girders. See Figure 6. For the single girder case the model disregards the external girders. The crossbeams is given negligible mass, and very high stiffness. The double girder bridge is created by disregarding the central girder. The girders is now connected to the hangers by large cross-beams. The position of the hangers on the crossbeams is controlled by the cable distance and the distance between the girders. The triple girder has the same structural principle as the double girder except that the central girder is included.

The analyst only needs to select the number of bridge girders in the analysis. The excess girders will be automatically disregarded, and the BC's will be updated the writefile-script.

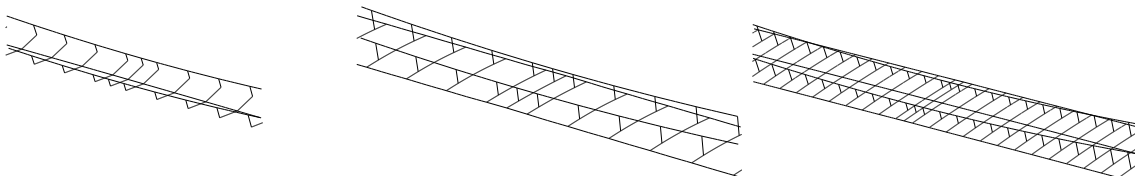


Figure 6: Bridge cross section for one, two and three girders

### Static tensioning step

It is important to add the gravity loads before doing the frequency step. This is because the geometrical stiffness is of particular importance for suspension bridges. This is especially for the cables, which rely very much on the geometrical stiffness. To account for the geometric non-linearities, and the large-deflection theory that occurs especially in the cables, the \*NLGEOM option in Abaqus is enabled.

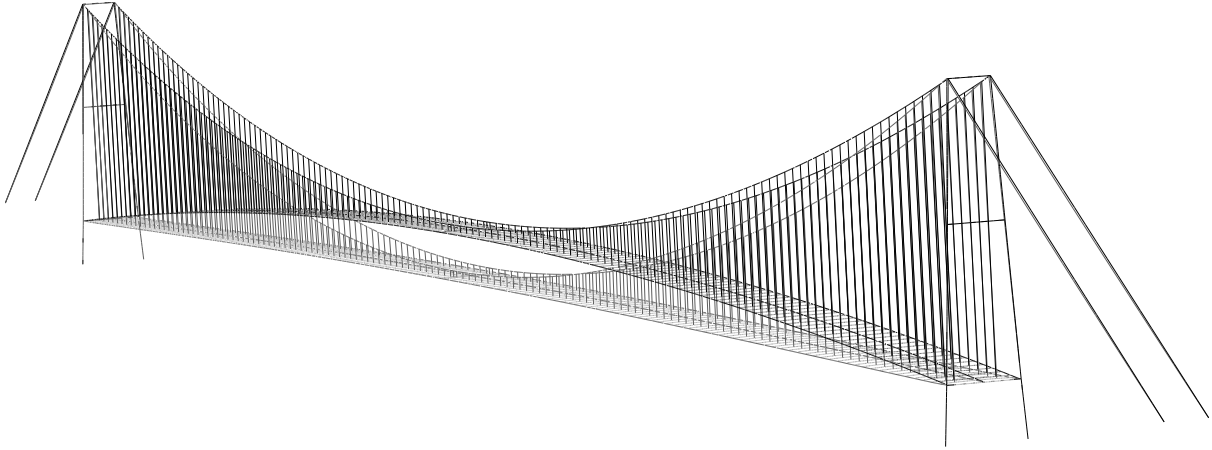


Figure 7: Geometry before and after the \*STATIC tensioning step. Example setup: Girder height mid span before tensioning = 45m. Girder height after tensioning = 8.5 m.

The parameters *Girder\_sag*, *h* and *sag* in Table 1 must be tested by the analyst. These three parameters describes the sag of the girder and cable before the tensioning step. Their size must be changed in order to obtain a reasonable equilibrium position for the bridge after gravity loads are applied. In other words: Since the geometry must be developed before gravity loads are applied, the analyst must try different settings for the sag to achieve the geometry desired after gravity is applied. In this thesis, a cable sag of  $\frac{L}{10}$  and a positive girder sag of 10-20 meters is desired, after gravity is applied.

### Elements and boundary conditions

This model uses two element types. The main- and side-girders, together with the cross-beams and the pylons are modelled as B32 beam elements. The main cables and the hangers are B31 beam elements. B31 is a beam element in space, with linear interpolation. It has one node in each end. B32 has quadratic interpolation, and hence also three nodes over the element length. The documentation can be found in the Abaqus Analysis User's Guide [1].

The cables are fixed in all translational and twisting degrees of freedom at the ends. Towers are also fixed in the same way at ground level. The main girder BC's is changed after the \*STATIC tensioning step described in Chapter 3.1. This is because the girder needs symmetric BC's in the tensioning procedure in order to deflect symmetric. This is an important condition to obtain symmetric mode shapes in the \*FREQUENCY- step. In the \*STATIC step the girders- ends has slide-bearings in the longitudinal direction, but they are fixed against vertical- and lateral- translation, as well as rotation about the longitudinal axis. The BC's are changed slightly after the \*STATIC load step: One of the girder-ends are fixed against longitudinal translation, in order to prevent the modes obtained in the \*FREQUENCY- step to include large oscillations in the longitudinal direction. This restraint will reflect the physical behaviour of a real suspension bridge, that is not able create large longitudinal deflections due to the abutments.

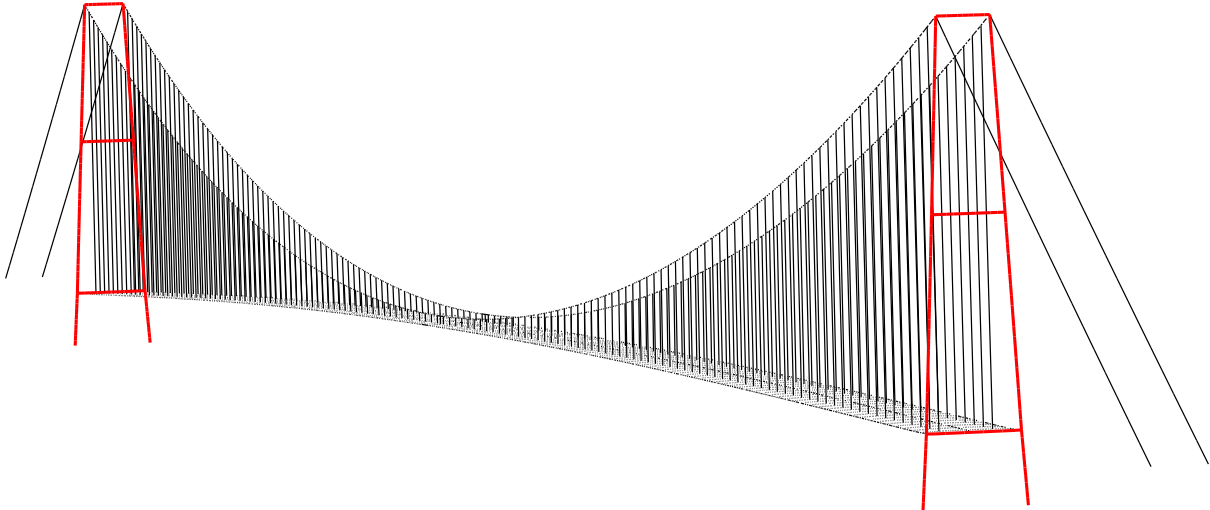


Figure 8: Setup 3 with pylons highlighted

## Pylons

The master script that generates the FE-model and analysis accepts input parameters for the pylon geometry, stiffness and material properties. As argued later in this paper, the code is not customized for decreasing area and stiffness over the height of the pylons. This decision is based on the results obtained in Chapter 5.4.

The pylons has three stiffening girders over the height. The top girder is located at the pylon top. The lowest stiffening girder is 10 cm beneath the support of the bridge girder. Note that these are not connected as the boundary conditions of the bridge girder prevents them from making contact.

The model has an option that accepts different distance between the cables mid-span and over the pylons, which will make the towers A-shaped. This is a much used solution for many suspension bridges world wide. This option may not be used unconditionally, as it induces large compression forces in the crossbeams in the mid-span. For wide setups this will cause buckling in the crossbeams.

## 3.2 MATLAB script for flutter analysis

The flutter procedure used to calculate the critical wind speeds in this thesis is created and provided by supervisor Ole Øiseth. It is a complex script that uses numerous MATLAB functions to iterate its way to the critical wind speed and oscillation frequency.

1. The calculation procedure begins with importing eigenvalues and eigenvectors from a datafile from an Abaqus analysis. This file must be specified according to the structure that is being analysed. From the data file the script also calculates the modal mass, stiffness and damping properties.
2. Next, curve fitting of the aerodynamic derivatives is performed. The type of AD must be specified together with the kind of curve-fitting that will be used.

3. The third step is where the stability iterations are made. The analyst must specify the modes that shall be included in the stability calculations. The script uses all the modal output from the Abaqus- data file, as well as the aerodynamic derivatives as input. The size of each velocity increment is specified, and the complex eigenvalue problem is solved for each velocity increment. The development of the real- and imaginary part of the complex eigenvalue problem, corresponding to the damping- and frequency of the structure described in Equation 71, is plotted as a function of wind velocity.

As both the frequency and wind velocity changes in each velocity iteration, the aerodynamic derivatives is re-calculated before inserted in the next iterations stability calculation, see Equation 69. The ADs that is used by the program follows the chosen curve-fitting as the wind velocity increases.

The velocity-iterations stops if the modal damping turns positive, causing positive feedback of the oscillations. If this occurs the stability limit of the structure is reached.

If the frequency iterations converges, the script will return the critical wind velocity, the critical frequency, and a plot of the real and imaginary parts of the complex eigenvalue problem. The results of the stability calculations are reported in Chapter 7.

---

## 4 Case study – Aerodynamic stability of a triple-girder suspension bridge

### 4.1 Introduction

Ever since the collapse of Tacoma Bridge in 1940, the flutter instability of suspension bridges has been carefully studied, and the challenges of verifying flutter stability of long suspension bridges remains today. The traditional way of preventing flutter is to increase the torsional frequencies of the bridge to prevent mode coupling from occurring.

However, as technology advances, allowing engineers to construct even longer bridges, the traditional design principles are no longer sufficient because of the decreasing torsional stiffness as the bridge length increases.

As a part of a research project together with PhD candidate Michael Styrk Andersen at the University of Southern Denmark, and supervisor Ole Øiseth, this thesis will investigate the possibility to create a flutter-free bridge section.

If the still-air torsional frequency is lower than the vertical frequency, the hypothesis is that the torsional mode will separate further away from the vertical mode as the wind speed increases. Thus, the frequency ratio  $\frac{f_r}{f_v} < 1$  being less than unity will lead to frequency separation, preventing flutter. Michael Styrk Andersen has designed a conceptual design of a triple-deck bridge girder with three configurations. In this preliminary stage of the project, the bridge sections analysed will be for the 2050 meters Halsafjord crossing on the Norwegian west coast. This fjord crossing is relevant for the future technology of flutter analysis, as the Norwegian Roads Administration are implementing the "Ferry Free Fest Foast"- project, replacing several ferry connections with bridge structures in a very wind-exposed environment.

This thesis will contribute to the triple-girder project by creating FE-models for the different setups, and perform flutter calculations to obtain the critical flutter wind velocities for the different setups.

### 4.2 The triple-girder concept

The principle of reducing the torsional frequencies below the shape-wise similar vertical frequencies is called the non-flutter principle [6]. The non-flutter principle has been addressed in the literature several times [5, 21], although only for double girder bridges. In 2009 Bartoli et al. published an article stating that the non-flutter principle will remove the necessity of a comprehensive aerodynamic optimisation, implying that the principle is not only innovative and futuristic, but may also be cost-effective [7]. The reduction of the torsional frequencies is a consequence of reduced torsional stiffness. This means that static divergence, see Chapter 2.5.1, might happen. Instead of reducing the stiffness, this project seeks to increase the mass moment of inertia by placing as much mass as possible outside the cables. This will contribute to the reduction of frequencies without necessarily reducing the stiffness to the point where static divergence might

occur [6].

### 4.3 Configurations for this thesis

In the feasibility study for a suspension bridge with a main span of 2050 meters crossing Halsafjorden, the triple girder is made out of one central closed-box section made out of steel and composite material. The two external decks are made from massive concrete. Analyses are made for three setups with varying distance between the central- and the external- girders. The design of these setups are made by Michael Styrk Andersen as part of his non-flutter project. Setup 1 acts like a reference setup due to its similarities to a single-box girder. Setup 2 is a medium-wide configuration and is supposed to have a frequency ratio  $f = \frac{f_r}{f_v} \approx 1$ . The third and widest setup is designed to have frequency ratio less than unity.

For the triple girder bridge, the longitudinal bridge cross sections are not directly connected to the hangers, as in conventional single girder suspension bridges. The hangers are fixed to transversal cross beams, that carries the stiffening girders. See Figure 4.

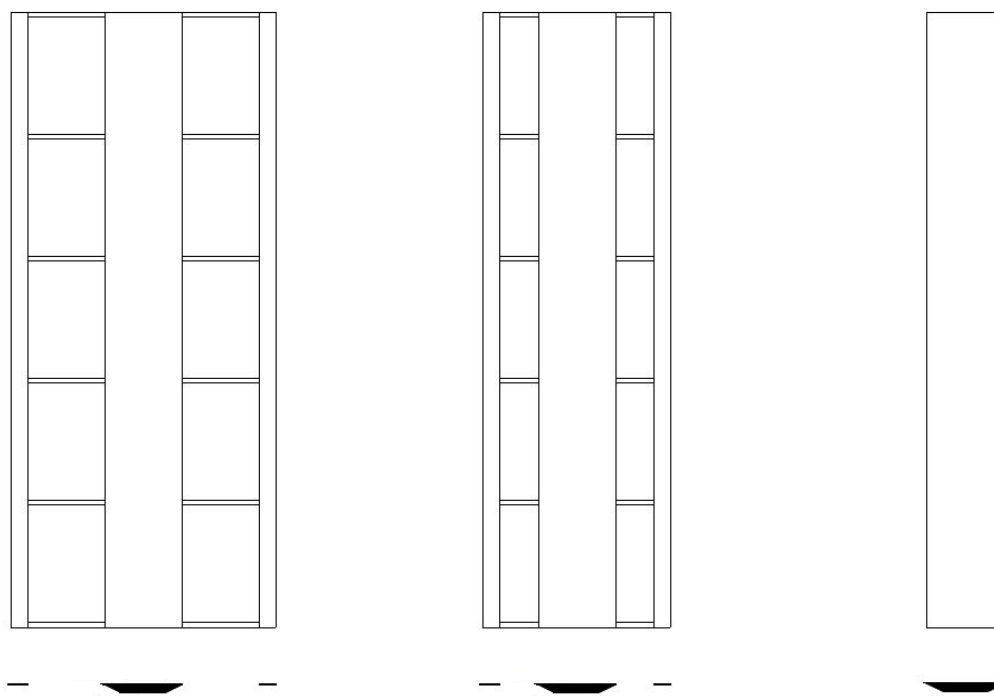


Figure 9: From right: Setup 1, Setup 2 and Setup 3.



Figure 10: Positioning of crossbeams and cables



Table 3: The different setups

Parameter	Setup 1	Setup 2	Setup 3
Distance between cables [m]	15	30	30
Slot opening [m]	0	8	16
C-C distance between central and external deck [m]	9.75	17.75	25.75
Length of cross beams [m]	23	39	55
Cross sectional area per cable [ $m^2$ ]	0.1767	0.1963	0.2044

## 5 Modal results

The main purpose of the finite element model is to find the zero-wind mode shapes and corresponding natural frequencies of the structure. This is essential in order to evaluate the in-wind characteristics, and to calculate the stability limit of the suspension bridge. The adjustable finite element model allows the analyst to extract this output for several setups and configurations. This is one of the main features of the model, and it makes the parameter study concerning the flutter limit easier. To easily describe the type of modes that are identified, a series of abbreviations are made.

Table 4: Abbreviations that describes the mode shapes

L	Lateral
V	Vertical
T	Torsional
A	Anti- symmetric
S	Symmetric
C	Cables

### 5.1 Verification of FE-model: The Hardanger Bridge replica
















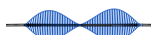

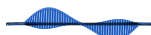

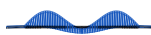






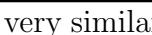

To verify that the FE-model is applicable for a variety of suspension bridge configurations, and that it gives reasonable results, it will be adapted to describe the Hardanger Bridge. The modal results is compared to the mode shapes and natural frequencies that is performed by The Norwegian Public Roads Association (NPRA), and used in the detailed design of the Hardanger Bridge.



Figure 11: Hardanger configuration of FE-Model

The model is created only by adjusting the optional parameters in the master script of the FE-model. The mechanical and geometrical properties is taken from the NPRA's calculation report [19]. The input parameters in the master script may be found in Appendix B.

Table 5: Modal output for the Hardanger Bridge replica compared to NRPA model.

Mode	NRPA	f[Hz]	Replica	f[Hz]	Error[%]	Side view	Top view
1	1LS	0.0501	1LS	0.0505	-0.88		
2	1LA	0.0980	1LA	0.1012	-3.22		
3	1VA	0.1104	1VA	0.1087	1.54		
4	1VS	0.1407	1VS	0.1405	0.13		
5	2LS	0.1690	2LS	0.1782	-5.49		
6	2VS	0.1972	2VS	0.1961	0.55		
7	2VA	0.2110	CS	0.2089	7.17		
8	CS	0.2250	2VA	0.2115	-0.23		
9	CA	0.2325	CA	0.2221	4.49		
10	CA	0.2336	CA	0.2265	3.04		
11	C+T	0.2445	C+T	0.2341	4.25		
15	1TS	0.3597			0.59		
16			1TS	0.3576	0.59		
17	1TS*	0.3921	1TS*	0.3653	6.83		

\*The second torsional symmetric mode, named 1TS\*, is very similar to 1TS. Both modes contain only one half sinusoidal wave over the bridge span. The difference of these two modes are the phase of the main-cable oscillations.

As can be seen in Table 5 the modes occur in the same order, except for the first torsional symmetric mode, that has changed place. The frequencies is considered to have acceptable error, considering that this is an approximate setup for the Hardanger Bridge made quickly from the master script of the FE-model. Assumptions on the pylon stiffness is the same as in Chapter 3.1.

Based on the results in Table 5 the FE-model is expected to give reasonable results for a wide range of suspension bridge setups. It is important to notice that the analyst is in any case responsible for controlling the geometrical and mechanical properties, as well as the assumptions and limitations of the model, before expecting good results. It is emphasized that the FE-element model is created for modal value extraction, and is not thoroughly tested for other types of analyses.

## 5.2 Estimated modal results

The main target for the calculations in this chapter is to investigate the parameters that affects the frequency ratio between the torsional and vertical eigenmodes,  $\gamma_\omega$ . The estimated eigenfrequencies and eigenmodes provided by supervisor Michael is used as a calibration of the model. His calculations is of a more approximate nature than the full scale Abaqus model. Even though, the approximations acts as a guide to the order of the vibration modes. This order, especially for the vertical and rotational degrees of freedom, is of high importance in the study of flutter-free bridges.

Table 6: Eigen-frequencies supplied by advisor Michael Styrk Andersen

Mode	Setup 1	f [Hz]	Setup 2	f [Hz]	Setup 3	f [Hz]
1	Lateral		Lateral		Lateral symmetric	0.0600
2	Lateral		VA1	0.0839	TA1	0.0772
3	Lateral		VS1	0.0960	VA1	0.0839
4	1VA	0.0837	TA1	0.0995	TS1	0.0881
5	1VS	0.0963	TS1	0.1150	VS1	0.0958
6	Lateral				TS2	0.1195
7	2VS	0.1300			VS2	0.1297
8	2VA				TA2	0.1445
9	1TA	0.1370			VA2	0.1573
10	Lateral				TS3	0.1821
11	1TS	0.1510				

As we can see in Table 7, the three setups has their respective eigenmodes in different orders, and therefore also different frequency ratios,  $\gamma_\omega = \frac{f_r}{f_v}$ . This ratio is an important parameter within flutter analysis, because the difference in vertical- and torsional frequency in many cases is decisive for the critical flutter wind velocity. As the wind velocity on a suspension-bridge increases, the torsional frequencies tends to decrease due to loss of torsional stiffness because of the aerodynamic forces. The vertical and horizontal vibration modes will not experience such a loss of stiffness. As the torsional stiffness decreases, the torsional frequency will decrease, and the torsional and vertical modes will at some point couple together. This coupling is a driving cause for the flutter phenomenon. But if the frequency ratio  $\gamma_\omega < 1$  for the zero-wind structural properties, the structure will experience mode separation, and flutter will therefore be prevented. This is the goal of the widest of the three setups below, Setup 3.

Table 7: Frequency ratio  $\gamma_\omega$  for the first pair of symmetric (S) and anti- symmetric (A) vertical and torsional modes, obtained from Table 6

Setup	$\gamma_{\omega,S}$	$\gamma_{\omega,A}$
1	1.42	>1.80
2	1.19	1.19
3	0.92	0.92

### 5.3 Vibration modes and natural frequencies for Setup 1-3

Table 8: Natural frequencies of the three setups. Error refers to the supplied results by Michael Styrk Andersen in table 6. The mode shapes are illustrated in appendix C

Mode	Setup 1	f[Hz]	Error[%]	Setup 2	f[Hz]	Error[%]	Setup 3	f[Hz]	Error[%]
1	1LTS	0.042		1LTS	0.048		1LTS	0.049	-22.0
2	1VA	0.086	3.3	1VA	0.087	3.1	1TA	0.076	-2.2
3	1LTA	0.092		1TA	0.095	-4.5	1VA	0.086	2.8
4	1VS	0.096	-0.3	1VS	0.097	0.8	1TS	0.089	0.7
5	1LTA*	0.117		1LTA	0.114		1VS	0.096	0.5
6	1TS	0.121	-19.6	1TS	0.117	1.8	1LTA	0.104	
7	2VS	0.130	0.3	2VS	0.131		2TS	0.115	-3.6
8	2LTS	0.158		2TS	0.151		2VS	0.130	0.6
9	2VA	0.158		2VA	0.159		2TA	0.139	-4.0
10	3LTS	0.177		2LTS	0.171		2LTS	0.153	
11				2TA	0.182		2VA	0.158	0.4
12							3TS	0.174	-4.6

\* 1LTA and 1LTA\* are vely similar mode shapes. The difference is that 1LTA\* has considerable more lateral deflections. The mode shapes are illustrated in Appendix C.

The calculated natural frequencies and corresponding modes for the three different setups can be seen in Table 8. Except the lateral modes of Setup 1, the modes appear in the same order as for the estimated data given in Table 6. This indicates that the FE-model gives satisfying results for the setups in the analysis.

It is evident that the combination of long spans and low stiffness of all three setups gives low torsional frequencies. The mode shapes in torsion have considerable lateral deflections for all the setups. This is not observed for the Hardanger Bridge replica or any other setup with span-length of 1000-1300 meters. The lateral contributions are however considered reasonable because of the super long span and low stiffness of the bridge deck.

Table 9: Frequency ratio  $\gamma_\omega$  for the first pair of symmetric (S) and anti-symmetric (A) vertical and torsional modes, obtained from Table 9

Setup	$\gamma_S$	$\gamma_A$
1	1.26	1.07
2	1.21	1.10
3	0.90	0.88

Note the highlighted cell. For Setup 1, the first torsional asymmetric mode also has considerable lateral contributions. The frequency ratio in this cell is thus the ratio between the first lateral torsional (1LTA) mode and the first vertical (1VA), and is not directly comparable to the corresponding ratio in Table 7.

## 5.4 Pylon analysis

Since the scope of this thesis is restricted to the flutter characteristics of a triple-girder bridge, the cable-girder system is most likely to be of biggest importance to the results. To consider whether or not it is necessary to implement solutions for adjustable geometry of the pylons, there has been performed eigenvalue-calculations to see how the pylons affect the eigenfrequencies. Three different tower- setups was calculated, to see how the difference in mass and stiffness affects the eigenfrequencies.

The pylons of the Hardanger Bridge has decreasing stiffness over the height. In the FE-model of the Hardanger Bridge that is created by the Norwegian Public Roads Administration, and used for the detailed design of the bridge, the pylon is modelled with 50 increments over the height of 131 m, to account for the decreasing stiffness [9]. To decide whether or not the decreasing pylon stiffness will affect the modal results for the suspension bridge, four calculations has been made.

1. Setup 3 without pylons. Cable- tops are free to move in x- direction, but fixed in y- and z- direction for the \*STATIC load step. For the \*FREQUENCY step, the cable tops are fixed in all translational DOF's. Analysis 1 is used as reference to the error in Table 10.
2. Setup 3, with pylons. Pylon geometry and stiffness is *ten times* the stiffest increment of the Hardanger pylons. Decreasing stiffness with height is not regarded.
3. Setup 3 with pylons. Pylon geometry and stiffness is the same as for the stiffest increment of the Hardanger pylons. Decreasing stiffness with height is not regarded. This is the standard tower configuration for Setup 3 in this thesis.

Table 10: Eigen-frequencies of different tower setups. Error refers to Analysis 1.

Mode	Analysis 1	f[Hz]	Analysis 2	f[Hz]	Error[%]	Analysis 3	f[Hz]	Error[%]
1	1LTS	0,050	1LTS	0,050	-0,3	1LTS	0,049	-1,0
2	1TA	0,076	1TA	0,076	0,1	1TA	0,076	-0,1
3	1VA	0,087	1VA	0,087	0,0	1VA	0,086	-0,3
4	1TS	0,093	1TS	0,092	-0,6	1TS	0,089	-4,5
5	1LTA	0,104	1VS	0,096	-8,1	1VS	0,096	-8,2
6	1VS	0,105	1LTA	0,104	0,1	1LTA	0,104	-0,2
7	2TS	0,123	2TS	0,121	-1,6	2TS	0,116	-5,5
8	2TA	0,139	2VS	0,130	-9,9	2VS	0,130	-9,5
9	2VS	0,144	2TA	0,139	0,2	2TA	0,139	-0,1
10	2LTS	0,153	2LTS	0,154	0,4	2LTS	0,153	0,0

As we can see in Table 10, the stiffness of the towers affects the modal output of the model. The modes mostly occurs in the same order in the models, except for the pairs 1LTA/1VS and 2TA/2VS that changes places due to reduced torsional stiffness in the analyses with towers included. See the dashed rows in the Table. Neither of these two mode pairs are likely to couple because of their low shape-wise similarity. Hence the

switching of modes when including the towers in the analysis is considered not to affect the probability of a multi-modal flutter instability of this setup.

Analysis 1 is the stiffest structure because the cables are fixed in all translational degrees of freedom in the top point. This replicates the model if the pylons were infinitely stiff.

Analysis 2 has very stiff towers with large cross sectional area. The geometry and stiffness parameters is *ten times* the magnitude of the stiffest(lowest) section of the Hardanger bridge pylons. Even though Setup 3 in this thesis is considerably longer than Hardanger Bridge, and has a wide girder, it is unrealistic that it would have such stiff towers over the entire length. Analysis 2 is therefore also considered as stiffer than what is reasonable.

Analysis 3 has the same properties as the lowest and stiffest increment of the Hardanger pylons. It is considered the most reasonable of the three pylon configurations. Even though decreasing stiffness is not considered, it seems as if the bridge's modal output is not very sensitive to changes in pylon stiffness. As seen in the highlighted cells of Table 10, the vertical symmetric modes changes with less than 10% when the towers are included. The error is though very similar for Analysis 2 and 3, indicating that the pylon stiffness does not change these frequencies considerably.

Most of the natural frequencies are not affected more than 1% when increasing the stiffness of the pylons by 1000%. The only vibration modes that stands out is the 1TS and 2TS that both experiences a increase in frequency of circa 4%. These results show that the natural frequencies are not very sensitive to changes in the pylon stiffness.

Since the scope of this thesis mainly focuses on the girder- and cable- influence within modal analysis, the pylon geometry and stiffness in Analysis 3 will be used herein. More research on the effects of pylon stiffness will not be further considered in this thesis. This may for instance be relevant when studying deflections and response of such long-span bridges.

## 5.5 Stiffness of crossbeams

In this Chapter it is investigated how the stiffness of the crossbeams affects the natural frequencies. The FE-model of Setup 1-3 is modified, and the modal results are reported in Table 11.

The increase of torsional frequencies is anticipated, as the torsional modes will lead to bending of the crossbeams. Making the beams very stiff, as in the FE-model, is however problematic in a civil-engineering point of view. This problem is not considered further, as this thesis focuses merely on the parameters that affects the natural frequencies and critical wind velocities.

For the mode pairs 1VS/1TS and 2VA/2TA of Setup 3, marked with dashed circles, the vertical and horizontal modes have switched places, making the frequency ratio above

Table 11: Eigenfrequencies Setup 1-3 with stiff crossbeams. The error refers to the normal configuration of Setup 1-3, as seen in Table 8

Mode	Setup 1	f[Hz]	Error[%]	Setup 2	f[Hz]	Error[%]	Setup 3	f[Hz]	Error[%]
1	1LTS	0.043	1.2	1LTS	0.053	9.7	1LTS	0,060	22.7
2	1VA	0.087	0.0	1VA	0.087	0.1	1TA	0.086	14.0
3	1VS	0.096	0.0	1VS	0.097	0.0	1VA	0.087	0.4
4	1LTA	0.100	8.6	1TA	0.104	9.3	1VS	0.097	0.2
5	1TS	0.128	5.2	1TS	0.124	6.1	1TS	0.104	17.0
6	1LTA*	0.128	9.7	2VS	0.131	0.1	2TS	0.130	12.6
7	2VS	0.130	0.0	2VA	0.159	0.1	2VS	0.131	0.4
8	2VA	0.158	0.0	2TS	0.160	5.9	2VA	0.159	0.6
9	2TS	0.169	6.7	1LA+C	0.169		2TA	0.163	17,6
10	1LA+C	0.194		C	0.193		C		
11	1LS+C	0.194		2TA	0.198	8.9	C		

\* 1LTA and 1LTA are vely similar mode shapes. The difference is that 1LTA\* has considerable more lateral deflections. The mode shapes are illustrated in Appendix C.

unity.

$$\gamma_{1S} = \frac{1TS}{1VS} = \frac{0,104}{0,097} = 1.08 \quad (74)$$

$$\gamma_{2A} = \frac{2TA}{2VA} = \frac{0,163}{0,159} = 1.03 \quad (75)$$

This is certainly an interesting result, since Setup 3 cannot be considered flutter-free with stiff crossbeams. The effect of such structural members ability to change the global behaviour of the structure must be considered in any detailed design. This result will affect the aerodynamic stability, that is analysed in Chapter 7.8.



---

## 6 Aerodynamic derivatives

One of the challenges of calculating the flutter limit in a conceptual phase of a project like this is the lack of aerodynamic derivatives. As there are no ADs available for similar sections, three different approaches has been conducted in the flutter analysis. The aerodynamic derivatives for two bridges that has similar cross-sections has been used in the analyses. In addition Theodorsen's ADs for thin aerofoils has been used.

### 6.1 Assumptions

#### Reduced velocity

As mentioned in Chapter 2.3, the ADs are functions of the reduced velocity which is given as  $\tilde{V} = \frac{V}{B\omega}$  or as  $\tilde{V} = \frac{V}{Bf}$  where  $V$  is the wind velocity,  $B$  is the width of the bridge section, and  $\omega$  and  $f$  is the oscillating frequency of the structure in radians and degrees respectively. There are many different ways to define  $B$  when performing a wind tunnel test. It is important that the analyst is consequent with the definition of  $B$ . When using experimental data for aerodynamic derivatives, one must use the same definition of  $B$  when formulating the Scanlan flutter equations in Equation 20, as was used to normalize the ADs during the wind tunnel tests. In this thesis Theodorsen's analytical ADs has been used [20], as well as experimental ADs from Hardanger Bridge and Messina Bridge. All three uses the total width of the girder as  $B$ . For Messina this includes the gaps between the central and external girder.

The final value of the reduced velocity will depend on the calculated critical wind velocity, the oscillation frequency of the structure as it reaches flutter, and finally the width  $B$ . When performing a wind tunnel test the analyst must predict the order of magnitude of these three parameters so the test series for the ADs includes data for sufficiently high reduced velocities.

#### Curve fitting

The data series of aerodynamic derivatives extracted from the wind-tunnel testing is a discrete series of data-points. In order to utilize them in stability-calculations one must perform curve-fitting to create continuous functions that may describe them. There are two methods that is commonly applied in the curve fitting of aerodynamic derivatives.

1. Polynomial curve fitting where the data points are used to perform a regression where a polynomial of a certain order is created to estimate the measured data.
2. Rational functions that describes the measured data within a reasonable range.

## Extrapolation

If the range of the reduced velocities is too narrow to include any instability, one must extrapolate the ADs. This may introduce major error, and greatly affect the calculation of the self-excited forces. This is because the polynomials are often second order or more, making them highly unfitted for extrapolation beyond the experimental data. As illustrated in Figure 12, the different polynomials will achieve very different values outside the range of the measured data points, making extrapolation of these functions highly uncertain.

To perform flutter analyses outside the domain of the experimental data of the ADs will in this thesis be considered purely speculative. The results obtained will then only be a matter of choice of interpolation, and not a matter of physics. This will be an issue in the setups in this thesis because of the low frequencies that leads to high reduced velocities.

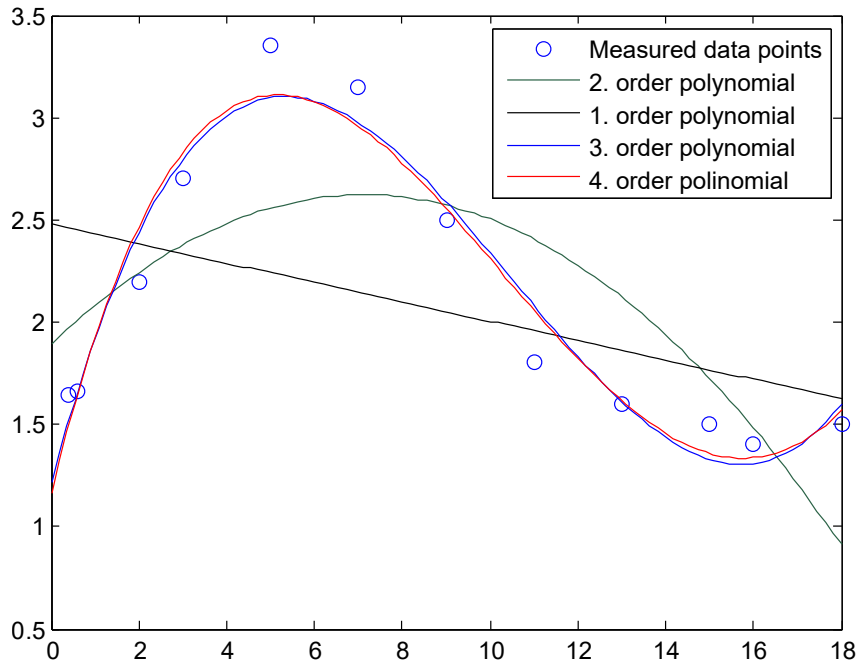


Figure 12: Different curve fittings for  $H_4^*$  of the Messina Bridge.

## 6.2 The role of each aerodynamic derivative

The aerodynamic derivatives are used to calculate the self-excited forces from the interaction between the oscillating structure and the wind flow. The different derivatives are connected to the self-excited forces as described in Equation 20. Rewriting this equation to describe the forces in drag, lift, and moment, we obtain

$$\begin{bmatrix} F_D \\ F_L \\ F_M \end{bmatrix} = \frac{\rho B^2}{2} \omega \begin{bmatrix} P_1^* & P_5^* & BP_2^* \\ H_5^* & H_1^* & BH_2^* \\ BA_5^* & BA_1^* & B^2A_2^* \end{bmatrix} \begin{bmatrix} \dot{r}_D \\ \dot{r}_L \\ \dot{r}_\theta \end{bmatrix} + \frac{\rho B^2}{2} \omega^2 \begin{bmatrix} P_4^* & P_6^* & BP_3^* \\ H_6^* & H_4^* & BH_3^* \\ BA_6^* & BA_4^* & B^2A_3^* \end{bmatrix} \begin{bmatrix} r_D \\ r_L \\ r_\theta \end{bmatrix} \quad (76)$$

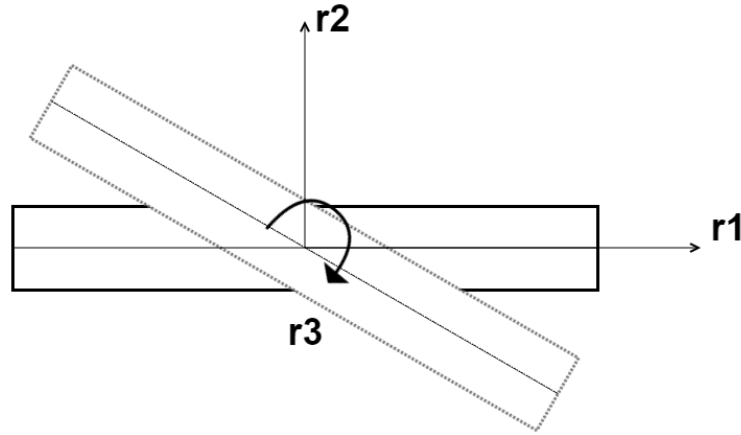


Figure 13: 3-DOF convention corresponding to the aerodynamic derivatives.  $r_D = r_1$ ,  $r_L = r_2$ ,  $r_\theta = r_3$

From Equation 76 it is easy to interpret the physical meaning of the different terms. For instance the term  $BH_2^*$  describes the connection between the lifting force  $L$  and the rate of rotation  $\dot{r}_\theta$ . The  $BH_3^*$ -term is the connection between the lifting force  $L$  and the rotation of the girder,  $r_\theta$ .

In aerodynamic stability analysis there are some AD-terms that will affect the different instability phenomena more than others. It is the cross-terms in the in-wind stiffness and damping matrices that provides the coupling between horizontal, vertical and torsional modes. Besides the frequency ratio between the shape-wise similar modes susceptible for flutter, this is the most crucial parameter for flutter to occur. In the case of classical flutter, the coupling is controlled mainly by  $H_2^*$  and  $H_3^*$  [14]. The torsional damping is described by the term  $A_2^*$ , and is the controlling term for pure torsional flutter [14, 16].

In Figure 17 and 18 the three different AD-series are plotted against each other. The difference in the ADs will be used to explain the different stability limits that are found in chapters 7.2 to 7.7.

### 6.3 Accuracy of aerodynamic derivatives

The traditional method for extracting aerodynamic derivatives in the wind tunnel is the *free-vibration method*. It involves a model section mounted on springs. As the section is subject to increasing wind speeds, the displacements and oscillations are measured, and processed in order to describe the self-excited forces. An other method for AD-extraction that is subject to much contemporary research is the *forced vibration method*. In this method the bridge model section is fixed in an apparatus that moves it in vertical, lateral and horizontal motions while at the same time measuring the forces required to do so. The self-excited forces are extracted by subtracting the zero-wind forces from the in-wind forces for each configuration of wind speed and oscillation frequency.

In traditional bridge design it has usually been sufficient with 2DOF stability analysis, eliminating the lateral DOF  $r_1$  in Figure 13. This reduces the number of non-zero ADs

from 18 to 8, as  $P_{1-6}^*$ ,  $H_{5,6}^*$ , and  $A_{5,6}^*$  in Equation 76 are all equal to zero. The technical aspect of the measurements are also severely complicated by the inclusion of lateral ADs. The quality of the lateral ADs are in many cases highly uncertain due to the difficulties encountered in the extraction process.

The aerodynamic derivatives are in most cases within bridge aerodynamics empirical, and they may be very sensitive to small changes in geometry of the bridge model section. This represents a major weakness in stability calculations performed in this thesis, as they are based on ADs from different bridge sections.

## 6.4 ADs of the setups in this thesis

### Theodorsen

The Theodorsen ADs are calculated as a part of the flutter routine that is provided by supervisor Ole Øiseth. The ADs are calculated directly from Equations 22, 23 and 24. These eight aerodynamic derivatives,  $A_i^*$  and  $H_i^*$ ,  $i = 1 - 4$  do not include any horizontal contributions. It is emphasised that Theodorsen's ADs are theoretical expressions yielding a flat plate, and is derived by using non-stationary potential flow theory combined with a series of assumptions. Therefore they are not able to correctly describe the self-excited forces for the sections analysed in this thesis. Nevertheless, they are used in the analyses as a reference against the empirical ADs that have sources of errors that are more difficult to control

### Hardanger Bridge

The Hardanger Bridge is a single girder suspension bridge crossing the Hardanger fjord on the Norwegian west coast. The bridge has a closed box girder with optimized aerodynamic behaviour. The main span of the bridge is 1310 meters and the girder is 18.3 meters wide. The bridge is one of the most slender cable bridge structures in the world, making it suspicious for large aerodynamic oscillations and instabilities. The Hardanger Bridge ADs are calculated by second order polynomials that are curve-fitted to experimental data implemented in the flutter procedure.

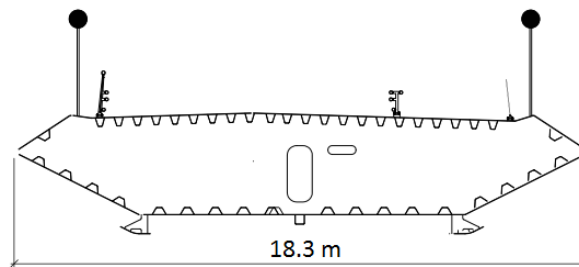


Figure 14: Geometry of the Hardanger bridge. Geometry taken from [19].

## Messina Bridge

Messina Strait Bridge is a suspension bridge with a main span of 3300 meters. The bridge was supposed to provide a fixed link between the Italian main-land and the east coast of Sicily. The construction of the bridge was scheduled to begin in 2009, but the project was stopped due to economic circumstances and political disagreement. The huge structure was designed with eight traffic lanes, and a double track railway. See Figure 15.

The aerodynamic derivatives of the Messina Bridge has been used in this thesis as it is the only triple-girder suspension bridge with ADs available in the literature. The ADs are extracted from Alan Larsen's paper "Horizontal aerodynamic derivatives in bridge flutter analysis" [14].

Even though both Messina Bridge and Setup 2 and 3 are triple girder bridges, the structures are very different. While the setups for the Halsafjord- crossing are light structures that supports two traffic lanes, Messina Bridge is a very heavy and stiff structure. The external decks of Setup 2 and 3 are 3.5 meters wide, 0.35 meters high concrete plates, while the external decks of Messina Bridge is 12.75 meters wide closed box sections. The difference in the external decks are evident when comparing Figure 15 and 16. Another difference between the two is that Messina has its cables outside the external decks. Setup 2 has the cables over the cross beams, approximately 12.5 meters from the outer edge of the external decks. Messina has large wind-screens that will drastically increase drag-forces. The differences in the geometries are illustrated in Figures 15 and 16.

The Messina ADs are likely to induce to large self-excited forces on Setup 2 and 3 because of its large dimensions compared to the slender and lean design of Setup 2 and 3.

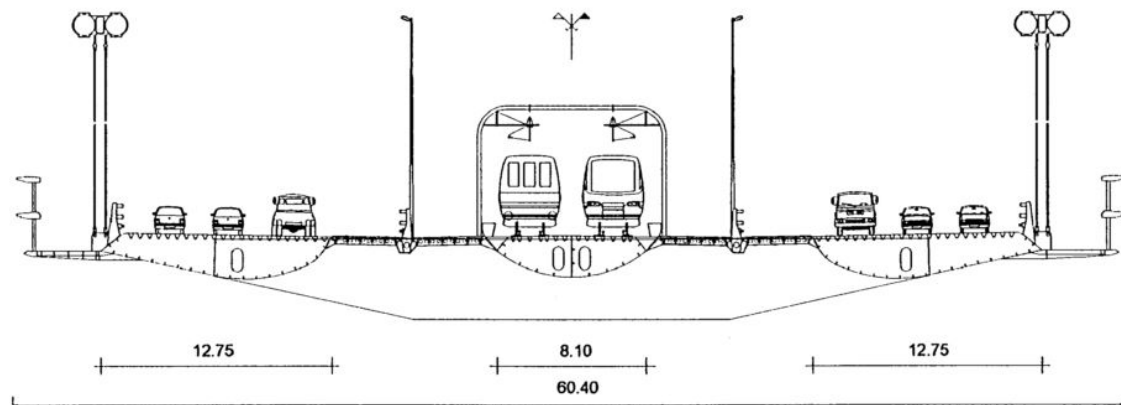


Figure 15: Geometry of Messina tripple- girder. Facsimile from [15].

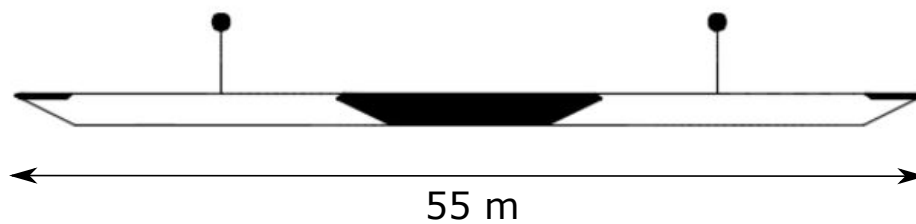


Figure 16: Geometry of Setup 3. The external girders are very narrow, only 3.5 m wide.

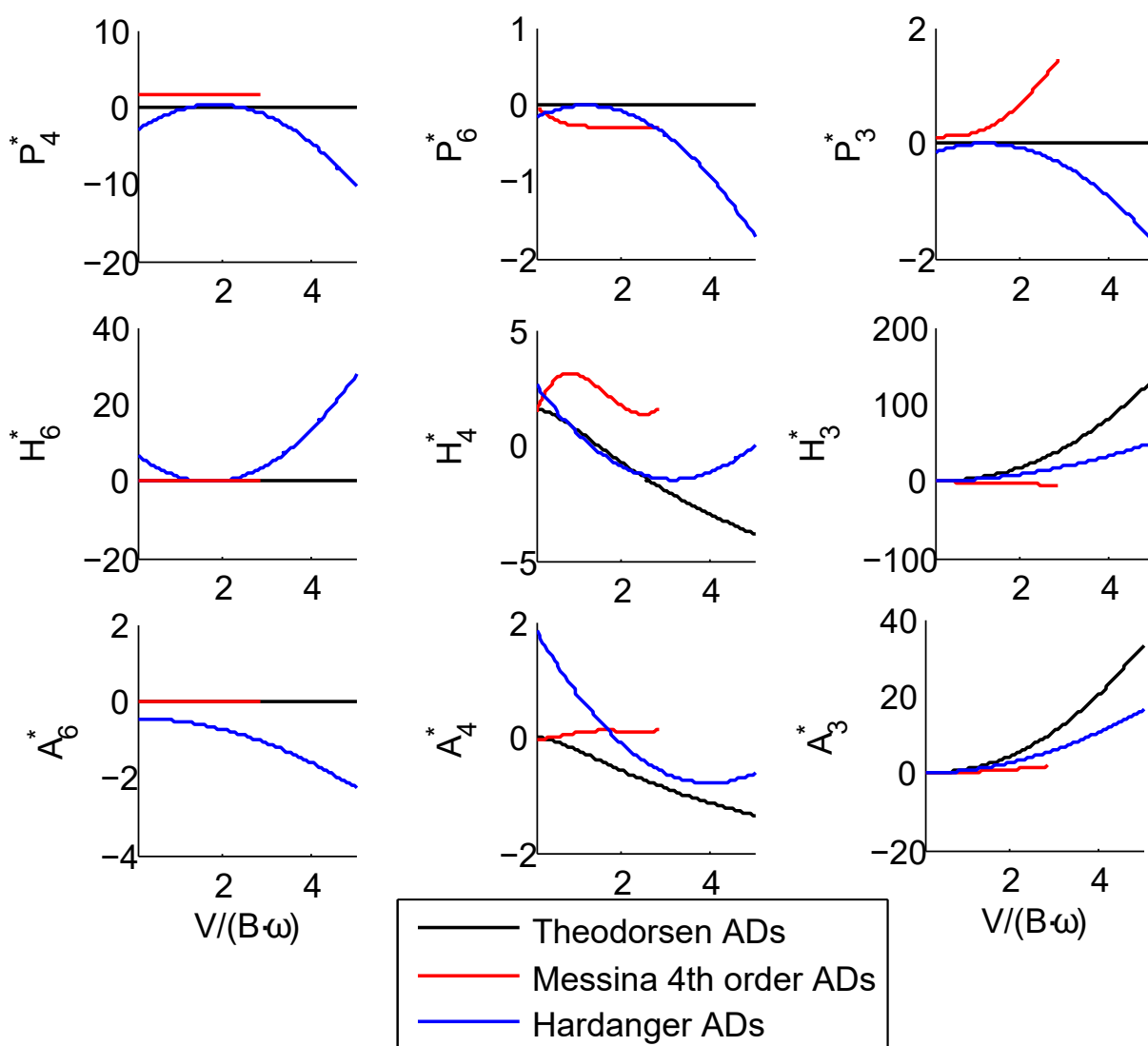


Figure 17: ADs corresponding to aerodynamic stiffness. Normalized with frequencies in radians.

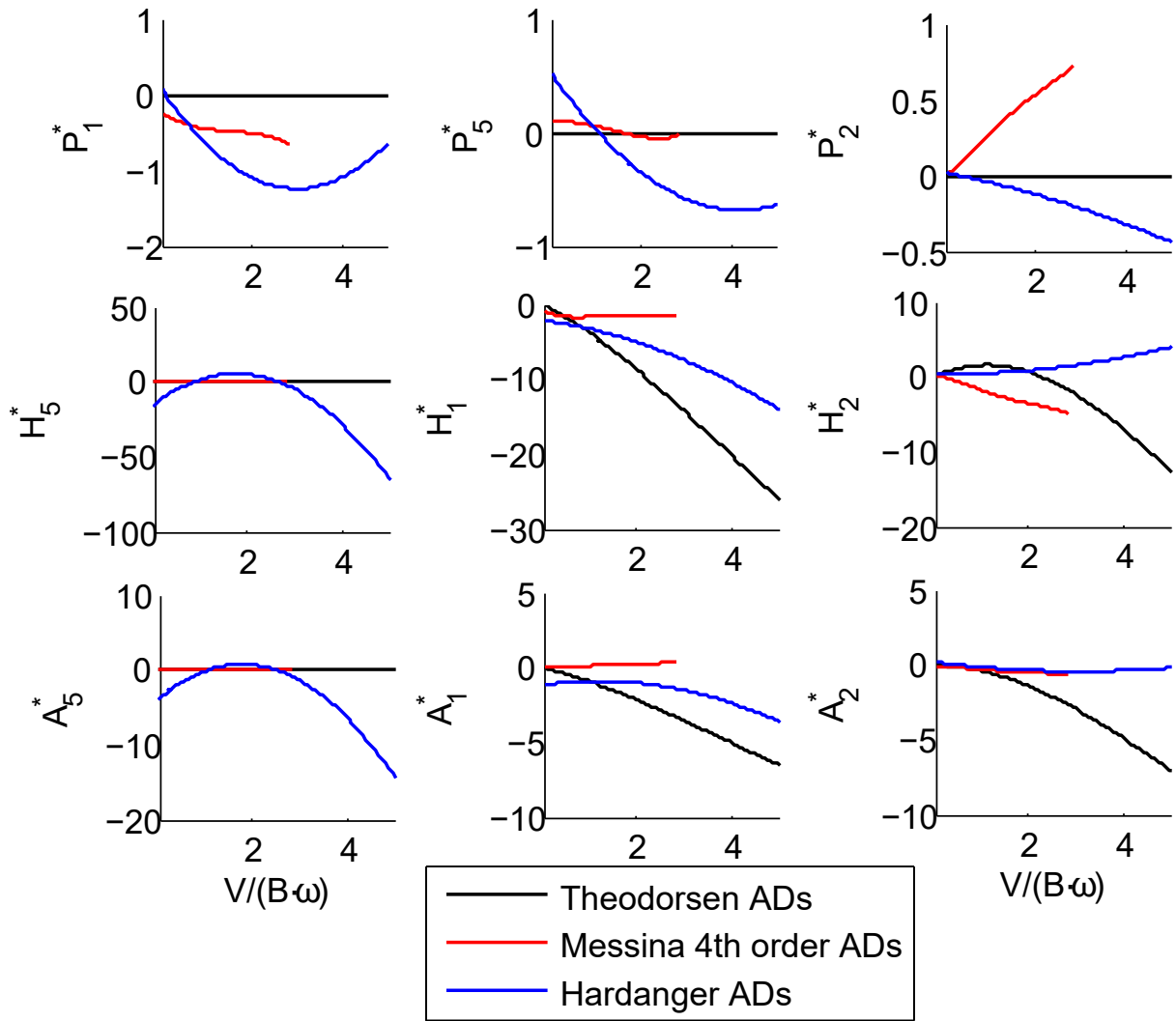


Figure 18: ADs corresponding to aerodynamic damping. Normalized with frequencies in radians.

## 7 The critical wind velocity

Since the aerodynamic derivatives for Setup 1-3 is not available during the writing of this thesis, there has been made certain assumptions in order to evaluate the aerodynamic performance of the different setups. For Setup 1 the Hardanger derivatives is used. This is a reasonable approximation considering that Setup 1 has similar geometric shape as the Hardanger bridge. For Setup 2 and 3 it is first assumed that the ADs for Messina bridge can be used. The reason for choosing Messina is that this is the only triple girder suspension bridge with ADs available in the literature [14]. Due to the low torsional frequency of this setup and high expected wind velocities, the reduced wind velocity  $V_{red} = \frac{V}{f \cdot B}$  will become high and cause numerical problems. As the Messina derivatives has not been implemented with complete success, Setup 2 and 3 will also be analysed with the Theodorsen and Hardanger ADs.

In the search for the critical wind velocity of bridges, we are looking for the wind velocity where the damping turns negative, i.e. when forces from wind flow add more energy to the oscillations than the structure and wind can dissipate. There are many uncertainties in the flutter calculations for the triple girder bridge. The author's experience suggests that it is the quality and validity of the aerodynamic derivatives that is most crucial for the results.

### 7.1 Flutter analysis of the Hardanger Bridge replica

In order to verify the flutter procedure for the various setups in this project, it is performed a flutter analysis of the Hardanger Bridge replica described in Chapter 5.1. The calculation is conducted with approximated ADs for the Hardanger bridge, obtained in [11], as well as Theodorsen ADs.

Table 12 shows the critical wind velocity and frequency for different combinations of modes. It is clear that the flutter calculations using Theodorsen ADs underestimates the critical wind speeds by 10-15%. This is because of differences in the aerodynamic derivatives. Theodorsen ADs does not include any self-excited forces in the along-wind direction. This will cause an underestimation of the damping in the system, as the horizontal modes will introduce damping to the system. The flutter mechanism identified involves four vibration modes, 1VS, 2VS, 1TS and 1TS\*. See Appendix C for illustrations. As presented in Table 12 and Figure 21 and 22, the 1TS is the driving mechanism of the flutter instability. However it is clear from Table 12 that convergence of the stability limit requires both 1TS and 1TS\*. This is because of the high shape-wise similarity between 1TS and 1TS\* that is illustrated in Figure 19.

The stability limit of the Hardanger bridge replica is reasonable compared to similar stability calculations in the literature. For instance, Øiseth, Rønnquist, and Sigbjørnsson [10], obtained the results in Table 13 for quasi-static and Hardanger ADs, respectively. Note that the Theodorsen and the quasi-static ADs are not identical, ref. Equation 21 and Equation 22. For instance, the quasi-static ADs do not introduce any torsional damping to the system, as  $A_2^* = 0$ . This may explain why the stability limit for these



Table 12: Critical wind velocity for Hardanger replica. Theodorsen ADs, Hardanger ADs with  $P_{1-6}^* = 0$ ,  $H_{5,6}^* = 0$ , and  $A_{5,6}^* = 0$ , and the full set of Hardanger ADs is reported.

Theodorsen ADs	Modes	Mode ID	$V_{cr}$ [m/s]	$f_{cr}$ [Hz]	
	1 to 20		67.78	0.263	
	4 6 16 17	1VS+2VS+1TS+1TS*	67.34	0.263	
	6 16 17	2VS+1TS+1TS*	74.41	0.242	
	4 6 17	1VS+2VS+1TS*	80.28	0.286	
	4 16 17	1VS+1TS+1TS*	81.34	0.195	
	4 6 16	1VS+2VS+1TS	83.66	0.133	
	6 17	2VS+1TS*	91.34	0.261	
	6 16	2VS+1TS	97.28	0.267	
	4 16	1VS+1TS	109	0.228	
Hardanger ADs	Modes	Mode ID	$V_{cr}$ [m/s]	$f_{cr}$ [Hz]	$V_{red}$
$P_{1-6}^* = 0$	1 to 20		77.78	0.279	2.42
$H_{5,6}^* = 0$	4 6 16 17	1VS+2VS+1TS+1TS*	78.09	0.277	2.45
$A_{5,6}^* = 0$					
Hardanger ADs	Modes	Mode ID	$V_{cr}$ [m/s]	$f_{cr}$ [Hz]	$V_{red}$
	1 to 20		77.53	0.278	2.41
	4 6 16 17	1VS+2VS+1TS+1TS*	78.09	0.277	2.45
	6 16 17	2VS+1TS+1TS*	83.9	0.262	2.78
	4 6 17	1VS+2VS+1TS*	93.28	0.296	2.74
	4 16 17	1VS+1TS+1TS*	92.4	0.223	3.44
	4 6 16	1VS+2VS+1TS	95.41	0.307	2.70
	6 17	2VS+1TS*	101.91	0.281	3.15
	6 16	2VS+1TS	107.84	0.291	3.22
	4 16	1VS+1TS	118.22	0.275	3.74

\* See Table 5

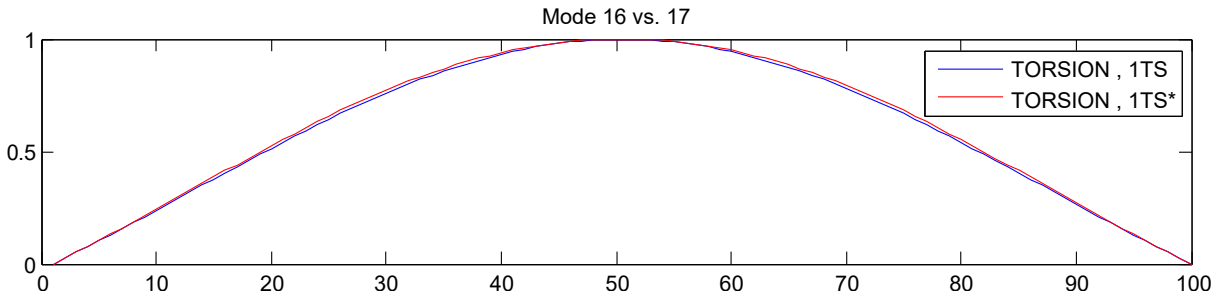


Figure 19: Shapewise similarity of 1TS and 1TS\* in torsion.  $\psi_{16,17} = 0.9999$

derivatives is considerable lower than for Theodorsen and Hardanger.

If we consider the mode combination 1VS+2VS+1TS+1TS\* for the three cases in Table 12 we see that the stability limit is the same for both cases of Hardanger ADs. This is because these modes don't have any lateral components, making the assumption of  $P_{1-6}^* = 0$ ,  $H_{5,6}^* = 0$ , and  $A_{5,6}^* = 0$  insignificant. Since the Hardanger replica model has lateral modes amongst its first 20 modes, the stability limit when including all the first

20 modes is affected slightly by this assumption. The Theodorsen analysis gives a lower stability limit for the same mode combination, than the reduced Hardanger analysis. This indicates that it is not only the damping in lateral DOF that causes the difference in stability limit, but also the self-excited forces created by  $H_{1-4}^*$  and  $A_{1-4}^*$ .

Table 13: Results from Øiseth, Rønnquist, and Sigbjørnsson, 2010 [10]

Quasi static ADs	Modes	Mode ID	$V_{cr}$ [m/s]	$f_{cr}$ [Hz]	
	4 6 13	1VS+2VS+1TS	44	0.329	
	4 13	1VS+1TS	59	0.307	
Hardanger ADs	Modes	Mode ID	$V_{cr}$ [m/s]	$f_{cr}$ [Hz]	$V_{red}$
	1 to 24		79	0.259	2.7
	4 6 13	1VS+2VS+1TS	78	0.259	2.6

For the Hardanger AD calculations, the results are more similar. In the results from Øiseth, Rønnquist, and Sigbjørnsson, 2010 [10], the first torsional symmetric mode shape is unique and is also the only torsional mode that is critical. In the Hardanger replica model, there are two very similar torsional modes that contributes significantly to the stability limit, 1TS and 1TS\*. See Figure 22 and Table 5. This difference may be caused by

- Simplifications made in the FE-model referred to in [10] that gives clean mode shapes in torsion. For instance neglecting the cables.
- An error in the FE-model for Hardanger replica that pollutes the lowest torsional mode shapes.

Usually it is the first shape-wise similar pair of vertical and torsional mode shapes that gives the lowest critical wind speed. As can be seen in Table 12, this is not the case for the Hardanger Bridge. The lowest critical velocity is found for a combination of the two lowest symmetric vertical and torsional modes.

$$\psi_{4,16} = \frac{\int_L \phi_4 \phi_{16} dx}{\int \phi_4^2 dx} \frac{\int \phi_{16} \phi_4 dx}{\int \phi_{16}^2 dx} = 0.4565 \quad \psi_{6,17} = \frac{\int_L \phi_6 \phi_{17} dx}{\int \phi_6^2 dx} \frac{\int \phi_{17} \phi_6 dx}{\int \phi_{17}^2 dx} = 0.5410 \quad (77)$$

$$\psi_{4,17} = 0.4496 \quad \psi_{6,16} = 0.5335$$

As we can see from the shapewise similarities in Equation 77, mode 6 and 17 has the highest shapewise similarity of the critical mode shapes. As seen in Figure 19 the two first torsional mode shapes, number 16 and 17 is almost identical for the bridge girder. The main difference in these two modes are the cable oscillations. In mode 16, the cables oscillate in phase with the girder rotation. For mode 17, the cables are out of phase. The reason why the  $V_{cr}$  has not fully converged for the the mode combination 4, 6, 16, and 17 is likely because of shape-wise similarity between several of the other first 20 modes.

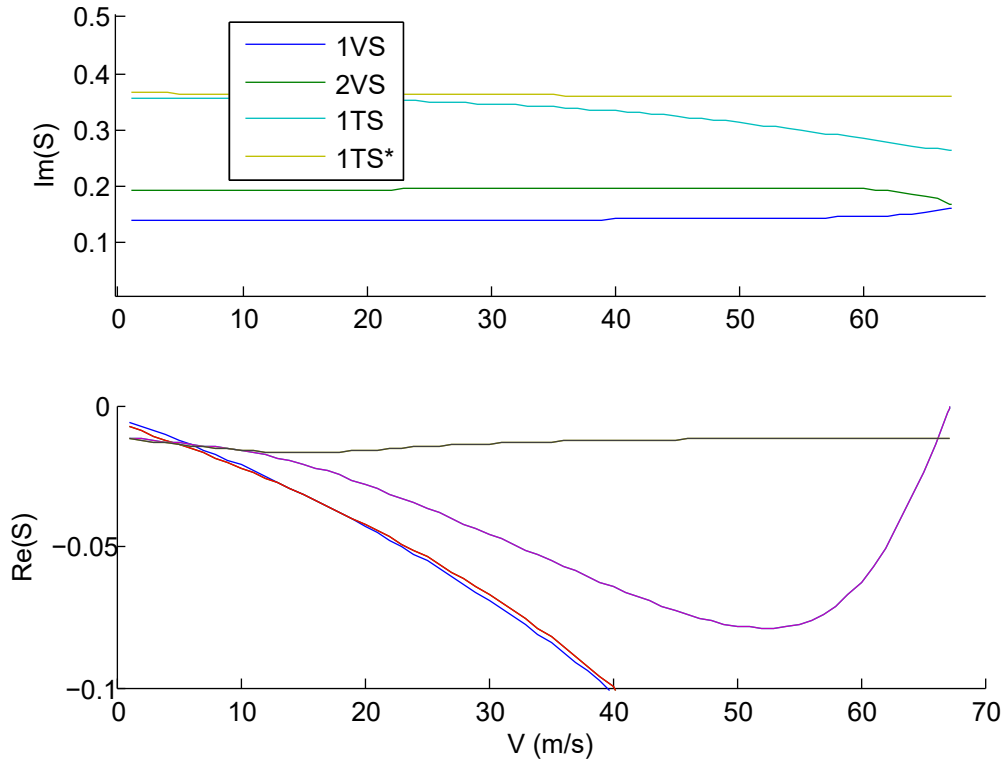


Figure 20: Solution of the complex eigenvalue problem for Hardanger replica using Theodorsen ADs. It is clearly seen that 1TS is the mode that drives the system to flutter.

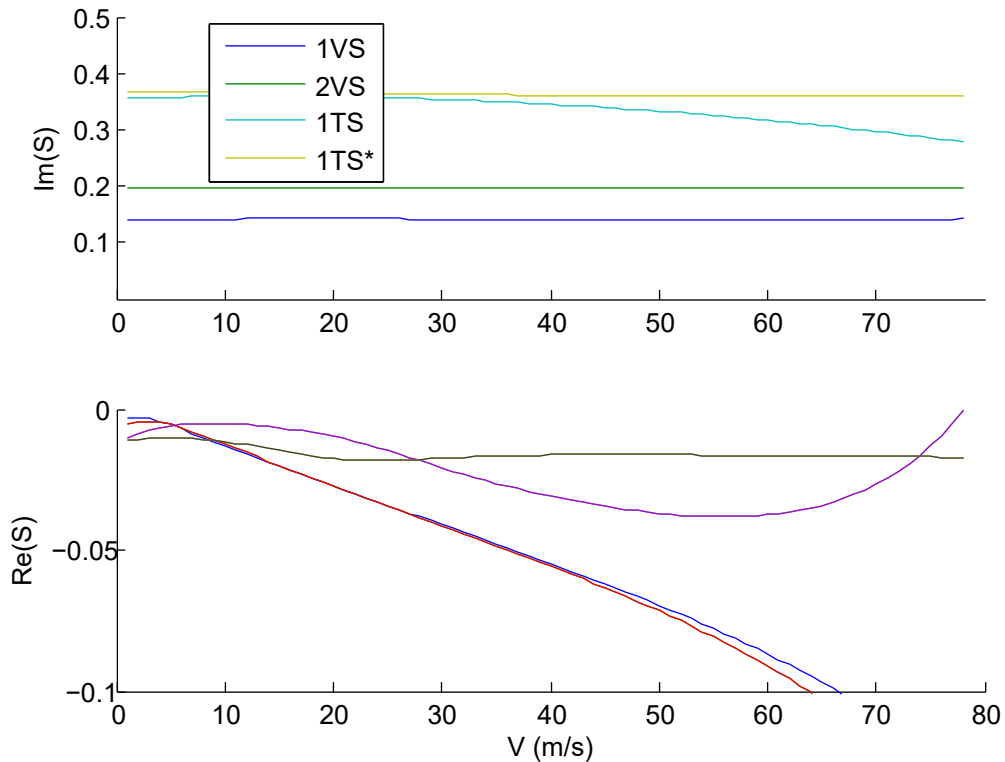


Figure 21: Solution of the complex eigenvalue problem for Hardanger replica using Hardanger ADs

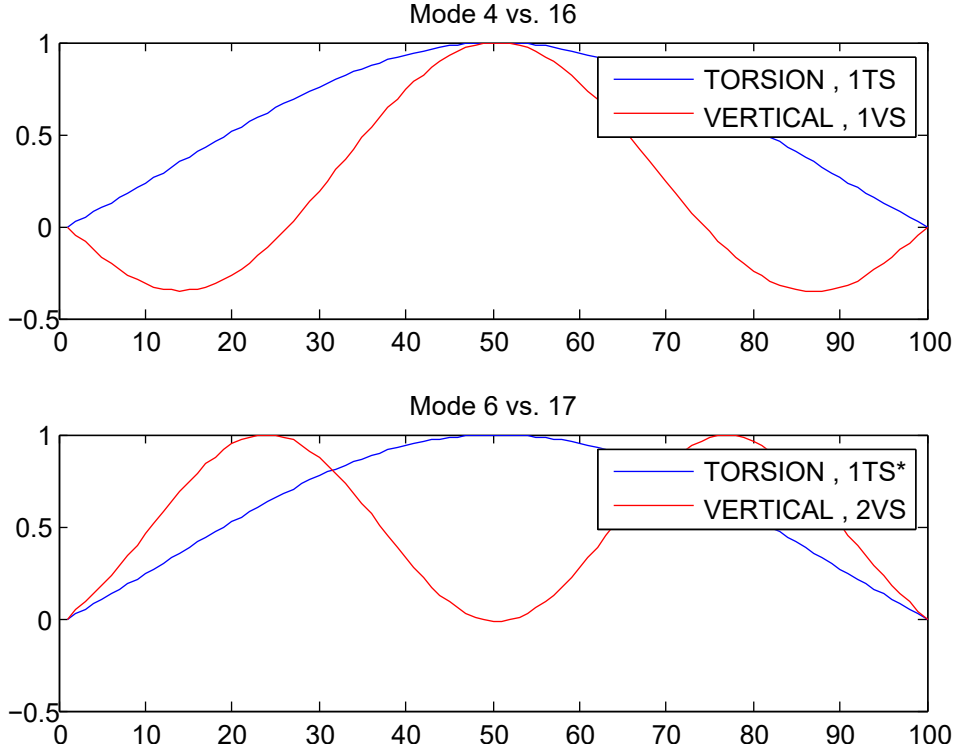


Figure 22: Critical mode shapes for the Hardanger Bridge

## 7.2 Setup 1

As expected, the stability limit for Setup 1 is very low. With a main span length of 2050 meters and a girder width of 16 meters the bridge is extremely slender, making it highly vulnerable for aerodynamic instabilities. An overview of some well-known suspension bridges are given in Table 1 in Øiseth, Rønnquist, Sigbjørnsson [10]. The Table is reproduced here in Table 14, illustrating the slenderness of Setup 1.

Table 14: Width and lengths of some well-known bridges. The Table is a modified reproduction from [10]

Bridge Name	Main span [m]	Width[m]	Country
Akashi-Kaiko Bridge	1991	35.5	Japan
Xihoumen Bridge	1650	36	China
Great Belt Bridge	1624	31	Denmark
Runyang Bridge	1490	39.2	China
Humber Bridge	1410	28.5	UK
Jiangyin Suspension Bridge	1385	-	China
Tsing Ma Bridge	1377	41	China
Hardanger Bridge	1310	18.3	Norway
Setup 1	2050	16	-

As the bridge cross section is an aerodynamic optimized hollow box section similar to the Hardanger Bridge, the Hardanger ADs are assumed to give reasonable self-excited forces for Setup 1. For this study, the difference in mass, and torsional stiffness of the two bridges is neglected. These are factors that will affect the Hardanger ADs ability to

reproduce realistic ADs for Setup 1, but this is not considered further, as the aerodynamic design of Setup 1-3 is still in a conceptual phase.

Table 15: Critical wind velocity for Setup 1 using different types of ADs

Theodorsen ADs	Modes	Mode ID	$V_{cr}$ [m/s]	$f_{cr}$ [Hz]	
	1 to 20		15.34	0.091	
	2 3 5	1VA+1LTA+1LTA*	15.28	0.091	
	1 4 6	1LTS+1VS+1TS	22.2	0.1124	
	2 4 6	1VA+1VS+1TS	22.2	0.1124	
Hardanger ADs	Modes		$V_{cr}$ [m/s]	$f_{cr}$ [Hz]	$V_{red}$
$P_{1-6}^* = 0$	1 to 20		19.03	0.0904	2.1
$H_{5,6}^* = 0$	2 3 5	1VA+1LTA+1LTA*	19.03	0.0904	2.1
$A_{5,6}^* = 0$	2 3	1VA+1LTA	20.41	0.0904	2.3
	2 5	1VA+1LTA*	28.78	0.1068	2.7
	1 4 6	1LTS+1VS+1TS	26.41	0.1129	2.3
	2 4 6	1VA+1VS+1TS	26.41	0.1129	2.3
Hardanger ADs	Modes		$V_{cr}$ [m/s]	$f_{cr}$ [Hz]	$V_{red}$
	1 to 20		26.47	0.1129	2.3
	1 4 6	1LTS+1VS+1TS	26.47	0.1129	2.3
	2 4 6	1VA+1VS+1TS	26.47	0.1128	2.3
	2 3 5	1VA+1LTA+1LTA*	35.84	0.1073	3.32
	4 6	1VS+1TS	26.53	0.1128	2.3
	2 5	1VA+1LTA	28.9	0.1078	2.7

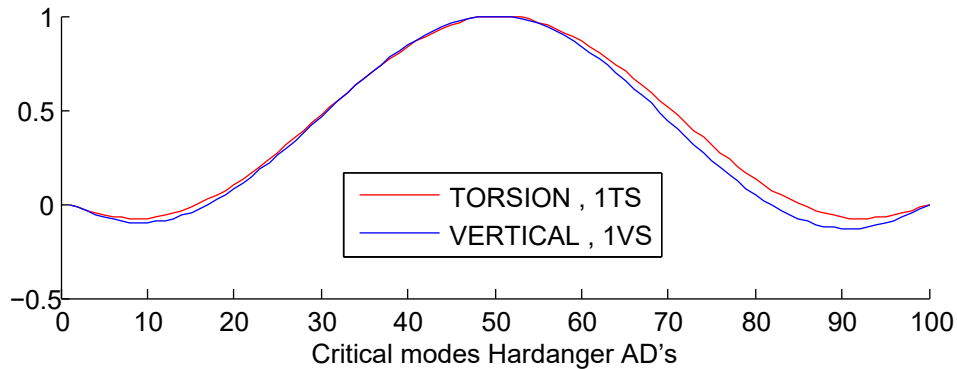
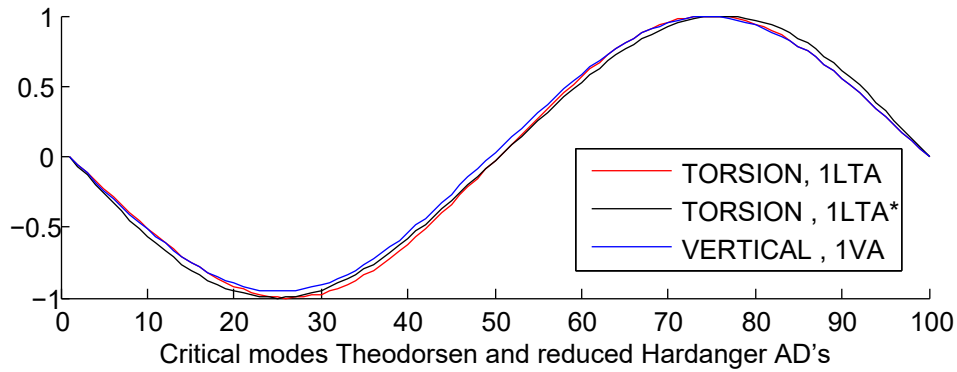


Figure 23: Similarity of critical modes for Setup 1

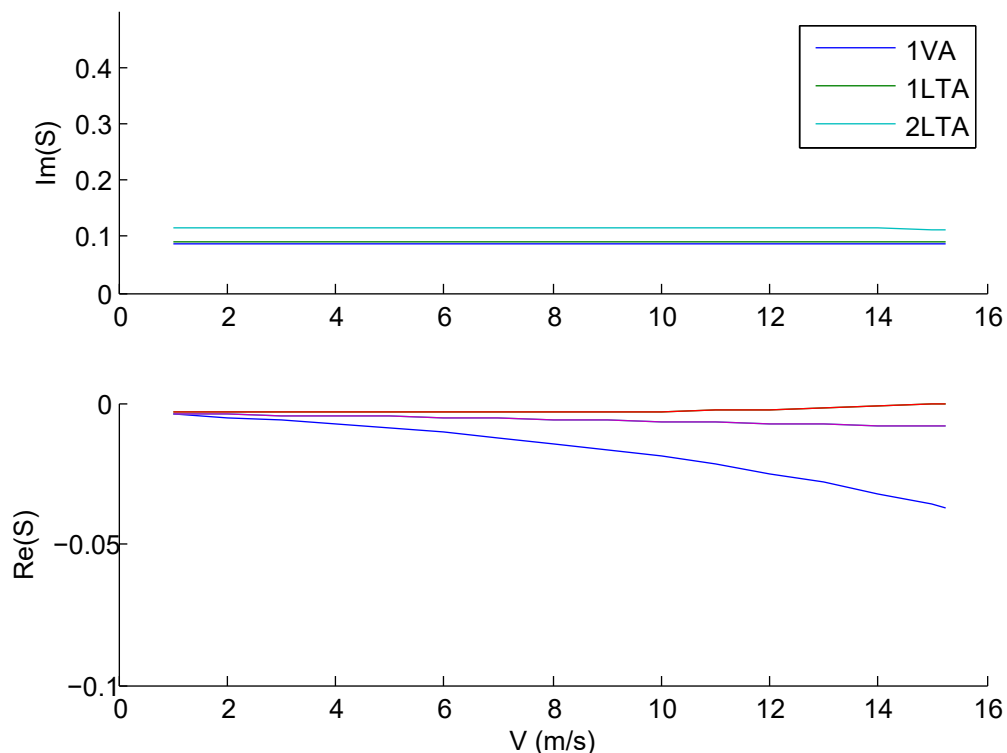


Figure 24: Solution of the complex eigenvalue problem for Setup 1 with Theodorsen ADs.

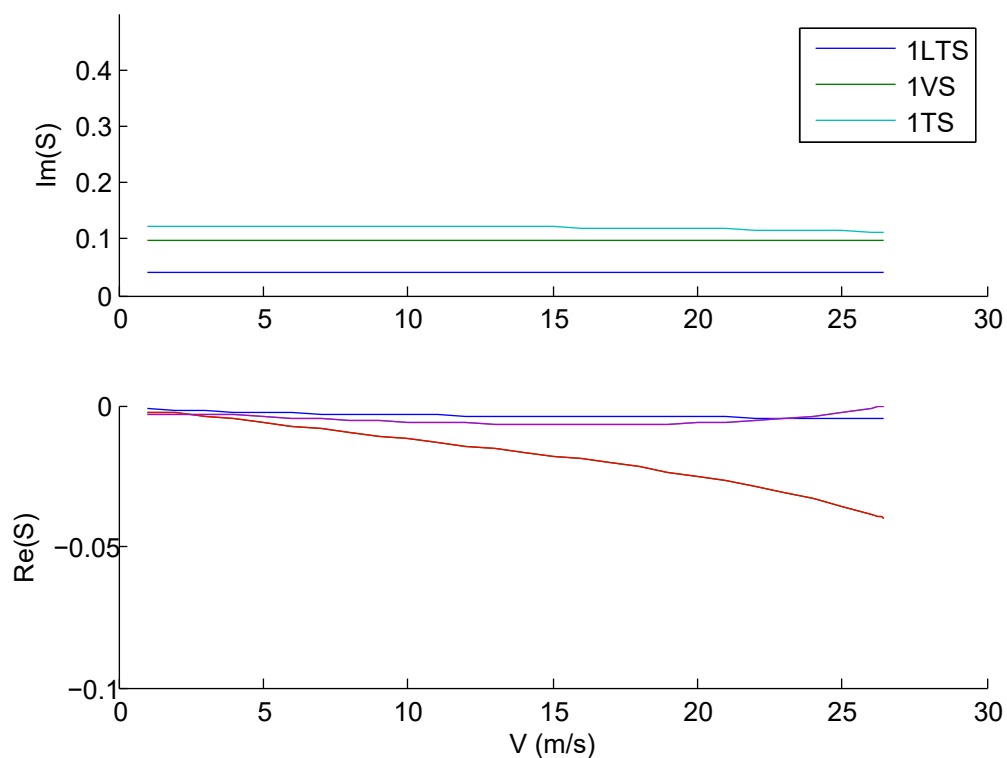


Figure 25: Solution of the complex eigenvalue problem for Setup 1 with Hardanger ADs.

In Table 15 the stability limits are calculated with different ADs. The calculations where  $P_{1-6}^* = 0$ ,  $H_{5,6}^* = 0$ , and  $A_{5,6}^* = 0$  is performed in order for the results to be comparable with the Theodorsen results, as these derivatives are zero for all Theodorsen analyses. Finally, the full set of 18 ADs is obtained from the Hardanger Bridge.

The stability limit in the results for Setup 1 involves different critical modes when the horizontal derivatives are neglected, compared to when the full set of Hardanger ADs are used. The reason that the modes 1VA, 1LTA, and 1LTA\* are the critical mode for the Theodorsen and the Hardanger  $P_{1-6}^* = 0$ ,  $H_{5,6}^* = 0$ , and  $A_{5,6}^* = 0$ - calculations is because the lateral contributions are not participating. The torsional modes of Setup 1 contains significant deflections in the lateral direction, see Appendix C. This will introduce noticeable aerodynamic damping to the system, especially through  $H_5^*$  and  $A_5^*$  which has large values in the Hardanger case. See Figure 18. Theodorsen and the reduced Hardanger ADs cannot account for the damping of these modes, thus the antisymmetric modes become critical because they have lower frequency and lower frequency ratio than the symmetric. In the calculation with all the Hardanger ADs, the antisymmetric modes will be damped out, leaving the symmetric modes to couple and create flutter, as these modes do not contain lateral deflections.

### 7.3 Adopting the Messina ADs for Setup 2 and 3.

Despite considerable effort by the author, the implementation of the Messina ADs has not been completely successful. The ADs have not given any critical velocity within an acceptable range of reduced velocities. The results obtained by using the Messina ADs for Setup 2 and 3 are presented below, as well as the limitations and errors that comes with them.

The Messina ADs are normalized by the full width of the Messina triple- girder section, being 60 meters. Despite this, any attempt of running a flutter analysis with the full width of section 2 and 3 has not given convergence in the frequency iterations. Some assumptions are made in order to find a reasonable width to calculate the self- excited forces.

There are mainly two factors that complicates the flutter calculations for Setup 2 and 3

1. The width of the bridge section must be specified in the flutter routine. This width is used to calculate the self- excited forces described in Equation 19. The width must have the same definition as the width used to normalize the velocities in the experimental data when creating the aerodynamic derivatives. The width used for the Messina ADs are 60 meters, and describe the distance between the outside of the external girders. For Setup 2 and 3 the distances according to this convention is 39 and 55 meters, respectively. However such wide configurations are not able to reach frequency convergence in the flutter script. Rendering from Chapter 6.4 that Messina Bridge is a very stiff and heavy structure compared to the lean and light-weight configurations in Setup 2 and 3. Messina bridge has three wide girders, and narrow gaps between them. See the different gap-to-total-width ratios,  $R_{gap/width}$  for the three bridges in Table 16.

\* The ratio from Messina is approximate and is calculated by the author from Fig.9 in Larsen, 2014 [14].

Table 16: Ratio between total width and total gap-width

Bridge section	$R_{gap/width}$
Messina Bridge	0.22*
Setup 2	0.41
Setup 3	0.58

Considering the wide gaps and small side-girders of Setup 2 and 3 it is assumed reasonable to reduce the width for the self excited forces in the flutter analysis for Setup 2 and 3. This is mainly because the large dimensions of Messina Bridge will give too large wind forces on Setup 2 and 3. The width is scaled down by a factor of 2/3. This reduced width allows the script to reach convergence for both setups.

Table 17: Reduced width used in flutter calculations for Setup 2 and 3

Bridge section	B [m]
Setup 2	26
Setup 3	37

- The Messina ADs are created from experimental data, and are defined for reduced velocities  $V_{cr} = \frac{V}{f \cdot B}$  from 0 to 18. These derivatives are curve-fitted by polynomials of different order in the search of an optimal fit. None of the fittings that was tried out was able to provide a critical wind velocity within the valid domain of the experimental data. It is seen in Table 18 and 19 that the reduced velocity that gives unstable behaviour is more than 18 in all mode combinations for setup 2 and 3. Since the Messina ADs are unable to cause flutter instability for both setups, it is concluded that they are not suited for approximate flutter calculations of Setup 2 and 3.

Despite these considerations, the results of the flutter procedure with the Messina ADs are reported and discussed below. The physics of Setup 2 and 3 will be analysed and discussed further in Chapter 7.6 and 7.7 with Theodorsen and Hardanger ADs, as these give more stable results.

## 7.4 Setup 2

The mode combinations and stability limits for Setup 2 calculated with Messina ADs is presented in Table 18. The instability is identified as a 3-mode flutter mechanism where 1VA, 1TA and 1LTA is the critical mode shapes. As previously mentioned the Messina ADs is described as a fourth order polynomial, and is only valid up to  $V_{red} = 18$ . The critical wind velocities for Setup 2 violates this. It is obvious that the system turns unstable when the self-excited forces that acts on it, is calculated from the diverging domain of a fourth order polynomial. This means that the stability limit is not found by analysing the physics of the oscillating in-wind system, but rather based on the choice of interpolation. In Table 18 the stability limit of a second order polynomial as a curve



fitting is also displayed. Neither of the polynomials that is tried out in the calculations has given stability limits within the valid domain of the Messina ADs.

Table 18: Critical wind velocity for Setup 2

Messina ADs	Mode nr.	Mode ID	$V_{cr}$ [m/s]	$f_{cr}$ [Hz]	$V_{red}$
4th order poly	1 to 20		49.61	0.0883	21.6
	1 to 4		49.39	0.0883	21.5
	2 3 5	1VA+1TA+1LTA	49.58	0.0883	21.6
	4 6	1VS+1TS	66.16	0.0877	29.0
2nd order poly	1 to 20		71.20	0.0946	32.7

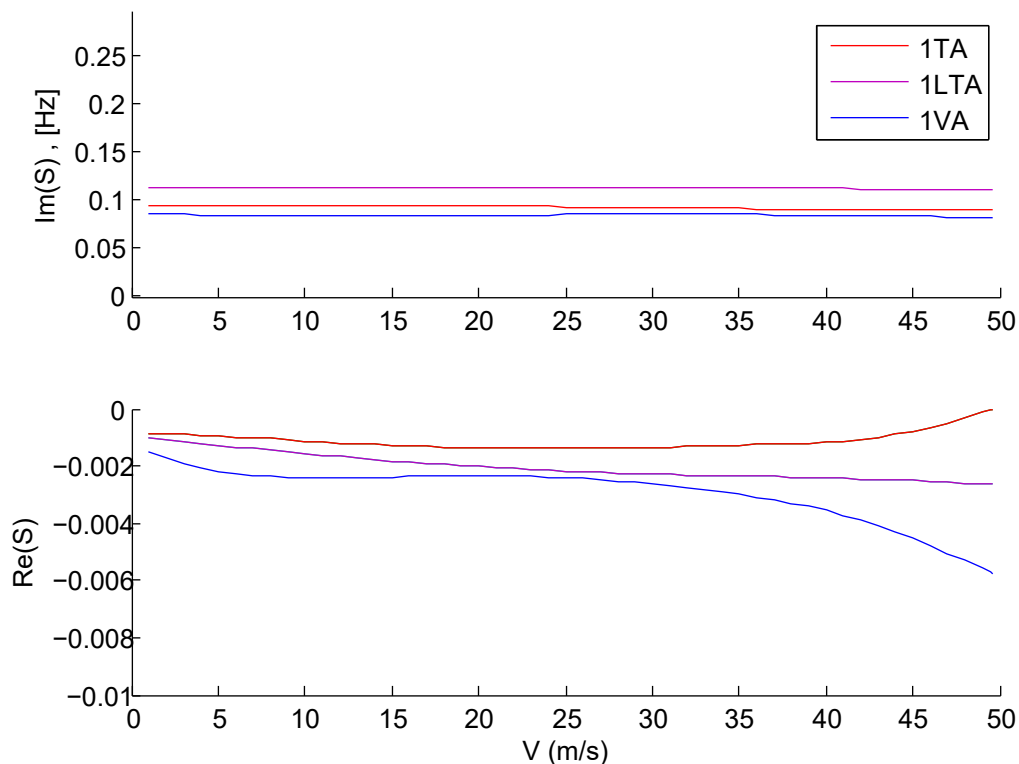


Figure 26: Solution of the complex eigenvalue problem for Setup 2 with Messina ADs.

Because of the questionable validity of the results obtained by using the Messina ADs, one must be careful in order to interpret them. Based solely on the frequency ratios between the first shape-wise similar modes in vertical direction and in torsion, Setup 2 is expected to reach flutter at low wind speeds. Because of the increased rotational inertia, the stability limit is however expected to be higher than for Setup 1. By analysing the development of the imaginary part of the solution of the complex eigenvalue problem in Figure 27, we can not see any obvious intersection of shape-wise similar modes. The mode pair that is most often connected to the flutter instability is the 1VS and 1TS. What usually occurs is that the 1TS loose stiffness due to the self excited forces in torsion, and the frequency for 1TS is reduced. As the frequency approaches the shape-wise similar 1TS, and in some cases also intersect, the damping will turn negative, and flutter occurs. In Figure 27 we see that 1TA approaches 1VA up to a wind velocity of circa 40 m/s. However, the damping, specified by the ADs  $A_i^*$ ,  $H_i^*$ ,  $P_i^*$ ,  $i = 1, 3, 5$ , will not turn negative for this wind speed.

If we assume that it is the 1TA mode that is the driving mode that causes flutter, we are able to check the reduced wind velocity where this frequency branch surpasses the valid domain of the ADs. This way, we can estimate the highest wind velocity where it is reasonable to conclude that flutter has not occurred, under the current assumptions. Observing the development of 1TA in Figure 26 we see that it is more or less stable at its zero-wind frequency  $f = 0.095$  Hz. This corresponds to a velocity  $V = V_{red}^{max} \cdot B \cdot f = 44.5$  m/s.

As there has not been identified any stability limit within the valid domain of the ADs, the further considerations regarding the aerodynamic stability of Setup 2 is discussed in Chapter 7.6.

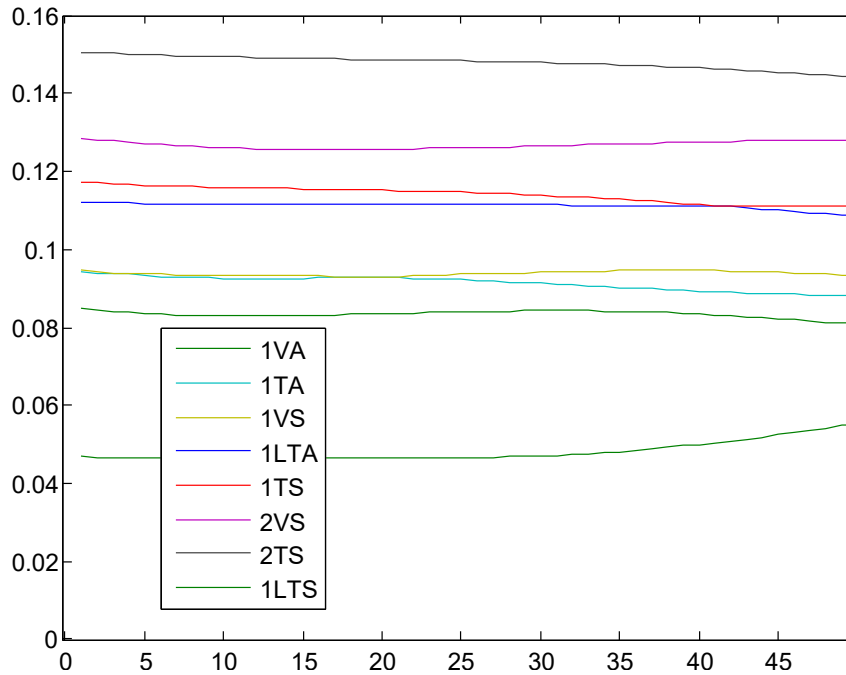


Figure 27: Imaginary part of solution for Setup 2, corresponding to frequencies. Messina ADs. Be aware of that each branch changes colour when crossing another branch. The legend refers to the initial colours.

## 7.5 Setup 3

As mentioned, the main issue when doing flutter analysis if Setup 3 with Messina ADs is the range of the reduced velocities. This setup has low torsional frequencies, and is believed to withstand high wind velocities. This requires a data set for high reduced velocities. As argued earlier, the ADs for Messina bridge is used in these flutter calculations. The data set is valid up to  $V_{red} = 18$ , and are extrapolated beyond this. In the extrapolated domain of the reduced velocities, the ADs and the self excited forces will grow exponentially. Due to this violent growth, the critical reduced velocity obtained in these calculations will be in the vicinity if the upper limit for the valid domain, namely close to 20 m/s. Because of this limitation in the ADs, the critical wind velocity is very similar for Setup 2 and 3. This is simply a matter of extrapolation, not necessarily a matter of physics. To be able to perform a reliable calculation of the flutter limit for

Setup 3, the real ADs must be measured and implemented.

Table 19: Critical wind velocity for Setup 3 with different extrapolation polynomials.

Messina ADs	Mode nr.	Mode ID	$V_{cr}$ [m/s]	$f_{cr}$ [Hz]	$V_{red}$
4th order poly	1 to 20		64.20	0.0818	21.2
	2 3 6	1TA+1VA+1LTA	64.19	0.0818	21.2
	2 3	1TA+1VA	63.99	0.0818	21.1
2nd order poly	1 to 20		81.08	0.0203	133.1
1st order poly	1 to 20		153.22	0.0997	41.5

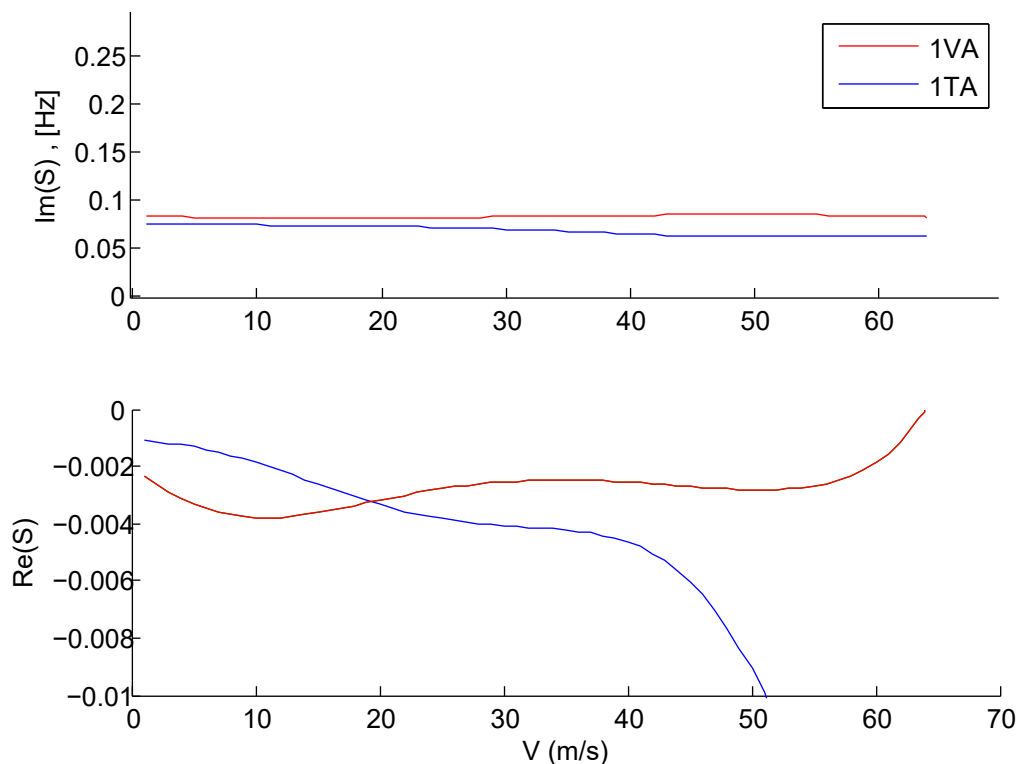


Figure 28: Solution of the complex eigenvalue problem for Setup 3 with Messina ADs.

In Table 19 we see the critical velocities for the different polynomials used to describe the Messina ADs. Since the development of the self excited forces outside the valid domain is much slower for the 1st and 2nd order polynomial, the critical velocity attains higher values. It is however only a matter of extrapolation. Hence the results outside the valid experimental data will not be further discussed.

The behaviour of Setup 3 is as predicted when the conceptual design was created by supervisor Michael Styrk Andersen. We can see in Figure 29 that the shape-wise similar torsional and vertical modes, e.g. 1TA/1VA and 1TS/1VS, experiences a mode separation rather than a mode coupling.

The fact that these modes are separated as the wind speed increases, due to the low frequency ratio, should according to the classical understanding of the flutter mechanism prevent these two modes from causing flutter. However, it is the 1TA and 1VA that is

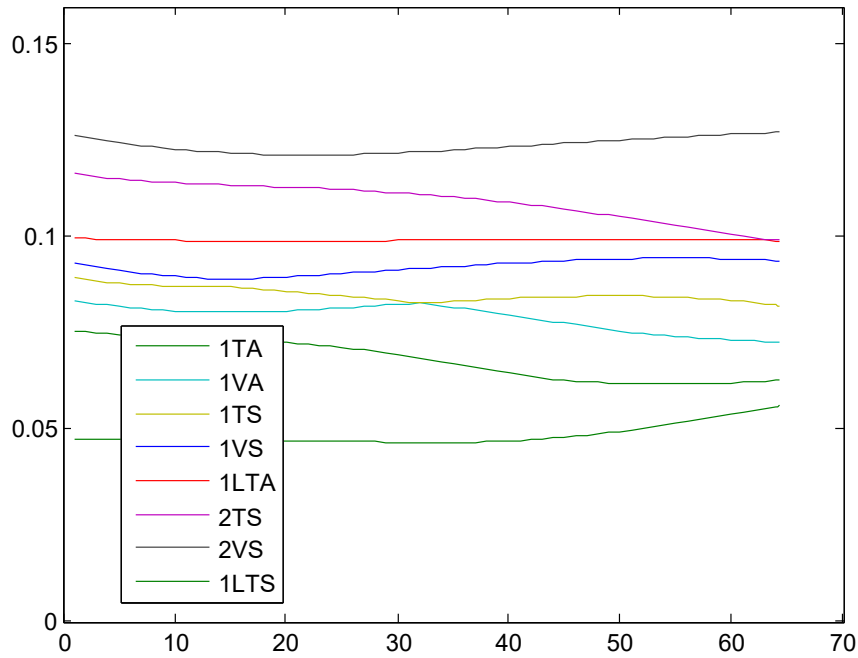


Figure 29: Imaginary part of solution for Setup 3, corresponding to frequencies. Be aware of that each branch changes colour when crossing another branch. The legend refers to the initial colours.

identified as the critical modes in the calculations, see Table 19. This does not mean that they cause flutter. It is simply a spurious result caused by the extrapolation of ADs.

The physical behaviour of Setup 3 is further discussed in Chapter 7.7, using Theodorsen and Hardanger ADs.

## 7.6 Setup 2 with Theodorsen and Hardanger ADs

As the Messina Bridge ADs are deemed to be unsuitable for Setup 2 and 3, the stability limit for these setups are calculated with Theodorsen ADs, and with Hardanger ADs. It is emphasized that neither of these ADs will provide the correct self-excited forces and damping for these setups. The section width used to calculate the self-excited-forces is the sum of widths of the three girders, namely 23 meters. Hence the gaps are not included in the width.

As presented in Table 20 the critical mode combination depends on the aerodynamic derivatives, in the same manner as for Setup 1. Setup 2 also has considerable lateral deflections in the anti-symmetric torsional mode shapes, causing high modal damping when using all 18 Hardanger ADs. The modes are illustrated in Appendix C. This is the reason that the anti-symmetric modes are critical when disregarding lateral effects.

The low stability limit is considered reasonable for this setup, due to the frequency ratio being just above 1. This corresponds to the preliminary feedback from the wind-tunnel testing of Setup 2, where classic flutter were observed for fairly low wind velocities. This might indicate that Theodorsen and Hardanger ADs describe the self-excited forces in

Table 20: Estimated critical wind velocity for Setup 2 with different types of ADs. B=23m

Theodorsen ADs		Modes	$V_{cr}$ [m/s]	$f_{cr}$ [Hz]	
	1 to 20		17.22	0.0929	
	2 3 5	1VA+1TA+1LTA	17.22	0.0929	
	2 3	1VA+1TA	17.41	0.0930	
Hardanger ADs		Modes	$V_{cr}$ [m/s]	$f_{cr}$ [Hz]	$V_{red}$
$P_{1-6}^* = 0$	1 to 20		22.28	0.092	1.7
$H_{5-6}^* = 0$	2 3 5	1VA+1TA+1LTA	22.28	0.092	1.7
$A_{5-6}^* = 0$	4 6	1VS+1TS	28.22	0.1107	1.8
Hardanger ADs		Modes	$V_{cr}$ [m/s]	$f_{cr}$ [Hz]	$V_{red}$
	1 to 20		28.22	0.1107	1.8
	4 6	1VS+1TS	28.22	0.1107	1.8
	2 3 5	1VA+1TA+1LTA	28.66	0.090	2.2

Setup 2 in a better way than the Messina ADs as there was not found any instabilities below 44.5 m/s.

The critical frequency is that of the 1TA at the critical wind velocity. Hence it is the first torsional anti-symmetric mode that is the driving mode for the flutter instability. As this mode is fairly close to the 1VA in the zero-wind case, these two modes cause classical flutter to occur for a fairly low wind speed for Setup 2.

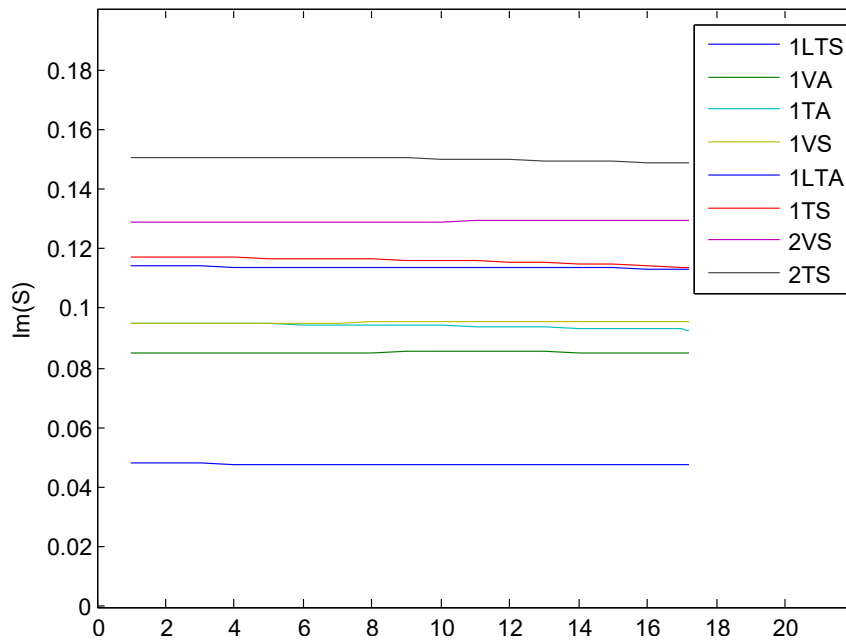


Figure 30: Frequency development for Setup 2, Theodorsen ADs. 10 first modes.

## 7.7 Setup 3 with Theodorsen and Hardanger ADs

Table 21: Estimated critical wind velocity for Setup 3. B=23m. No stability limit found.

Theodorsen ADs		Modes	$V_{cr}^*$ [m/s]	$f_{cr}$ [Hz]	$V_{red}$
	1 to 20		47.00*	0.0000	-
	2 3	1TA+1VA	47.00*	0.0000	-
Hardanger ADs		Modes	$V_{cr}^*$ [m/s]	$f_{cr}$ [Hz]	$V_{red}$
$P_{1-6}^* = 0$	1 to 20		71.00*	0.0000	-
$H_{5-6}^* = 0$	2	1TA	71.00*	0.0000	-
$A_{5-6}^* = 0$					-
Hardanger ADs		Modes	$V_{cr}^*$ [m/s]	$f_{cr}$ [Hz]	$V_{red}$
	1 to 20		71.00*	0.0000	-
	2	1TA	71.00*	0.0000	-

\*No critical velocities were found by the flutter routine for Setup 3.  $V_{cr}^*$  denotes the velocity where the first torsional frequency reaches zero, see Figure 31.

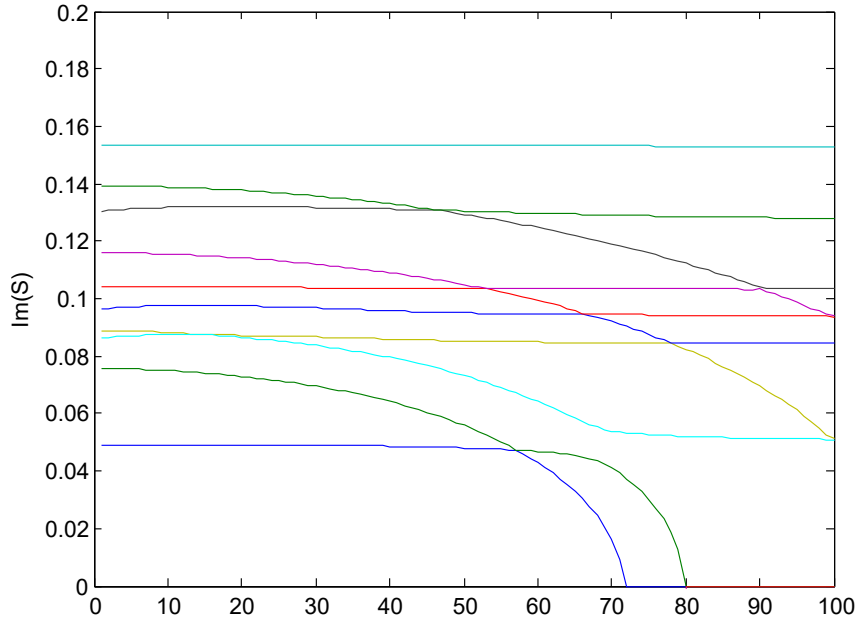


Figure 31: Frequency development for Setup 3, Hardanger ADs. 10 first modes. Be aware that the iterative flutter script sorts the frequencies by magnitude in each iteration. This disturbs the plot function, making each frequency branch to change colour when it crosses another branch.

It is noted that no critical wind velocity was found for Setup 3 using these ADs. As the wind velocity increases the frequencies are reduced, until they reach zero. This will require experimental data for infinite large reduced velocities. As this clearly is not the case, the results in Table 21 cannot be accepted. Mode number 2, the first torsional antisymmetric

(1TA) is reduced beyond mode number one, the first lateral torsional symmetric (1LTS). This is usually not the case for the zero-frequency instability *static divergence*. In this instability phenomena it is usually the first symmetric torsion that reaches zero frequency as it loses its stiffness because of the self excited forces.

The development of the frequencies displayed in Figure 31 shows signs of static divergence at a wind velocity of 71 m/s. The damping does however not attain negative values for this wind speed. It is assumed that the critical wind velocity is in the vicinity of where the first frequency reach zero, as this indicates that the net torsional stiffness is zero. Besides this remark, it is not discussed further how the in-wind system behaves as the frequencies approaches zero, as this is considered purely speculative. The ADs used throughout this thesis is extracted from wind tunnel testing where the bridge sections has 0 degrees rotation. The behaviour of the torsional modes, going steadily towards zero as the wind speed increases is therefore not necessarily correct, as the ADs will change as the girder rotates. It does however describe the bearing principle in the behaviour of Setup 3, that was observed in the wind tunnel tests.

The behaviour of Setup 3 in the wind tunnel test is similar to that of a twin-girder bridge with frequency ratio below unity, reported in M.Andersen, A.Johansson et al. [8]. Static divergence did not occur because the twin-girder section studied did not reach static divergence before exceeding the critical angle for stall. Stalling is a phenomena where the lift generated by a foil reduces because the rotation of the foil increases. An air foil must have smooth airflow over the foil in order to achieve lift. If the rotation gets too big, the upper-side of the foil will experience separated air-flow causing a reduction in lift and finally stalling. The critical angle for stalling is typically about 15 degrees [4]. The behaviour observed in the wind tunnel indicated lift combined with torsional deflections with reducing frequencies, as in Figure 31. As the section stalls, it will oscillate back to an equilibrium position. This movement is repeated and is considered as a steady-state situation for high wind velocities. The results for Setup 3 show similar but not identical behaviour, because it is not able to account for the rotation of the bridge deck.

## 7.8 Stability limit for Setup 1-3 with stiff crossbeams

Table 11 shows how the natural frequencies and vibration modes is affected by making the crossbeams very stiff. The torsional frequencies increased by 5-10% for Setup 1, 6-10% for Setup 2, and 12-23% for Setup 3. For Setup 3 the large increase in torsional stiffness changed the frequency ratio  $\gamma$  for the first shape wise similar pairs of torsional and vertical modes. The  $\gamma_{1S}$  and  $\gamma_{2A}$  for Setup 3 was changed to above unity, allowing classical flutter in Setup 3.

Table 22: Frequency ratios with stiff crossbeams

	Setup 1	Setup 2	Setup 3
$\gamma_{1A}$	1.15	1.20	0.99
$\gamma_{1S}$	1.33	1.28	1.07

Table 23: Stability limit and critical frequencies for Setup 1-3 with stiff crossbeams. The difference refers to the original stability limits of Setup 1-3 in Table 15, 20 and 21.

Setup 1						
Theodorsen ADs	Modes	$V_{cr}$ [m/s]	$f_{cr}$ [Hz]	$V_{red}$	Diff [%]	
1 to 20		18.28	0.0964	1.89	+19	
2 4	1VA+1LTA	19.16	0.966	1.97		
3 5	1VS+1TS	23.78	0.1144	2.07		
Reduced Hardanger *	Modes	$V_{cr}$ [m/s]	$f_{cr}$ [Hz]	$V_{red}$	Diff [%]	
1 to 20		20.41	0.0940	1.50	+7	
2 4	1VA+1TA	21.59	0.0946	1.58		
Hardanger ADs	Modes	$V_{cr}$ [m/s]	$f_{cr}$ [Hz]	$V_{red}$	Diff [%]	
1 to 20		25.22	0.0940	2.67	-5	
2 4	1VA+1LTA	28.72	0.0936	3.05		
3 5	1VS+1TS	28.09	0.1154	2.42		
Setup 2						
Theodorsen ADs	Modes	$V_{cr}$ [m/s]	$f_{cr}$ [Hz]	$V_{red}$	Diff [%]	
1 to 20		20.53	0.0993	1.43	+19	
2 4	1VA+1TA	20.59	0.0992	1.44		
3 5	1VS+1TS	25.84	0.1168	1.53		
Reduced Hardanger *	Modes	$V_{cr}$ [m/s]	$f_{cr}$ [Hz]	$V_{red}$	Diff [%]	
1 to 20		25.65	0.0984	1.80	+15	
2 4	1VA+1TA	25.72	0.0984	1.81		
Hardanger ADs	Modes	$V_{cr}$ [m/s]	$f_{cr}$ [Hz]	$V_{red}$	Diff [%]	
1 to 20		27.03	0.0973	1.92	-4	
2 4	1VA+1TA	27.09	0.0972	1.93		
3 5	1VS+1TS	31.59	0.1163	1.89		
Setup 3						
Theodorsen ADs	Modes	$V_{cr}$ [m/s]	$f_{cr}$ [Hz]	$V_{red}$		
1 to 20		20.65	0.1023	1.39		
4 5	1VS+1TS	20.59	0.1023	1.39		
Reduced Hardanger *	Modes	$V_{cr}$ [m/s]	$f_{cr}$ [Hz]	$V_{red}$		
1 to 20		27.03	0.1014	1.85		
4 5	1VS+1TS	26.90	0.1014	1.84		
Hardanger ADs	Modes	$V_{cr}$ [m/s]	$f_{cr}$ [Hz]	$V_{red}$		
1 to 20		25.84	0.1020	1.75		
4 5	1VS+1TS	25.66	0.1020	1.74		

\*Reduced Hardanger ADs:  $P_{1-6}^* = 0$ ,  $H_{5-6}^* = 0$ ,  $A_{5-6}^* = 0$



It is obvious that the stiff crossbeams has considerable influence of the stability limit of Setup 3. The inverted frequency ratios makes the "flutter free" Setup 3 susceptible for classical flutter, a result that undermines the very purpose of the conceptual design.

The stability limits for this configuration is listed in Table 23. The increased stiffness of the crossbeams has clearly affected the stability limit of Setup 1 and 2. The Theodorsen-calculations stands out with the most affected result. For Setup 1 and 2 the stability limit is increased by 19% for the Theodorsen calculations. The Hardanger- results is decreased by 4 and 5% for the two setups.

The fact that the critical velocities is affected differently depending on the choice of ADs shows the dependency of the results with regards to the ADs. The stability limits of Theodorsen and reduced Hardanger calculations is raised because of the increase of frequency-ratios for Setup 1 and 2. The torsional frequencies are increased, but the frequency of the vertical modes are almost unaffected. The stability limit of the Theodorsen analysis has the biggest increase because these ADs assume very strong coupling between the vertical and torsional modes through  $H_3^*$  and  $A_4^*$ . This is illustrated in Figure 17 and 18.

The stability limits calculated with full Hardanger ADs in Table 23 are lower with stiff crossbeams than for the regular Setup 2. This is because the lateral deflection in the critical torsional mode 1TA is considerably smaller for the case with stiff crossbeams. This is demonstrated in Figure 32. The small lateral contributions will decrease the over-all aerodynamic damping of this mode. This leads to a low stability limit for the Hardanger ADs. Theodorsen and reduced Hardanger ADs remains unaffected by the change in lateral deflection of the mode shapes because they disregard all lateral effects.

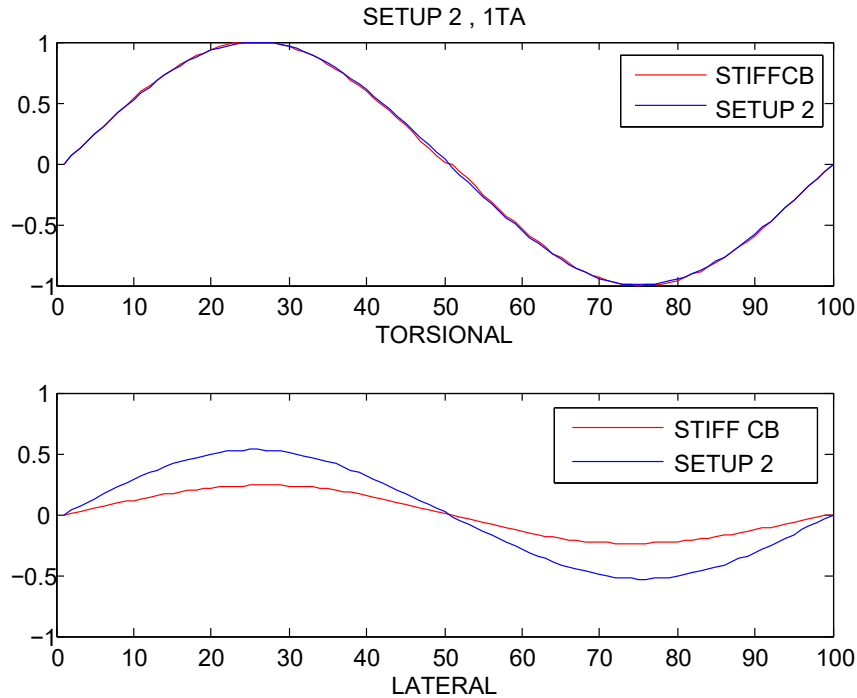


Figure 32: Mode shape of 1TA for regular Setup 2 and Setup 2 with stiff crossbeams.

Disregarding the flutter-analysis and focusing merely on the changed natural frequencies, the stiffness of the crossbeams should in general be beneficial for suspension bridges where

the frequency ratio  $\gamma > 1$ . For bridges where  $\gamma < 1$  the changed stiffness will be destructive if the increase in torsional frequency will make  $\gamma > 1$  like in the case for Setup 3, and thus allowing flutter to occur.

## 7.9 Modified Setup 3 with improved torsional stiffness

As the technology allows us to construct even longer bridge spans, the need for bridge designs with stable and predictable aerodynamic behaviour becomes even more important. It is not enough that a bridge section avoids flutter by having frequency ratio less than one- it must also have sufficient torsional stiffness to avoid large torsional deflections as well as static divergence. In order to achieve low frequency ratios and at the same time increase the torsional stiffness, one can increase the cable distance and at the same time move mass from the central girder to the external girder. This will increase the torsional stiffness and the mass moment of inertia of the girder simultaneously [8]. By optimizing these two parameters it is possible to achieve high torsional stiffness and frequency ratios below 1.

To illustrate this idea a new and modified model of Setup 3 is created by the FE-model. In this analysis the cable distance is increased from 30 to 40 meters. The mass of the central girder is reduced from 3300 kg/m to 1400 kg/m, and the mass of the external girders are increased from 3050 to 4000 kg/m. Hence the total mass of the structure is the same as for Setup 3, but the torsional stiffness and the mass moment of inertia is increased.

Table 24: Natural frequencies of modified Setup 3. Increased cable distance. Mass is moved from central to external girder. Error refers to the regular Setup 3.

Mode ID	Setup 1	f [Hz]	Error [%]
1	1LTA	0.0496	0.81
2	1TA	0.0827	9.51
3	1VA	0.0865	0.12
4	1TS	0.0964	8.58
5	1VS	0.0965	0.13
6	2LTA	0.1040	0.05
7	2TS	0.1273	10.42
8	2VS	0.1307	0.23
9	2TA	0.1529	10.05
10	2LTS	0.1533	0.08
11	2VA	0.1584	0.34

Table 25: Frequency ratio for first pair of torsional and vertical mode pairs

$\gamma_{1A}$	0.96
$\gamma_{1S}$	1.00

Table 24, 26, and Figure 33 shows the natural frequencies and the solution to the complex

eigenvalue problem for a modified Setup 3. A triple-girder configuration like this will be very difficult to construct and is perhaps not realistic. As this analysis is about optimizing the stiffness-to-mass ratio, such considerations has been neglected and left for future research.

Table 25 shows that the frequency ratios is still less than or equal to one, making also the new configuration *flutter-free*. As Figure 33 clearly states, the increased torsional stiffness has increased the wind speeds where the frequencies turns zero. Even though the ADs are not correct for this section nor within the domain of the reduced velocities, the flutter analysis is able to account for the increased torsional stiffness. This makes the stability limit for static divergence increase as the stiffness is increased. This behaviour is also expected for the steady state stall and divergence- oscillations that was observed in the wind tunnel. The results of the CEV- analysis in Figure 33 indicate static divergence at a wind velocity of 91 m/s. The damping does however not attain negative values for this wind speed. It is again assumed that the critical wind velocity is in the vicinity of where the first frequency reach zero, as this indicates that the net torsional stiffness is zero. This is a remarkable increase of critical wind velocity compared to the regular configuration of Setup 3.

Table 26: Stability limit and critical frequencies for modified Setup 3. Increased cable distance. Mass is moved from central to external girder

Setup 1				
Theodorsen ADs	Modes	$V_{cr}^*$ [m/s]	$f_{cr}$ [Hz]	$V_{red}$
1 to 20		58*	0.0000	-
Hardanger ADs	Modes	$V_{cr}^*$ [m/s]	$f_{cr}$ [Hz]	$V_{red}$
1 to 20		91*	0.0000	-

\* No critical velocity is found because of the low frequency ratio.  $V_{cr}^*$  refers to the velocity at which the first natural frequency acheives zero frequency.

The behaviour demonstrated in Figure 33 is anticipated of a any suspension bridge with frequency ratio below or equal to one, regardless of the aerodynamic derivatives. It is merely the physics of the flutter phenomena and static divergence that explains this behaviour.

Figure 33 describes the bearing principle of the phenomena observed by Setup 3 in the wind tunnel tests. Just as described in Chapter 7.7, the results indicates that static divergence will occur for high wind speeds. The divergence/stall behaviour is not predicted because the ADs used in the calculations do not consider the effects of girder rotation, which is the controlling parameter for stall. Therefore, they are not able to describe the behaviour that is observed in the wind tunnel. Figure 33 does however predict the physics of the system for small angles of rotation. It is reasonable to conclude that the increased torsional frequencies will increase the stability limit for static divergence even when accounting for the rotation of the girder.

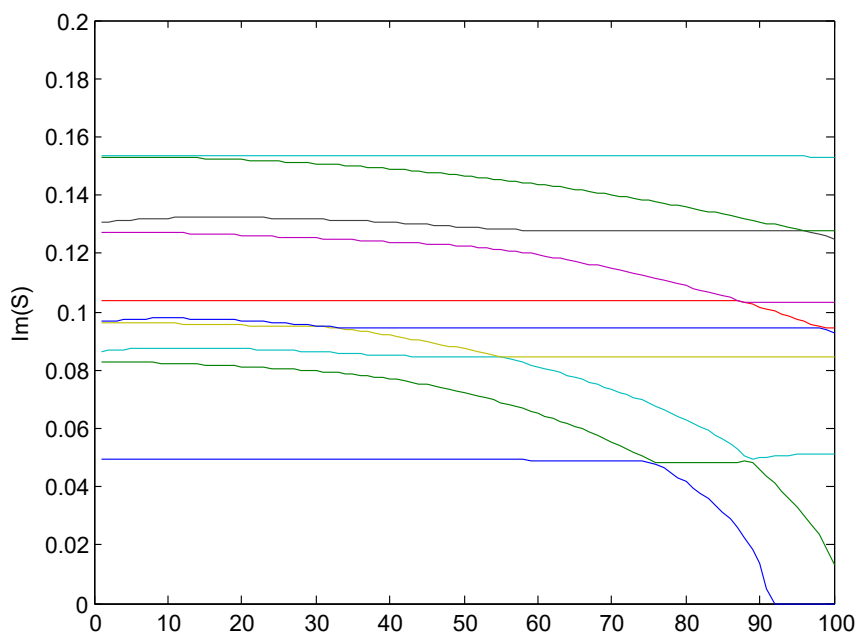


Figure 33: Frequency development of modified Setup 3 with Hardanger ADs.

---

## 8 Final considerations and main research findings

The FE-model is verified by customizing it to describe the Hardanger Bridge. The modal output is in good agreement with previous calculations on the Hardanger Bridge, performed by the author as well as the Norwegian Public Roads Administration (NPRA). The FE-model was able to reproduce the natural frequencies and mode shapes of the experimental setups created by Michael Styrk Andersen. The effect of variable pylon stiffness over the height of the pylons was investigated, and it was decided that this effect may be disregarded in this study. This is because of low influence on the eigenfrequencies within reasonable stiffness variation of the pylons.

The most innovative analysis regarding previous research is the investigation on how the cross beams of the multi-girder bridges affect the frequency ratio. For the wide Setup 3 very stiff crossbeams resulted in frequency ratios above 1. This result undermines the very purpose of the design of Setup 3, and must be avoided in a real detailed design situation.

The results in this thesis confirms that the quality and validity of aerodynamic derivatives is crucial in order to get trustworthy behaviour of flexible bridges subjected to wind loads. The challenge of obtaining high-quality ADs within a sufficiently large range of reduced wind velocities is not yet eliminated in the state of the art of bridge aerodynamics. For some of the calculations performed in this thesis, the stability limit has been highly sensitive to the choice of curve fitting. The ADs that is used are measured for zero-degree rotation of the bridge deck, which prevents the model from describing instabilities where natural frequencies of torsional modes drops to zero because of large rotations. It is emphasized that except for the Hardanger Bridge, the aerodynamic derivatives used to assess the stability are not the correct ADs for the different setups. This is a major weakness of the model.

The stability limit for the Hardanger Bridge replica is found in order to verify the calculation routine. The critical wind velocity was 77.5 m/s. The results agrees well with the stability limit calculated by NPRA. For the innovative single-girder Setup 1, a low stability limit of 26.5 m/s was obtained when using the ADs of Hardanger Bridge. These ADs are expected to give reasonable results for Setup 1.

Setup 2 has a lower frequency ratio than Setup 1, but is still expected to have a marginally higher stability limit due to its large cable distance and torsional inertia. This setup was originally calculated with the ADs of Messina Bridge, but the results are disregarded because of their unreliable nature. Setup 2 has a stability limit of 28.2 m/s when using Hardanger Bridge ADs. This corresponds good to observations made the wind tunnel testing of this setup. Both Setup 1 and 2 has far too low stability limits to be constructed on the Norwegian west coast. The critical design wind speed for the Hardanger Bridge is 57.9 m/s [19]. If we assume similar wind conditions in Halsafjorden it is obvious that these setups has too low stability limits, which was expected.

It was not found any stability limit for Setup 3 which indicates that classical flutter will not occur. The section shows very good aerodynamic behaviour, based on the frequency-ratios. The correct ADs for this setup is expected to enhance this behaviour even further.

The behaviour of the in-wind modes and frequencies agrees well with the observations from the testing, for low torsional angles of the bridge deck. The stiffness of the crossbeams had great influence on the aerodynamic stability of Setup 3, mainly because the inverted frequency ratio allowed classical flutter.

All the stability calculations have been performed with Theodorsen and Hardanger ADs both with and without the lateral terms  $P_{1-6}^*$ ,  $H_{5,6}^*$ , and  $A_{5,6}^*$ . The results states that it is conservative to disregard the lateral terms for all configurations in this thesis. For some of the configurations the large lateral deflections of the torsional modes introduced aerodynamic damping in the system that increased the stability limit. This effect gave discrepancies concerning which modes that are critical, depending on whether or not lateral terms are included. For the analysis with stiff crossbeams the lateral contributions of the anti-symmetric modes was reduced, causing even further reduction of the stability limit of this configuration.

## 8.1 Further work

As the work presented in this report has been conducted, Michael has performed wind tunnel testing of Setup 1-3. The results is not yet processed, so it is left for further research to implement the correct ADs in the flutter routine.

In the FE-model the pylons is modelled with constant stiffness over the entire length. This stiffness is the same as the lowest increment of the Hardanger Bridge pylons. Further investigations may determine the effect on the natural frequencies when decreasing the stiffness over the height.

The FE-model accepts A-shaped pylons with different cable distance over the pylons and mid-span. This feature triggered some numerical difficulties regarding buckling of the cross-beams mid span for the widest setups. This problem is assumed to be manageable even though it is not treated any further in this thesis.

It is commonly known that extraction of the lateral ADs complicates the wind tunnel testing considerably, and that it is difficult to extract high quality data for these ADs. As the results in this paper indicates, the lateral ADs may be important in order to simulate the real in-wind behaviour of the bridge. This is especially important for super-long suspension bridges that has considerable lateral deflections in some vibration modes. As the length of the contemporary suspension bridges increase, the lateral contributions of the self-exited loads will become even more important.

Some of the bridge setups proposed in this thesis is innovative and causes a series of civil engineering problems related to the construction and design of the setups. For instance the triple girder cross-section illustrated in Figure 34 is a challenging structure to implement. As the divergence/stall behaviour observed for Setup 3 is unacceptable for most structures, this behaviour must either be avoided, or require a wind speed far above the design wind speed. If the future within bridge design is to achieve stable super-long spans in wind-exposed environments, it will not be sufficient to find theoretical solutions to avoid aerodynamic instabilities. Engineers must also be able to construct the bridges in an economical and sustainable way.

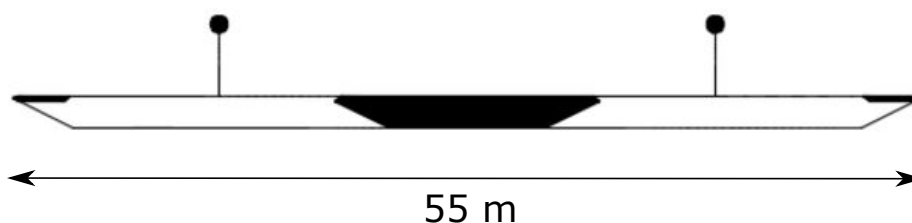


Figure 34: The triple-girder system will cause challenges related to detailed design.

## References

- [1] Simulia abaqus analysis user's guide, 2016.
- [2] T. Agar. Aerodynamic flutter analysis of suspension bridges by a modal technique. *Engineering Structures*, (11):75–82, 1989.
- [3] Anil K. Chopra. *Dynamics of Structures*. Prentice Hall, 2012.
- [4] Y.A. Cengel, J.M. Cimbala. *Fluid Mechanics: Fundamentals and Applications*. McGrawHill, 2010.
- [5] S.O.Hansen, C. Dyrbye. *Wind loads on structures*. Wiley, 1997.
- [6] Andersen et al. Non-flutter design principle for twin boxes. *14th international conference on wind engineering*, 2015.
- [7] G. Bartoli, S. D'Asdia, Febo, et al. Innovative configurations for long-span suspension bridges. *European African conferences on wind engineering*, (95):888–907, 2009.
- [8] M. Andersen, J. Johansson, Brandt, et al. Aerodynamic stability of long span suspension bridges with low torsional natural frequencies. 2016.
- [9] The Norwegian Public Roads Administration, Abaqus input file from NPRA's Hardanger Bridge pylons model. `tarn-urisset.imp`. 2016.
- [10] O. Øiseth, A. Rönnquist, R. Sigbjørnsson. Simplified prediction of wind-induced response and stability limit of slender long-span suspension bridges, based on modified quasi-steady theory: A case study. 2010.
- [11] O. Øiseth, A. Rönnquist, R. Sigbjørnsson. Finite element formulation of the self-excited forces for time-domain assessment of wind-induced dynamic response and flutter stability limit of cable-supported bridges. 2012.
- [12] O. Øiseth, R. Sigbjørnsson. An alternative analytical approach to prediction of flutter stability limits of cable supported bridges. *Journal of Sound and Vibration*, (330):2874–2800, 2 2011.
- [13] A. Larsen, G. Larose. Dynamic wind effects on suspension and cable-stayed bridges. *Journal of Sound and Vibration*, (334):2–28, 2015.
- [14] A. Larsen, editor. *Horizontal aerodynamic derivatives in bridge flutter analysis*, 2014.
- [15] P. D'Asdia, V. Sepe. Aeroelastic instability of long-span suspended bridges: a multi-mode approach. 1998.
- [16] M. Matsumoto, Y.Kobayashi, H. Shirato. The influence of aerodynamic derivatives on flutter. 1996.
- [17] Einar N. Strømmen. *Theory of bridge aerodynamics*. Springer, 2010.



- [18] Einar N. Strømmen. *Structural Dynamics*. Springer, 2014.
- [19] The Norwegian Public Roads Administration, Teknologivdelingen. Hardangerbrua, beregninger, kapittel 1, 2008.
- [20] T. Theodorsen. General theory of aerodynamic instability and the mechanism of flutter. *National advisory committee for aeronautics*, (496):1717–1737, 12 1934.
- [21] Scanlan, Tomko. Airfoil and bridge deck flutter derivatives. *Journal of Mechanical engineering division, American society for civil engineers*, (6):1717–1737, 12 1971.

# Appendices

## A Geometric and mechanical properties Setup 1-3

Table 27: Geometrical- and material- properties for Setup 1-3

Parameter	Central deck	External deck
Area [ $m^2$ ]	0,5391	1,225
Mass [kg/m]	3300	3050
Vertical second moment of inertia $I_y$ [ $m^4$ ]	0,4919	0
Lateral second moment of inertia $I_z$ [ $m^4$ ]	14,015	
Torsional inertia $I_T$ [ $m^4$ ]	0,15	
Youngs Modulus E [ $N/mm^2$ ]	2,05e11	2,05e11
Shear Modulus G [ $N/mm^2$ ]	7,8e10	7,8e10
	Hangers	Cables
Area [ $m^2$ ]	0,01	See Table 3
Youngs Modulus E [ $N/mm^2$ ]	2,05e11	2,05e11
	Crossbeams	Pylons
Area [ $m^2$ ]	0.073286	17.181
Mass [kg/m]	575.2	-
Vertical second moment of inertia $I_y$ [ $m^4$ ]	0.034401	
Lateral second moment of inertia $I_z$ [ $m^4$ ]	0.008386	
Torsional moment of inertia $I_T$ [ $m^4$ ]	0.15e-4	224.90
Youngs Modulus E [ $N/mm^2$ ]	2,1e11	4,0e11
Modulus G [ $N/mm^2$ ]	80,8e9	1,2e10

## B Geometric and mechanical properties Hardanger Bridge

The geometrical and mechanical properties of the approximated Hardanger FE-model in Chapter 5.1.

```

L=1310;           %Total span-length
L_side= 250;     %Side span length
d= 9;           %distance from main girder to side girders (center-center)
D=18;           %Distance between cables mid span
D_pylon=D;      %Distance between cables over pylons
subheight=20;   %Length of pylon legs under the girder
e_vert= 1.8;    %vertical distance from side to main girders

hangers= 67;    %must be an odd number

girder_sag= 20; %positive curvature of girder before gravity
h=25;          %vertical distance from cable to girder before gravity
sag=110+h;     %Sag of cable before gravity loads are applied






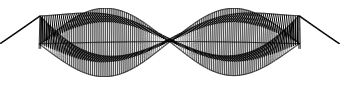
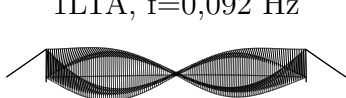
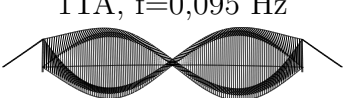
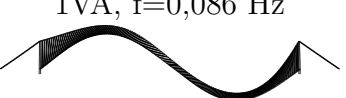
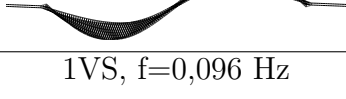
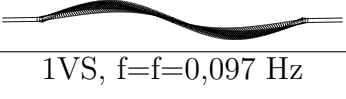
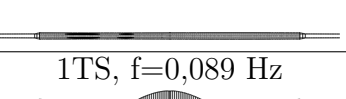
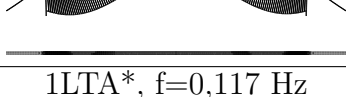
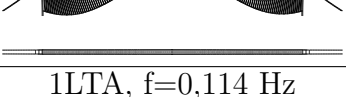
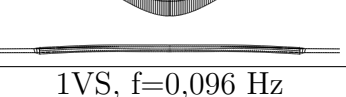

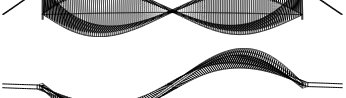

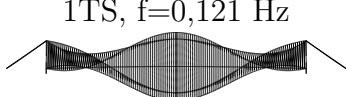
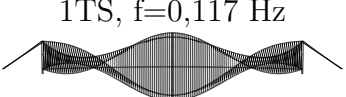
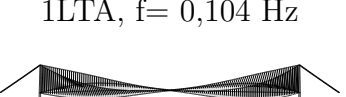
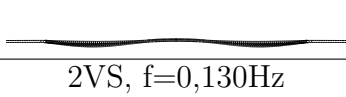
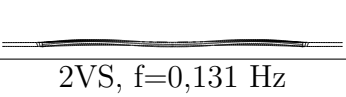
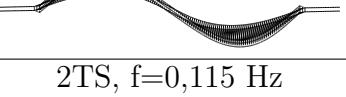
```



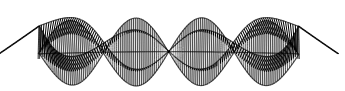
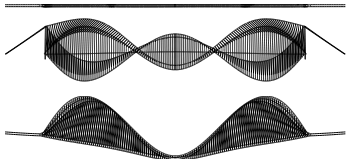
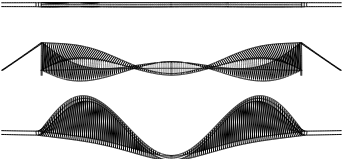
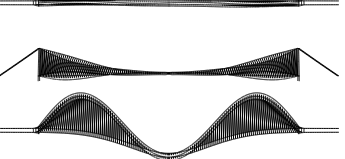
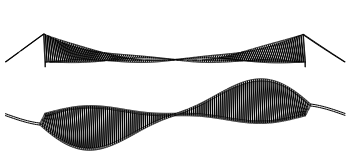
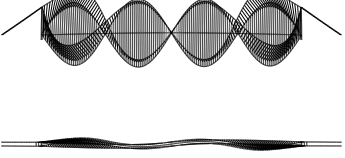
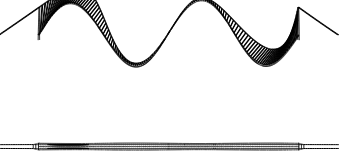
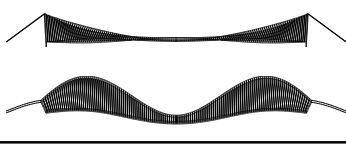
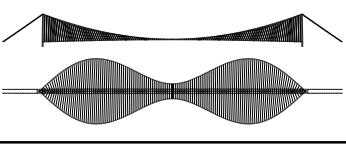
Table 28: Geometrical- and material- properties of the Hardanger Bridge

Parameter	Central deck	
Area [ $m^2$ ]	0,5813	
Mass [kg/m]	8080	
Vertical second moment of inertia $I_y$ [ $m^4$ ]	0,972	
Lateral second moment of inertia $I_z$ [ $m^4$ ]	16,448	
Torsional moment of inertia $I_T$ [ $m^4$ ]	4,298	
Vertical mass moment of inertia $I_{m,y}$ [ $m^4$ ]	217020	
Lateral mass moment of inertia $I_{m,y}$ [ $m^4$ ]	12515	
Youngs Modulus E [ $N/mm^2$ ]	2,10e11	
Shear Modulus G [ $N/mm^2$ ]	8,08e10	
	Hangers	Cables
Area [ $m^2$ ]	0,0032	0,22132
Youngs Modulus E [ $N/mm^2$ ]	1,6e11	2,00e11
	Crossbeams	Pylons
Area [ $m^2$ ]	1	17.181
Mass [kg/m]	1	-
Vertical second moment of inertia $I_y$ [ $m^4$ ]	1000	172,65
Lateral second moment of inertia $I_z$ [ $m^4$ ]	1000	124,66
Torsional moment of inertia $I_T$ [ $m^4$ ]	0	224.8967383
Youngs Modulus E [ $N/mm^2$ ]	2,1e11	4,0e10
Modulus G [ $N/mm^2$ ]	80,8e9	1,2e10

## C Mode shapes for Setup 1-3

Table 29: Modeshapes for Setup 1-3. Sideview/Topview.

ID	Setup 1	Setup 2	Setup 3
1	1LTS, $f=0,042$ Hz 	1LTS $f=0,048$ Hz 	1LTS, $f=0,049$ Hz 
2	1VA, $f=0,086$ Hz 	1VA, $f=0,087$ Hz 	1TAf= $0,076$ Hz 
3	1LTA, $f=0,092$ Hz 	1TA, $f=0,095$ Hz 	1VA, $f=0,086$ Hz 
4	1VS, $f=0,096$ Hz 	1VS, $f=0,097$ Hz 	1TS, $f=0,089$ Hz 
5	1LTA*, $f=0,117$ Hz 	1LTA, $f=0,114$ Hz 	1VS, $f=0,096$ Hz 
6	1TS, $f=0,121$ Hz 	1TS, $f=0,117$ Hz 	1LTA, $f=0,104$ Hz 
7	2VS, $f=0,130$ Hz 	2VS, $f=0,131$ Hz 	2TS, $f=0,115$ Hz 
8	2LTS, $f=0,158$ Hz 	2TS, $f=0,151$ Hz 	2VS, $f=0,130$ Hz 

ID	Setup 1	Setup 2	Setup 3
9	2VA, $f=0,158$ Hz 	2VA, $f=0,159$ Hz 	2TA, $f=0,139$ Hz 
10	3LTS, $f=0,177$ Hz 	2LTS, $f=0,171$ Hz 	2LTS, $f=0,153$ Hz 
11		2TA, $f=0,182$ Hz 	2VA, $f=0,158$ Hz 
12			3TS, $f=0,174$ Hz 